Polarimetry of the irregular galaxy m82

William Stuart Pallister

POLARIMETRY OF THE IRREGULAR GALAXY M82

BY

WILLIAM STUART PALLISTER

A THESIS PRESENTED AT THE
UNIVERSITY OF DURHAM
FOR THE DEGREE OF PH.D.

SEPTEMBER 1976

ABSTRACT

This thesis contains an account of some of the work undertaken by the author while a member of the Astronomy Group at the University of Durham. The work of the group which involves the measurement of the amount of linear polarisation in nebular astronomical objects, is in collaboration with the Royal Greenwich Observatory.

The initial chapters of the thesis describe the design and construction of the Durham Polarimeter which detects and measures the polarisation, and outlines the advantages of using a 4 cm McMullan electronographic camera as a recording device. Initial alignment of the polarimeter components prior to observation and the procedures followed to obtain a series of electronographic plates are described along with the development of a series of reduction equations which link the polarisation parameters to the densities of the images on the electronographic plates. Electronographs of the irregular II galaxy, M82, which is the subject of study in this thesis are illustrated.

In the later chapters of the thesis, the reduction of the visual electronographs to a digital form and the subsequent sophisticated computer programming required to accurately align the digital electronographs, read out the densities for several thousand locations distributed over the image of the galaxy, and finally convert these densities to polarisation parameters is described. Comparison of the new polarisation map of M82, with the previous photo-electric determinations confirms the success of this new automatic technique for the production of high resolution, accurate polarimetric measurements.

In the final chapters of the thesis, M82 is reviewed chronologically, and the observational information on the galaxy is summarised. Finally, the present polarisation data is analysed using a recent model of the galaxy, and the results which are consistant with those previously determined are considered in conjunction with the mass of observational evidence concerning the evolution and morphology of the galaxy. The possibility that M82 may represent a connecting link in galactic evolution is tentatively proposed.

TABLE OF CONTENTS

LIST OF FIGURES

LIST OF TABLES

LIST OF PLATES

INTRODUCTION

Our insight into the physical universe about us has evolved slowly for centuries, the main source of information being optical observations. The advent of large telescopes in the 20th Century, has led to vast increases in our knowledge, and these increases have been further extended by observations in other spectral regions, in particular, radio, micro-wave, X-ray and γ-ray. As each new window has become available, new vistas of the universe have been opened up to us, with a corresponding advance in our knowledge.

Along with the new areas of view, there has come an improvement in the techniques available to astronomers, so that even now further advances in optical astronomy are possible Not only can we look at the quantity of light reaching our telescope, but we can look at the quality of the light also. The spectra of stars and galaxies gives us details of the physical conditions within the universe, and observation of the universal red-shift has allowed us to make models of the universe of which we are a part. The radiation also carries further information, in the form of the states of polarisation of the light. With advances in astrophysics this data gives us further information on which to base our models and theories.

Interstellar linear polarisation was observed almost by accident in the Forties, and has led to advances in the structure of our galaxy, particularly in the realisation and form of the galactic magnetic field. In the Fifties, observation of polarisation in the Crab Nebula supernova remnant led to the first observation of the effect of synchrotron

radiation in an astronomical object. This effect is paramount in the understanding of conditions within the supernova remnant, and has led to interpretations of radio observations in a wider variety of objects.

The irregular galaxy M82, has been the subject of many investigations, and consequent interpretations over the last two decades. A dominant contribution to the understanding of M82 has been the observation of linear polarisation in the light emanating from this galaxy. Vital information on the conditions within the galaxy has been imprinted on the polarisation of the light, and this information is now becoming available to us.

The work in this thesis, describes efforts made to measure the polarisation to greater accuracy, and at many more points within nebular objects, than previously possible. The possibility of making these measurements, has only become feasible with the advances in recording technique, the electronographic camera, and with the advent of large computers enabling us to manipulate vast quantities of data, to yield the polarisation information. The observations are described and the interpretation of the polarisation data is discussed in terms of current models, of this particular irregular galaxy.

From this work, it is obvious that nebular polarimetry, can make extensive contributions, to the understanding of many forms of astronomical objects

CHAPTER 1

POLARISATION AND ITS MEASUREMENT

1.1 Polarised Light

1.1 1 General Description of Polarised Light

Light is a transverse electro-magnetic vibration. For simplicity in describing polarisation, the light can be considered to be characterised by its electric (E) vector, the amplitude of which varies sinusoidally with both time and position along its direction of propagation. The intensity of the radiation is proportional to the square of the amplitude.

In natural, or unpolarised light, the E vector exhibits no preferred direction in space, and vibrates randomly in the plane perpendicular to the direction of propagation of the beam. An unpolarised wave is diagramatically shown in figure 1.1a. If the direction of vibration is restricted in some manner from its natural randomness, the light is described as being polarised.

1.1.2. Plane and Elliptically Polarised Light

If the plane of vibration of the E vector is restricted to a fixed direction in the X-Y plane of figure 1.1a, the light is described as being plane polarised. A plane polarised wave is illustrated in figure 1.1b, and is characterised by its amplitude, and the angle the allowed plane of vibration makes with a fixed direction in space (in this case, the Y axis).

The amplitude vibration of the E vector can be decomposed into two orthogonal components along the X and Y axes respectively, and these component amplitudes are illustrated in figure 1.1c. The decomposition of plane polarised light is useful when the amount of radiation which can pass through polarising filters needs to be calculated. The component waves shown in figure 1.1c are sinusoidal, and are exactly in phase, so that

(a) Unpolarised Light

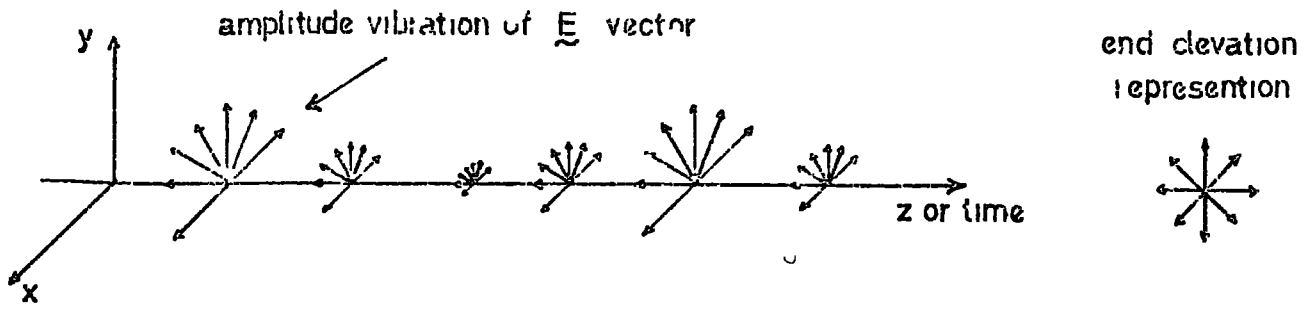

(b) Plane Polarisation

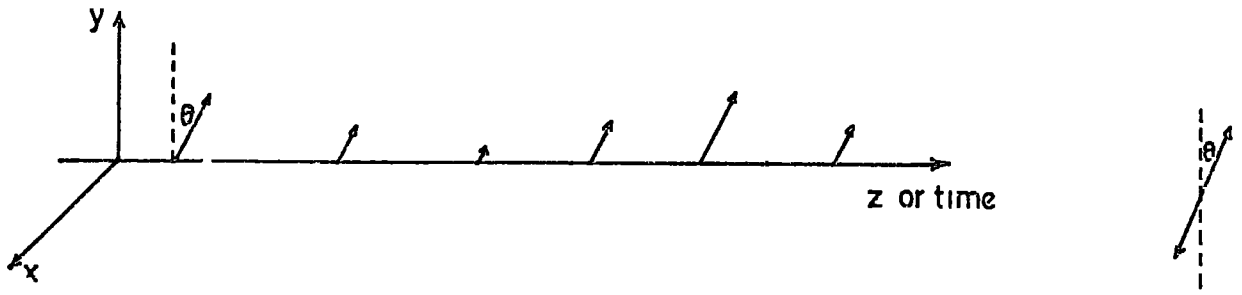

(c) Decomposition of Plane Polarised Light

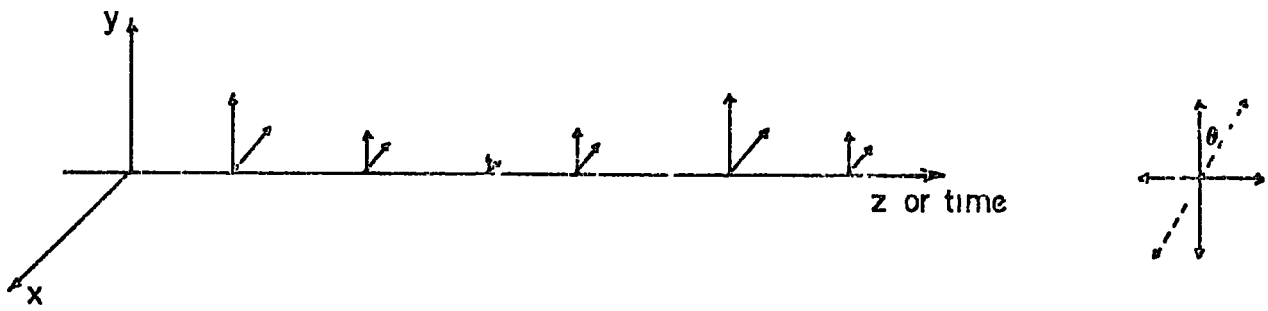

(d) Elliptical Polarisation

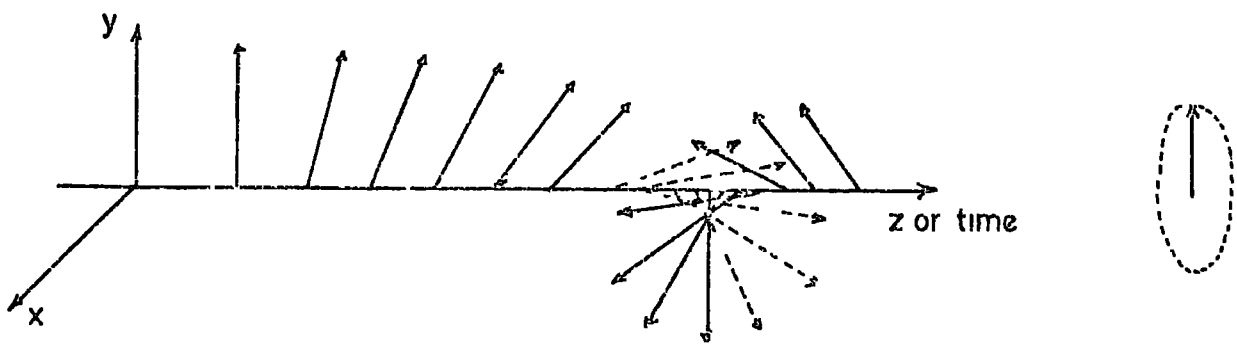

FIG 11 STATES OF POLARISATION

vector addition always produces the resultant wave at a fixed angle (θ in figure 1.1c) For a mixture of plane polarised and natural light, the magnitude, or degree of polarisation is defined as the ratio of the plane polarised and total intensities, and is often expressed as a percentage.

When the two component waves of plane polarised light shown in figure 1.1c, are differentially interfered with so that a phase difference is introduced between them, the resultant E vector no longer gives rise to simple plane polarised radiation, but instead, traces out an ellipse with both time and position along the wave, this is called elliptically polarised light An example of an elliptically polarised wave is shown in figure 1.1d The eccentricity of the ellipse depends upon the amplitudes of the two components, and the phase difference introduced, and for the special case when the component amplitudes are equal and the difference in phase angle is 90^{o}, the major and minor axes are of equal length, and the radiation is described as being circularly polarised.

1.2 The Occurrence of Plane Polarised Light in Nature

There are several mechanisms for the production of partially or completely plane polarised radiation in nature The scattering of incident natural light on particles of all shapes and sizes, from electrons to macroscopic surfaces, or the transmission of light through aligned non spherical dust grains results in the production of partially plane polarised radiation. The acceleration of charged particles in magnetic fields gives rise to completely plane polarised light, called synchrotron radiation.

The production of elliptical polarisation however, is usually a two

stage process, in which plane polarised light must first be produced by one of the above methods. A phase difference between one of the original components is then introduced by transmission through a birefringent medium. Partially plane polarised light might be expected to occur abundantly in nature therefore, while its elliptical counterpart is more of a rarity and is present in much diluted quantities only.

Each of the plane polarisation production mechanisms imprints its stamp on the form of the polarisation obtained. Investigation of the polarised nature of light emitted from distant, extra-terrestrial objects, can therefore give an insight into some of the physical conditions present at the source, and along the path of the radiation.

1.3 The Simple Measurement of Partial Plane Polarisation

For the analysis of plane polarisation, the light is usually passed through a polarising filter, (for example a piece of polaroid), which only transmits the E vector component of the radiation parallel to a certain allowed direction. The filter is calibrated so that the orientation of the allowed axis is known, and the intensity of the transmitted radiation for a particular filter orientation is recorded photo-electrically, or on a photographic plate.

A series of four measurements are taken at filter angles of 0, 90, 45 and -45 degrees respectively, and the transmitted intensities I_1-I_4 are recorded in each case. In figure 1.2 a beam of total intensity, I which is the sum of a plane polarised component of intensity 'Ip', at an angle to the vertical, and an unpolarised component of intensity 'I - Ip', is shown before and after transmission through the filter, for each of the orientations. In each case, the relationship between the recorded inten-

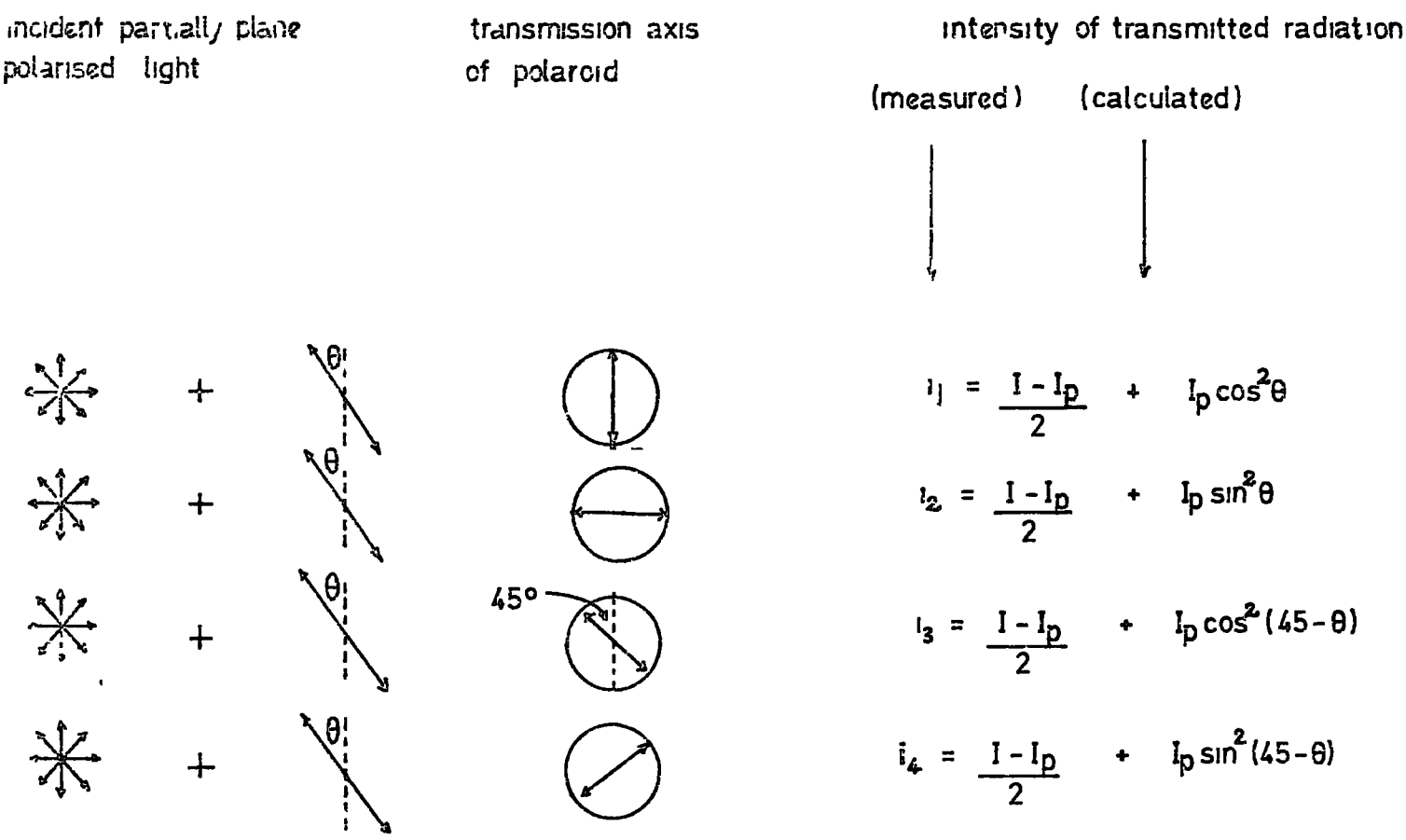

FIG 1 2 SIMPLE MEASUREMENT OF PLANE POLARISATION

sities $(i_1 - i_4)$, and the derived intensities in terms of the required quantities (I, Ip, θ) are shown. It is therefore a simple matter to solve the four simultaneous equations to obtain (I, Ip, θ) in terms of the measured quantities $(i_1 - i_4)$.

Defining 2 quantities Q, and U by the following equations:

$$Q = i_1 - i_2 = Ip \cos 2\theta \qquad 1.1$$

$$U = i_3 - i_4 = Ip \sin 2\theta \qquad 1.2$$

Then equations 1.1 and 1.2 can easily be solved for Ip, to give,

$$Ip = \sqrt{Q^2 + U^2} = \sqrt{(i_1 - i_2)^2 + (i_3 - i_4)^2} \qquad 1.3$$

$$\theta = 0.5 \arctan (U/Q) \qquad 1.4$$

The final required parameter, the total intensity I is simply given by,

$$I = i_1 + i_2 = i_3 + i_4 \qquad 1.5$$

because of the orthogonally polarised nature of the measurements. The ratio of the polarised and total intensities can be calculated to give the percentage polarisation of the incident beam.

$$P = Ip/I \times 100 \qquad 1.6$$

It follows that a simple series of four measurements, uniquely determines the polarisation for an incident beam of partially plane polarised light.

1.4 Elliptical Polarisation

Although the amount of elliptically polarised light from the astronomical objects is expected to be small, it is of interest to inquire

into the effect of having a small amount of elliptically polarised light, contaminating the plane polarised beam analysed in the previous section.

Using the simple method outlined, it is not possible to determine if the incident light has an elliptically polarised component, as three more parameters, intensity, ellipticity, and angle of major axis with reference direction, are required for a full specification. A total number of six unknowns would therefore be introduced into the four simultaneous equations. It is possible however, to ascertain the error induced into the measurement of plane polarisation, using the simple method, for a mixture which contains a small amount of elliptically polarised light.

In figure 1.3, an elliptically polarised component of minor axis amplitude 'b' and major axis amplitude 'a', at an angle 'ϕ' to the vertical reference direction, is added to the incident radiation. The derived intensities for this 'perturbed' beam, are again equated to the measured intensities ($i_1' - i_4'$).

Following the basic theory of 1.3,

$$Q' = i_1' - i_2' = (a^2 - b^2) \cos 2\phi + Ip \cos 2\theta \qquad 1.7$$

$$U' = i_3' - i_4' = (a^2 - b^2) \sin 2\phi + Ip \sin 2\theta \qquad 1.8$$

and the two parameters describing the plane polarised component are estimated as

$$Ip'^2 = Q'^2 + U'^2 = (a^2 - b^2)^2 + Ip^2 + (a^2 - b^2)\, Ip \cos 2(\phi - \theta) \qquad 1.9$$

$$\theta' = 0.5 \arctan (U'/Q') = 0.5 \arctan \frac{(a^2 - b^2) \sin 2\phi + Ip \sin 2\theta}{(a^2 - b^2) \cos 2\phi + Ip \cos 2\theta} \qquad 1.10$$

Inspection of 1.9 and 1.10 shows that the calculated values of the

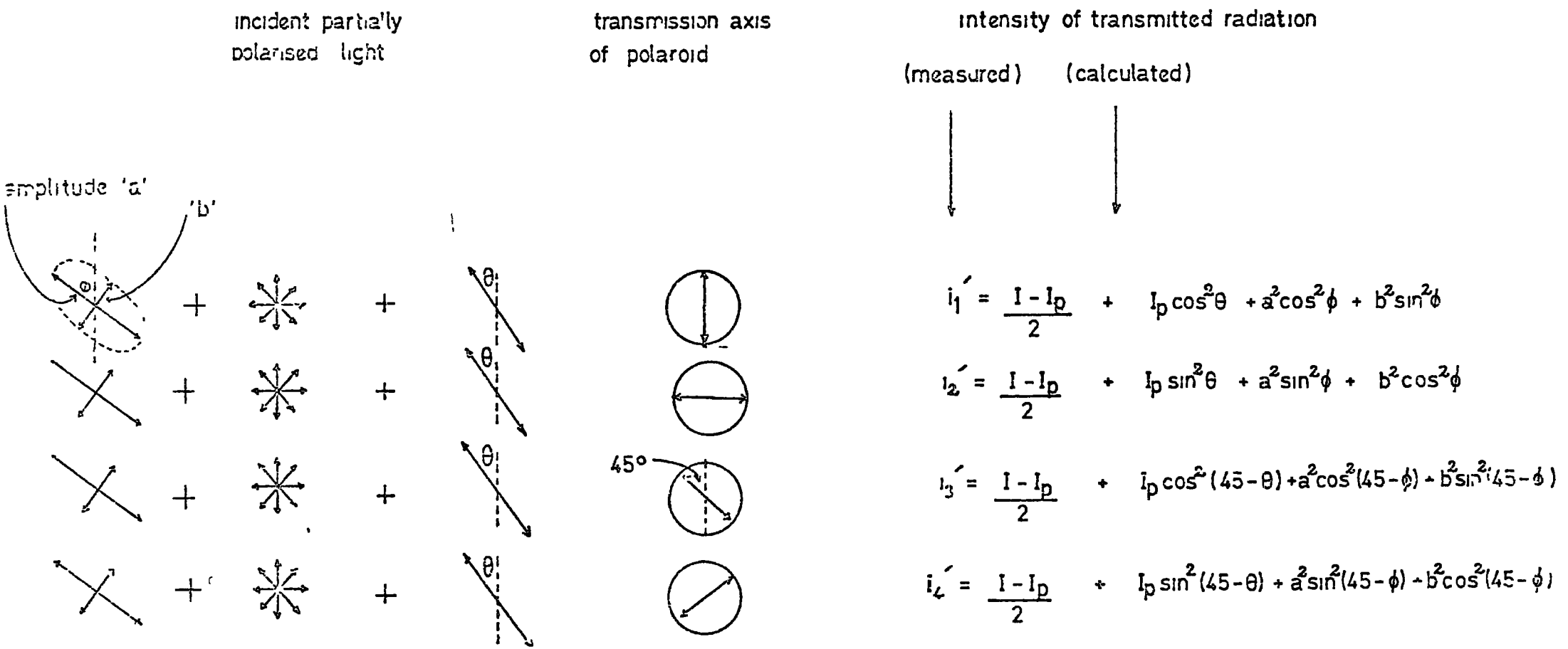

FIG 1 3 THE PERTURBATION CAUSED BY ELLIPTICAL POLARISATION

plane polarisation parameters, (Ip', θ') are not the true values,

$$Ip' = Ip \qquad \theta' = \theta, \tag{1.11}$$

but are perturbed by additional terms, caused by the presence of the elliptical polarisation.

The perturbation from the true values is small, providing the proportion of elliptically to plane polarised light is small ($a^2 + b^2 < Ip$), and equations 1.9 and 1.10 reduce exactly to equations 1.11 if the intensity of the elliptically polarised component is zero ($a^2 + b^2 = 0$)

For an incident beam containing 5% plane polarised and 0.5% elliptically polarised light of eccentricity 0.5, the maximum error introduced into the measurement of the plane polarisation parameters, is 0.2% in degree and 1 5° in direction Equations 1.9 and 1.10 show that the correction terms are in fact proportional to ($a^2 - b^2$), which is a measure of the eccentricity of the ellipse, and they therefore approach zero as the elliptical polarisation tends to circular polarisation ($a^2 = b^2$), independently of the total intensity ($a^2 + b^2$).

1.5 The Stokes Vectors

The degree of polarisation and angle of preferred vibration which are convenient parameters to describe a partially polarised beam, are scalar quantities, which together form a representation of the electric vector of the incident light As a consequence of this, it is not possible to simply add them when two incident beams of known (I, Ip, θ) are combined, to find the parameters of the resultant beam In the same

way, if several estimates of (Ip, θ) for the same beam are calculated, straight averages do not result in the correct value of the mean.

A set of quantities, which are simply related for the former ones, but are additive in nature, were defined by Stokes, to describe any beam of polarised radiation. The 'Stokes vectors' defined by,

$$I = \text{Total intensity of beam} \qquad 1.12$$

$$Q = Ip \cos 2\theta \qquad 1.13$$

$$U = Ip \sin 2\theta \qquad 1.14$$

may be mathematically manipulated as required, before returning to the convenient descriptive units for the final result Inspection of section 1.3 shows that the quantities arbitrarily defined as I, Q, U, are in fact the Stokes vectors of the partially plane polarised radiation These quantities could therefore be averaged, if a series of measurements ($I_1 - I_4$) were recorded several times for the same source, before finally returning to the descriptive units via the transformation

$$\bar{\theta} = 0.5 \arctan (\bar{U}/\bar{Q}) \qquad 1.15$$

$$\bar{p} = \sqrt{\bar{Q}^2 + \bar{U}^2} \; / \; \bar{I} \qquad 1.16$$

A fourth Stokes vector, 'V', exists which describe any elliptically polarised component of the radiation.

CHAPTER 2

THE DURHAM POLARIMETER AND 4 CM. ELECTRONOGRAPHIC CAMERA

2.1 Introduction

The Durham polarimeter was designed to detect and measure the degree to which incident light is partially plane polarised. The original prototype polarimeter, based on a design by Öhman (1939), is described by D.J. Axon (1976), who did most of the laboratory testing. In this thesis, the present polarimeter is described, which is essentially the same as the prototype in principle, but the optical components were rebuilt into a sturdy steel framed aluminium housing and the original monochromatic half wave plate was replaced by one which is approximately achromatic over the wavelength range 3900 - 4900 Å, and a new 4 cm. Wollaston prism was incorporated into the structure.

2.2 The Light Path through the Polarimeter

The components of the polarimeter shown in plates 1-5 are drawn diagrammatically in figure 2.1, and a particular 'light ray' entering the polarimeter from the telescope, is traced through the optical components.

When a particular object is imaged on the grids, the polarimeter 'sees' the part of the image contained in the series of vertical gaps formed by the grids. The light from those parts of the image which are formed behind the solid grid bars, is absorbed. The light from the image contained in the vertical gaps passes through the polarising components of the polarimeter, and is finally reimaged by the relay lens. This image can then be recorded by means of a photographic plate or, as used in the present case, an electronographic camera. The ray

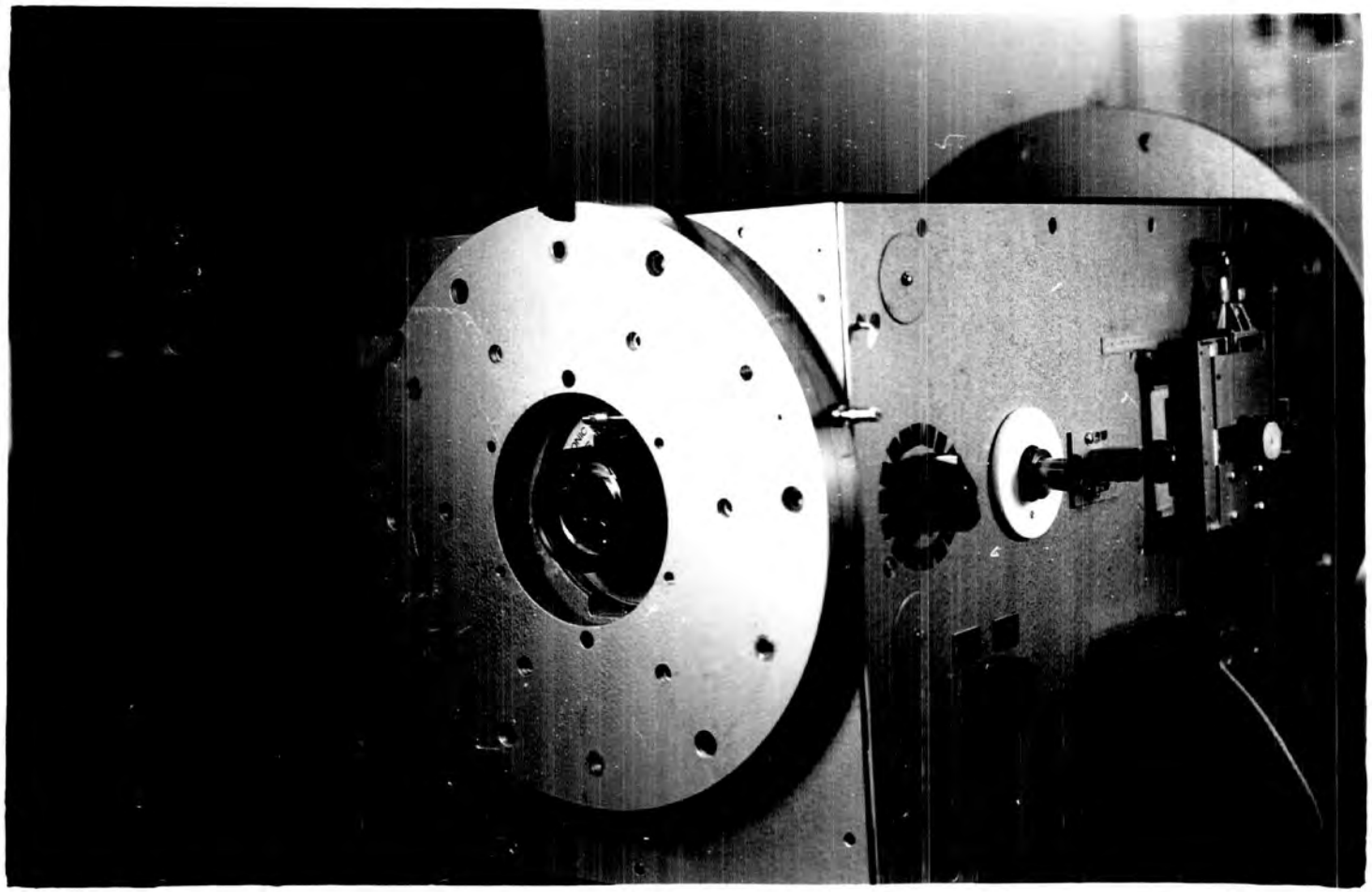

PLATE 1

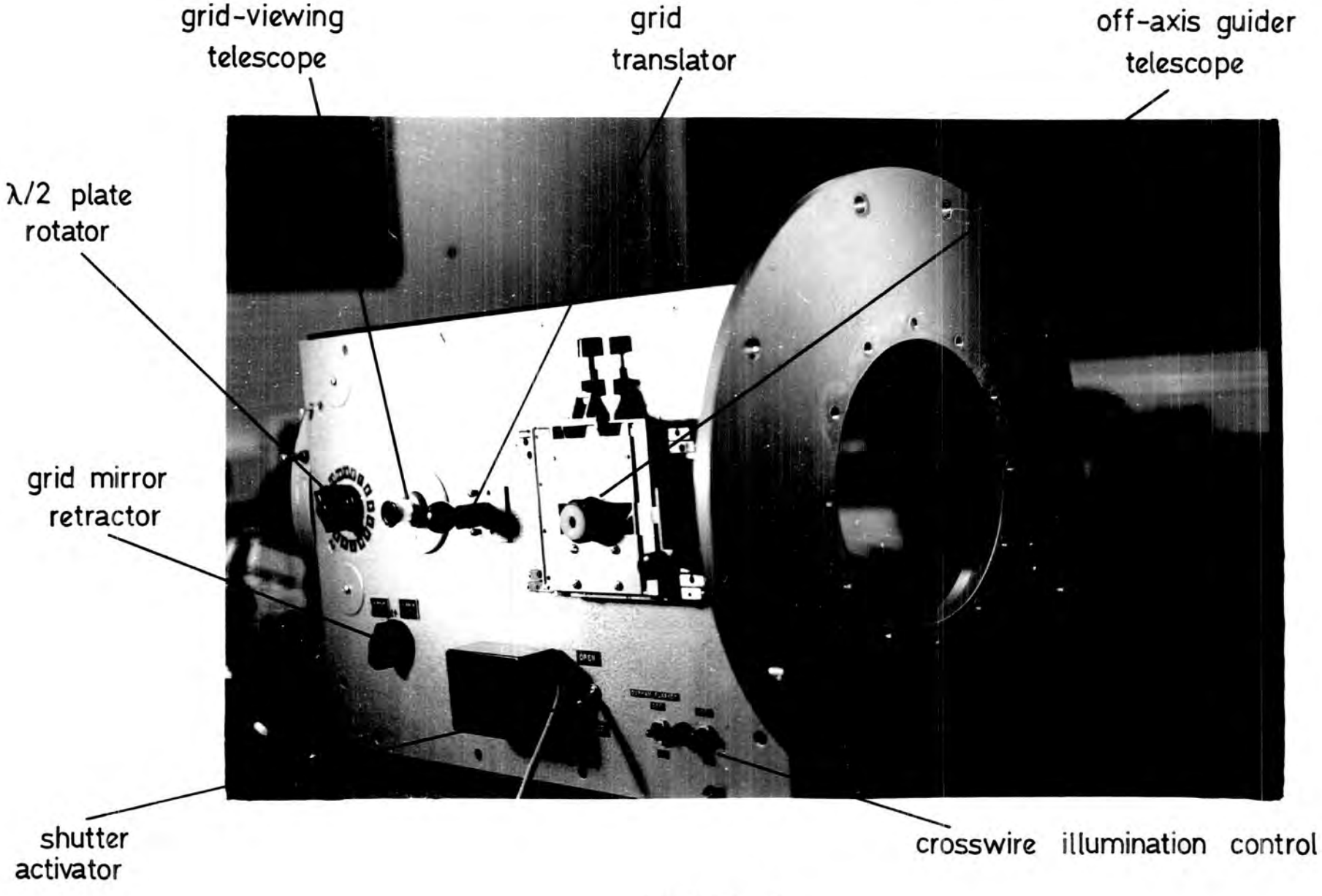
grid-viewing telescope
grid translator
off-axis guider telescope
λ/2 plate rotator
grid mirror retractor
shutter activator
crosswire illumination control

PLATE 2

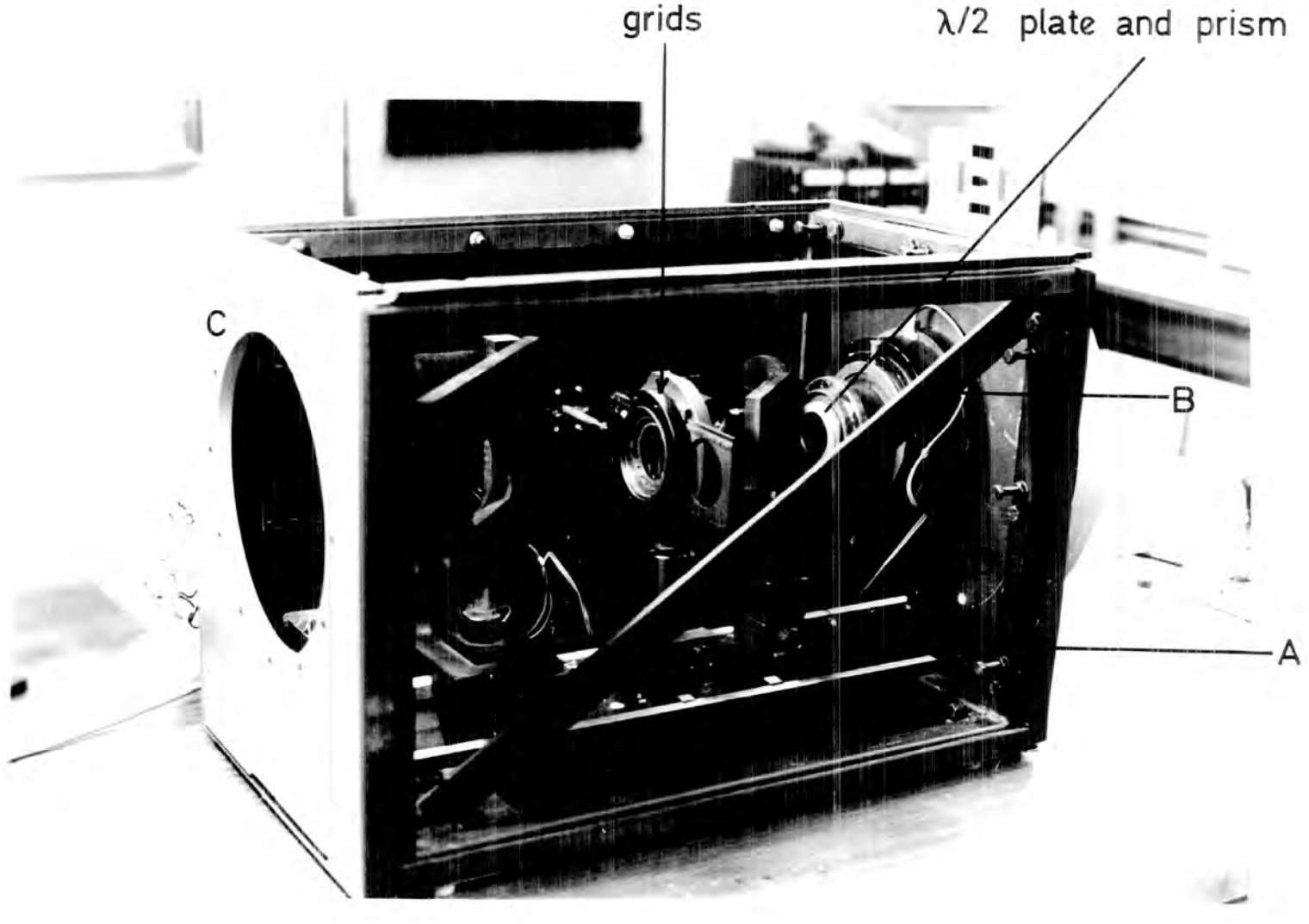

PLATE 3

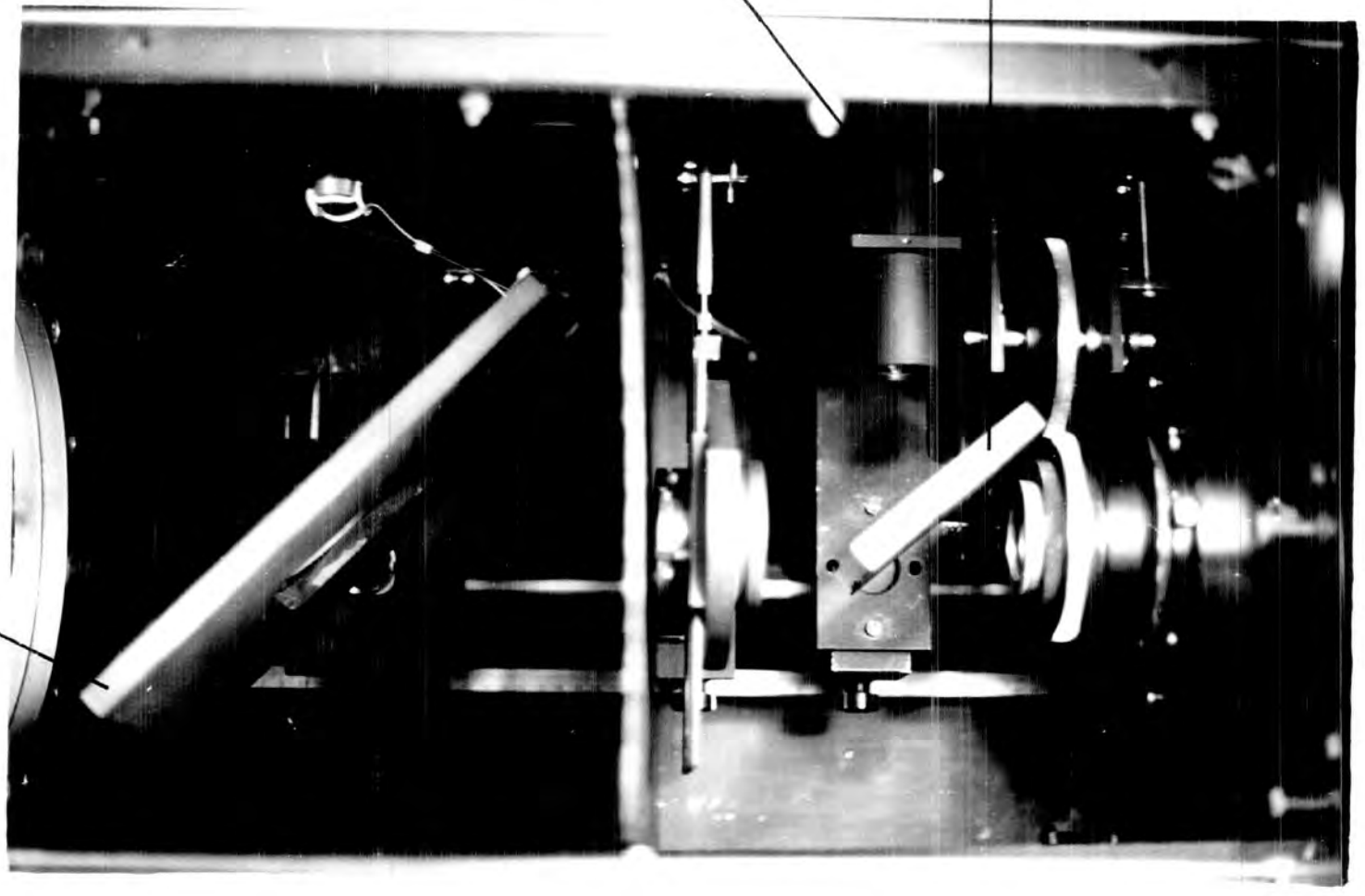
grid viewing telescope
grid viewing mirror
off-axis
guider mirror

PLATE 4

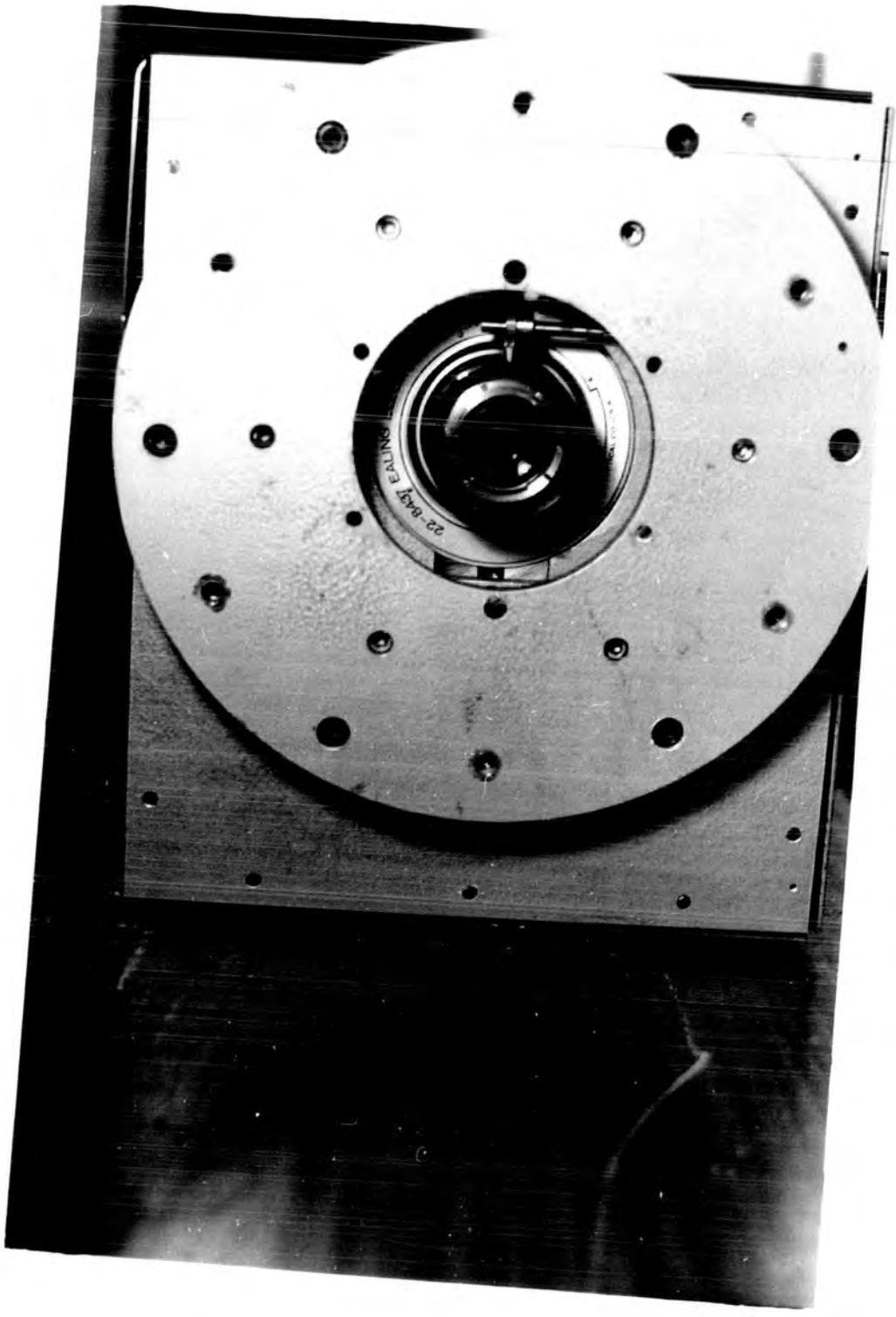

PLATE 5

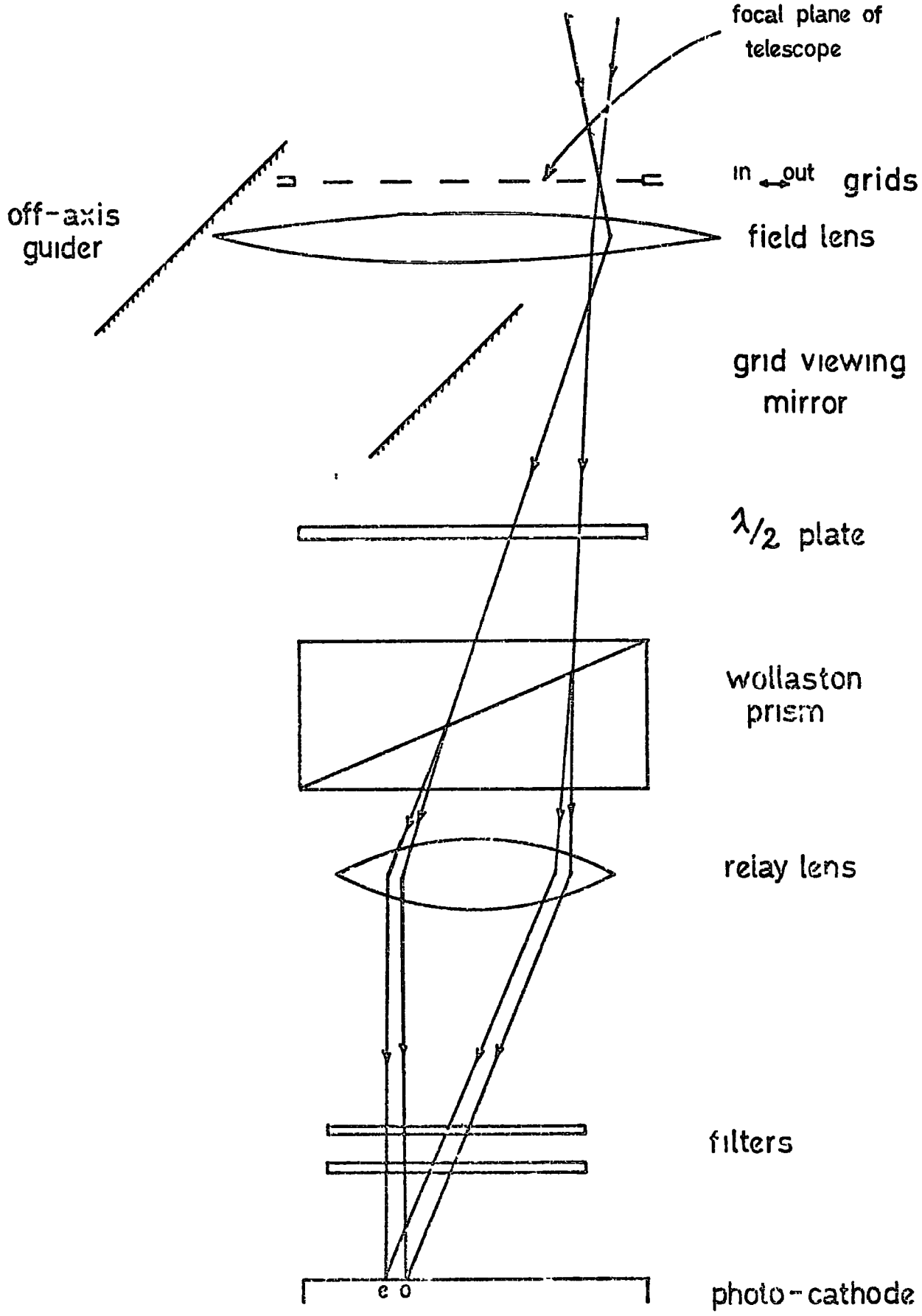

FIG 21 RAY DIAGRAM OF THE POLARIMETER

diagram shown traces the light path of a particular small element of the astronomical image (formed in the plane of the grids), through the analysing components.

The incident light, forming any point of the image on the grids, is contained in a cone of width 4^{o} because the telescope is used at f/13.5 focus. The beam of light passing through the grid gaps is approximately 4 cm. in diameter, and is condensed by means of the field lens so that it can pass through the limiting aperture ($\sim$ 1") formed by the half wave plate. The light from any point on the grid image then passes through the halfwave plate, which rotates the plane of polarisation of any plane polarised component, but does not deviate the ray. Transmission through the prism, splits the ray into two orthogonally polarised components, and also introduced a deviation of 1^{o} (in the horizontal plane) between them. If the incident light is unpolarised, these two rays will be of equal intensity. Any deviation from this equipartition indicates that a plane polarised component is present. The two rays are then brought to their separate foci (displaced in the horizontal plane), on the camera photocathode by the field lens.

Each element of the grid therefore forms two images, in orthogonally polarised light on the photo-cathode. The net effect is, that each of the spaced vertical bars forming the total grid 'object', are split into two orthogonally polarised components, and are re-imaged (with a horizontal displacement between them), on the camera photo-cathode. A schematic illustration of a particular grid 'object', and the resultant photocathode image are shown in figure 2.2 Rotation of the half wave plate, changes the relative amplitudes of the E vectors forming the two

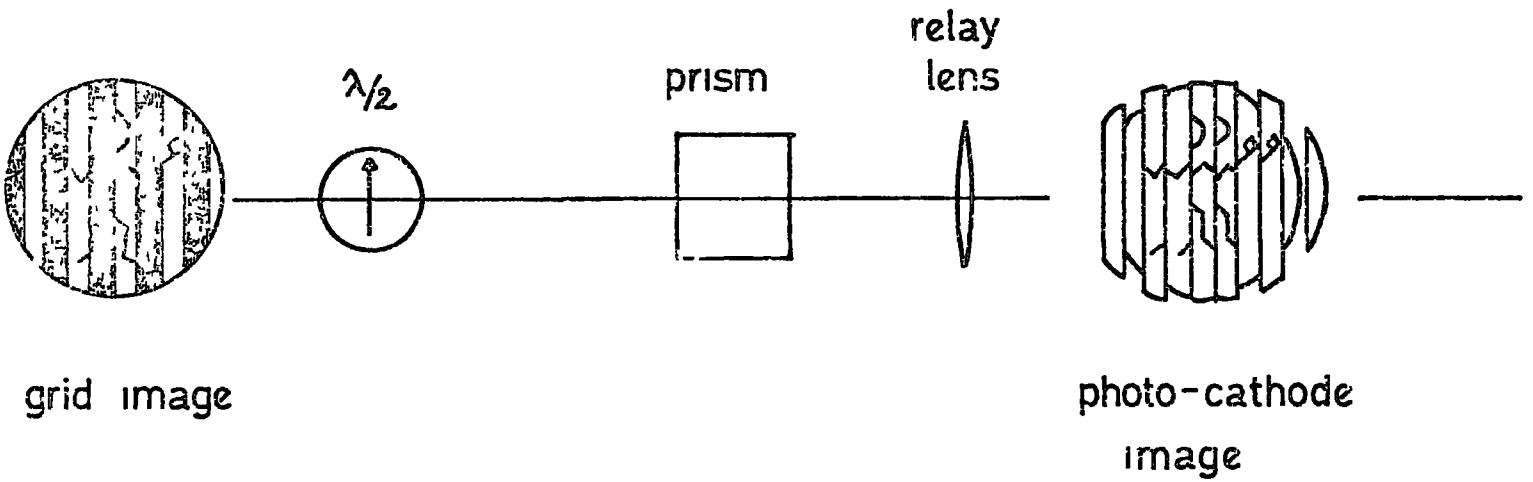

FIG. 2 2 THE GRID AND PHOTO-CATHODE IMAGES

polarised images, but does not affect its spatial appearance. The linear distances of the components along the principle axis of the polarimeter are arranged so that the pairs of horizontally displaced grid images just touch but do not interfere with each other.

To summarise, electronographs can be taken with the half wave plate at different orientations, and the spatial appearance of the final image is the same in each case Comparison of the relative densities, for the pairs of images formed on different plates, is a direct measure of the amount of plane polarised radiation in the light coming from the astronomical object, and forming that particular part of the image.

2.3 Description of the Polarimeter

2.3.1. The Shell

The frame of the polarimeter is composed of $\frac{3}{4}$' square steel section (A), and is reinforced with diagonal struts (B). The strength of the chassis is extremely important, as it must be capable of taking the 120 lb weight of the electron camera without any significant distortion.

The end plates (C and D), with which the polarimeter is bolted to the telescope and camera respectively, are $\frac{1}{2}$" aluminium plate, and are attached to the framework of the polarimeter with adjustable bolts, so that the whole apparatus can be aligned with the plane of the end plates perpendicular to the principal axis of the polarimeter. The sideplates, whose only purpose is to make the instrument light tight, and provide mountings for the adjusting knobs are $\frac{1}{8}$" aluminium plate.

2.3 2. The Wollaston Prism

The prism, which is illustrated in figure 2.3, is made from two

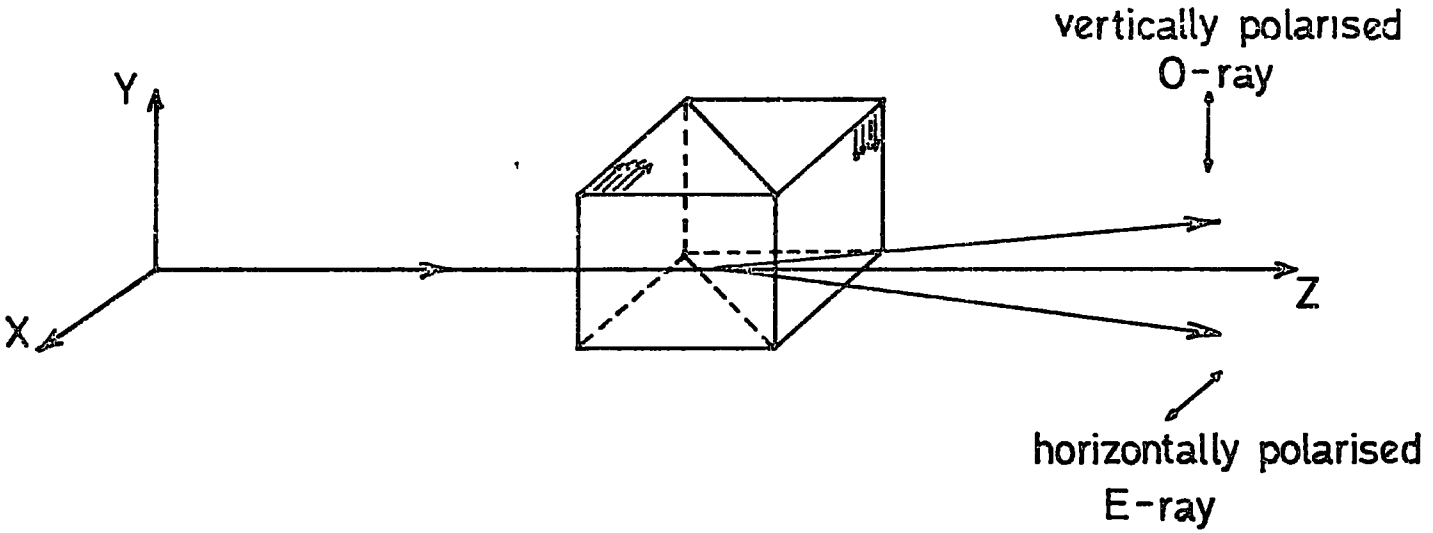

FIG 23 THE ACTION OF THE WOLLASTON PRISM

pieces of quartz cemented together with their optic axes perpendicular. The incident radiation is split into two orthogonally polarised components, (O and E rays), on entering the prism, because of the directional dependence of the refractive index of a birefringent material. At the boundary between the two segments, the two rays interchange identities because of the perpendicular optic axes of the two component parts of the prism, and are therefore refracted due to the apparent change in refractive index. The symmetry involved, implies that the two rays are each deviated from the normal by the same amount, as shown in figure 2.3.

The magnitude of the deviation is dependent on the angle at which the prism is cut, and, because it depends in the difference in refractive indices, rather than their absolute value, it is not very sensitive to wavelength. The prism used, which had a deviation of 1^{o}, was mounted in the polarimeter, so that the diverging, orthogonally polarised rays, were in the horizontal plane.

2.3.3. The Achromatic Half Wave Plate

The half wave plate consists essentially of a plane section of birefringent material, cut parallel to the optic axis which splits the incident radiation into orthogonally polarised O and E ray components. As described in the previous section, the two rays have different velocities in the material, but are not deviated as they travel normal to the optic axis and so they emerge with a net phase difference, given by

$$\delta = \frac{2\pi}{\lambda} \cdot d. (n_o - n_e) \qquad 2.1$$

where λ is the wavelength of the incident radiation, d, the thickness of the material, and n_o and n_e, the refractive indices of the plate for the O and E rays respectively. To satisfy the half wave plate condition, the value of d is adjusted so that

$$\delta = (2m + 1)\,\pi \qquad 2.2$$

where m takes on positive integer values. The two rays therefore recombine 180^o out of phase after transmission.

Equation 2.1 shows that the retardence is wavelength dependent, so that the required thickness of material can only give exact $\lambda/2$ properties at a specified wavelength. This disadvantage can be overcome by using a multi-layer plate made from different materials, so that the individual wavelength dependences approximately cancel out. The transmission of plane polarised light through the half wave plate causes the plane of polarisation to be rotated through twice the angle the incident radiation makes with the optic axis of the crystal. This is illustrated in figure 2.4a.

A 1" diameter, 2 layer plate made from magnesium fluoride and quartz was used in the polarimeter. The achromatism of the plate, which was designed for use in the wavelength range 3,900 - 4,900 $\mathring{A}$, (corresponding to B of the UBV system), was laboratory tested at Durham, and the variation of retardence with wavelength is shown in figure 2.4b. The plate was bloomed, to reduce light loss by reflection at both the incident and transmission surfaces.

The half wave plate is mounted into a rotateable housing, and is rotated by means of a set of bevel gears from outside the polarimeter

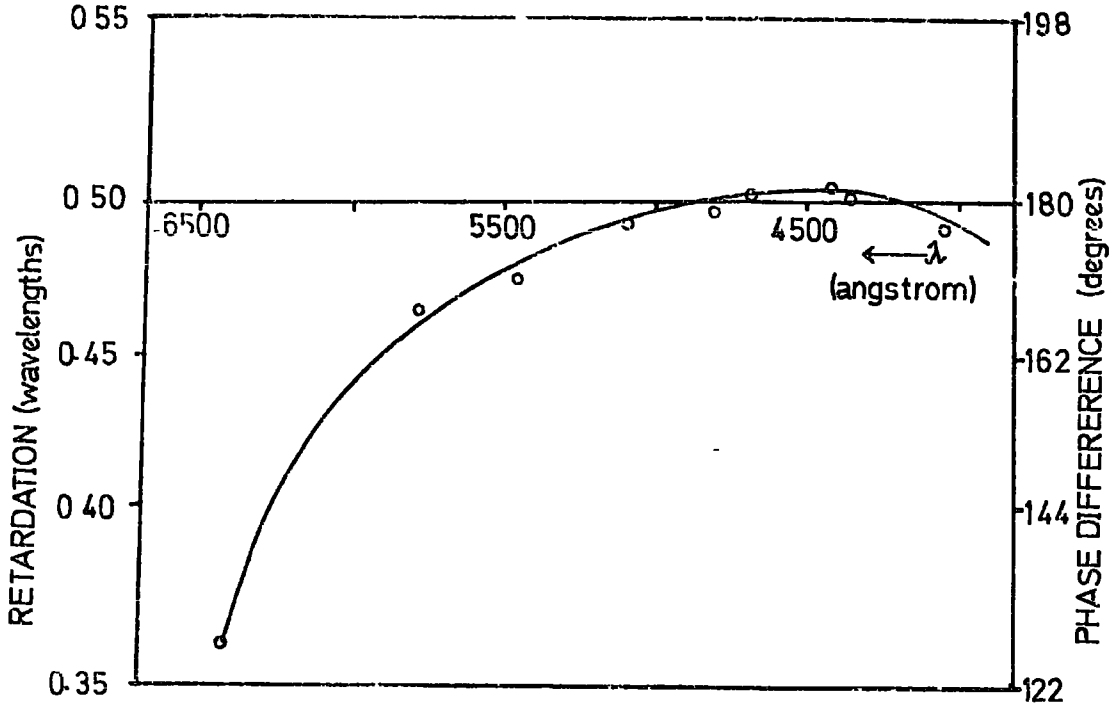

FIG 24a THE RETARDENCE OE THE $\lambda/2$ PLATE

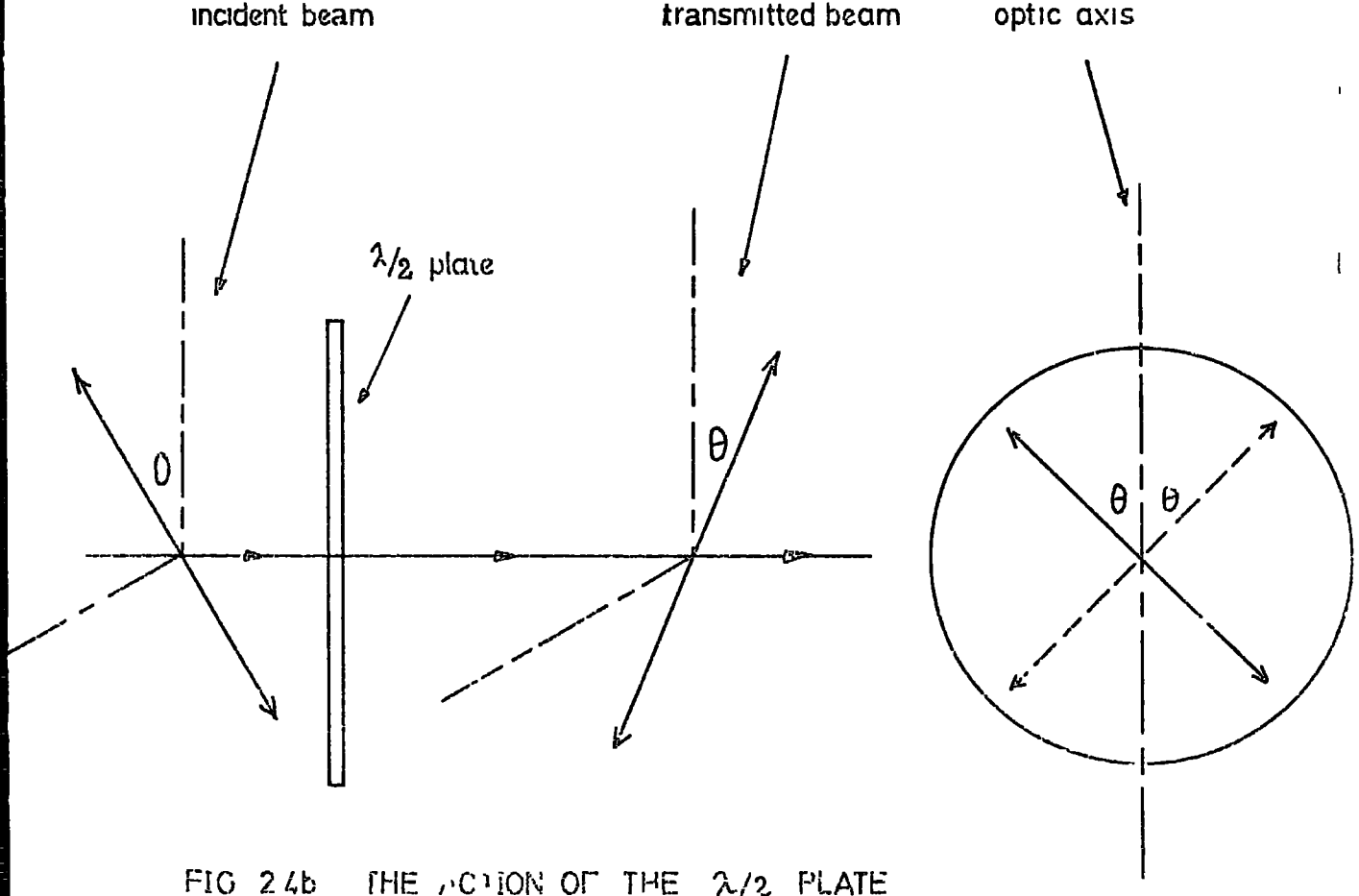

FIG 24b THE ACTION OF THE $\lambda/2$ PLATE

2.3.4. The Grid System

The grid system is mounted on an optical bench, running along the base of the polarimeter, and the constructional details are shown in plate 3. The actual grids are accurately machined from perspex, and have equal bars and gaps of width 3.1 mm. They are placed in the focal plane of the telescope, using f/13.5 Cassegrain focus, when 1 mm. across the grids corresponds to approximately 16 seconds of arc (for the 1 m telescope on which the observations were made). The grids can be moved in a horizontal direction across the focal plane of the telescope, and have adjustable stops to limit the extent of this motion The outside of the grids is covered with a thin annulus of polaroid, which is used for calibration purposes.

An aperture of 4 cms. is used when observing, which gives a total unvignetted field of 8 minutes of arc approximately. Three lengths of 20 micron diameter gold wire, are attached at right angles to the grids, and are used to ensure that the grids are accurately focussed on the photo-cathode of the 4 cm McMullan camera, used to record the images

Positioned on the same mount, and after the grids (along the light path), is the field lens, a 5 cm diameter, 20 cm. focal length achromatic doublet, which acts as a condensing lens, to ensure that all light emerging from the grids is sufficiently converged to pass through the limiting apertures of the analysing components.

2.3.5 The Relay Lens and Shutter

The relay lens and shutter are mounted into the end plate of the

polarimeter, as shown in plate 5. The shutter is electrically activated by means of a solenoid, the controlling switch being mounted on the control panel.

The relay lens is a Nikon f/1.4 camera lens of focal length 50 mm, and is bloomed to reduce unwanted reflection. The whole lens housing can be moved along the principal axis of the polarimeter by means of a rack and pinion gearing operated from the control panel to accurately focus the grids onto the photo-cathode. The focal length, and positioning of the relay lens, introduces a 4x demagnification between telescope and photo-cathode images. This results in a similar gain in speed, which is important when faint nebulous objects are under observation.

2.3.6. The Off Axis Guider and Grid Viewing Mirror

The off axis guider consists of a large plane mirror of aluminised perspex, mounted at 45° to the principle axis of the polarimeter. The mirror has an elliptical hole of minor axis $\sim$ 5 cm, in the centre to allow the axial light to reach the polarimeter.

The 'off axis' light is reflected, and brought to focus on illuminated crosswires, which are viewed with the off axis guider eyepiece, mounted on the control panel. The crosswires are illuminated with 2 battery operated light emitting diodes which emit most of their power in the red region of the spectrum, and do not interfere with the telescope light to be analysed, which is confined to the B waveband. The eyepiece, which is shown in plate 2, can be racked in both horizontal and vertical directions to scan the field provided by the 45° mirror for stars, which can be used for guiding purposes.

The grid-image viewing mirror (plate 4), can be rotated into the light path at 45° between the grids and half wave plate to deliver the light to a telescope mounted on the control panel so that the astronomical image formed on the grids can be viewed. This is necessary before an exposure is taken, to ensure that the object is centrally placed in the field of view, and is also used to focus the telescope image onto the grid system.

2.3.7. Filters

A BG12 filter was used to isolate the required optical wavelength range from 3,900 - 4,900 Å. The transmission curve is shown in figure 2.5 A second BG38 filter absorbs the infra-red wavelengths, which are transmitted by the BG12 filter, and for which the camera photo-cathode is still slightly sensitive. The filters are mounted over the relay lens, by means of a brass adaptor. The field lens does not transmit at wavelengths less than 3,900 Å.

2.4 The Electronographic Camera

2.4.1. Introduction

The images formed by the polarimeter, which contain the required information concerning the state of polarisation of the object, were recorded on a 4 cm. McMullan camera, recently developed at the Royal Greenwich Observatory (D. McMullan et al 1972).

2.4.2. The Principle of the Electronographic Camera

The basic idea of the electronographic camera, is that the photon image is converted into electrons, and these are accelerated and recorded,

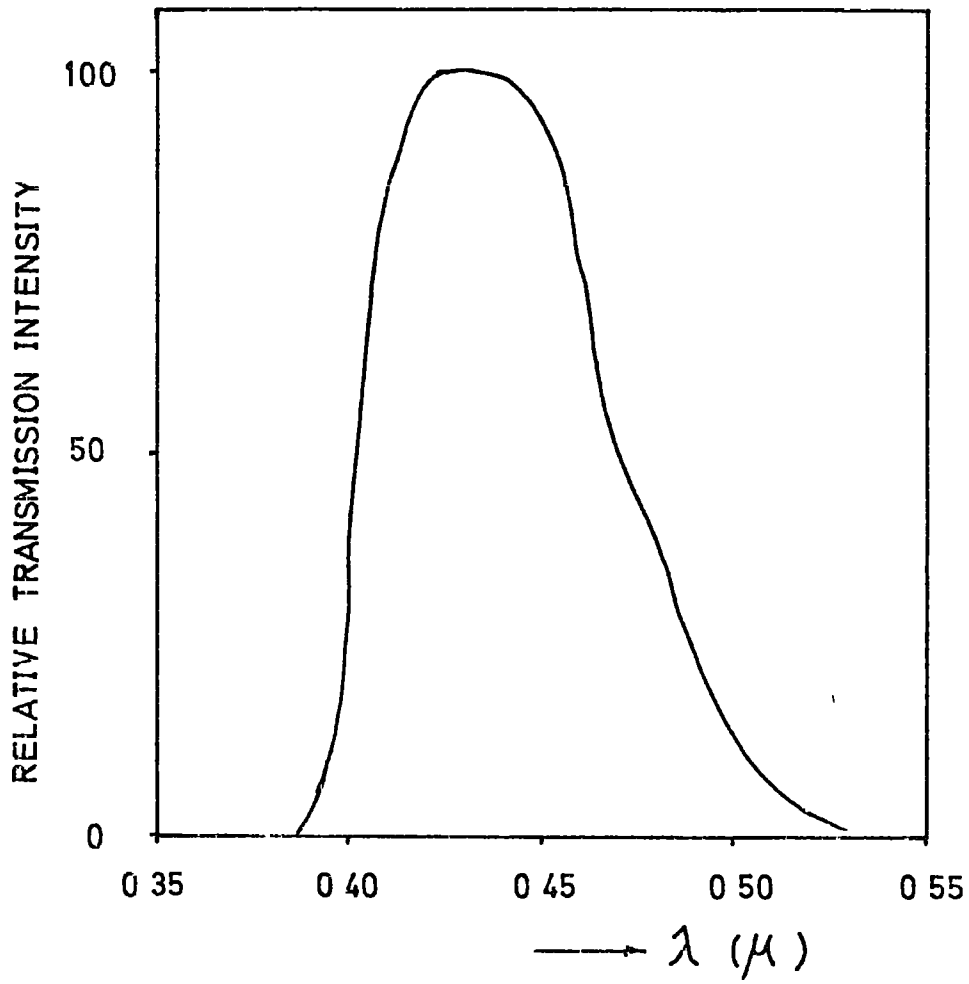

FIG 25 THE TRANSMISSION CURVE OF THE BG12 FILTER

to give an 'amplified' image.

Light from the object to be photographed, is imaged onto a photo-sensitive surface in vacuum surroundings. Each incident photon has a relatively high probability of releasing a photo-electron. The electrons coming from the surface, with essentially zero energy (Electron energy = energy of photon - work function $\sim$ eV), are electrostatically accelerated by a large potential difference along the tube ($\sim$ 40 K.V.), and then magnetically refocussed through a thin transparent, mica window which seals the other end of the tube, onto a film of nuclear emulsion. Although the window is only a few microns thick, 30% of the electrons are absorbed in the mica. The emulsion, which forms a thin layer, on a melánex backing, is pressure sealed against the mica window Each of the high energy electrons leave a track in the emulsion, which can later be 'developed', to reveal an apparent optical negative of the object.

The difficulty in practice is that the mica window, which must be very thin to be transparent to the electrons, will not withstand atmospheric pressure on one side, and high vacuum on the chamber side This difficulty has been overcome in the McMullan camera, by having the emulsion side at low pressure, ($\lesssim$ 1 torr), and a series of valves and chambers, to facilitate loading and unloading the camera, without exposing the window to atmospheric pressure

2.4.3 Description of the Camera

Plate 6 shows the camera attached to the polarimeter, which is in turn mounted on the 1 m telescope of the Wise Observatory, Israel,

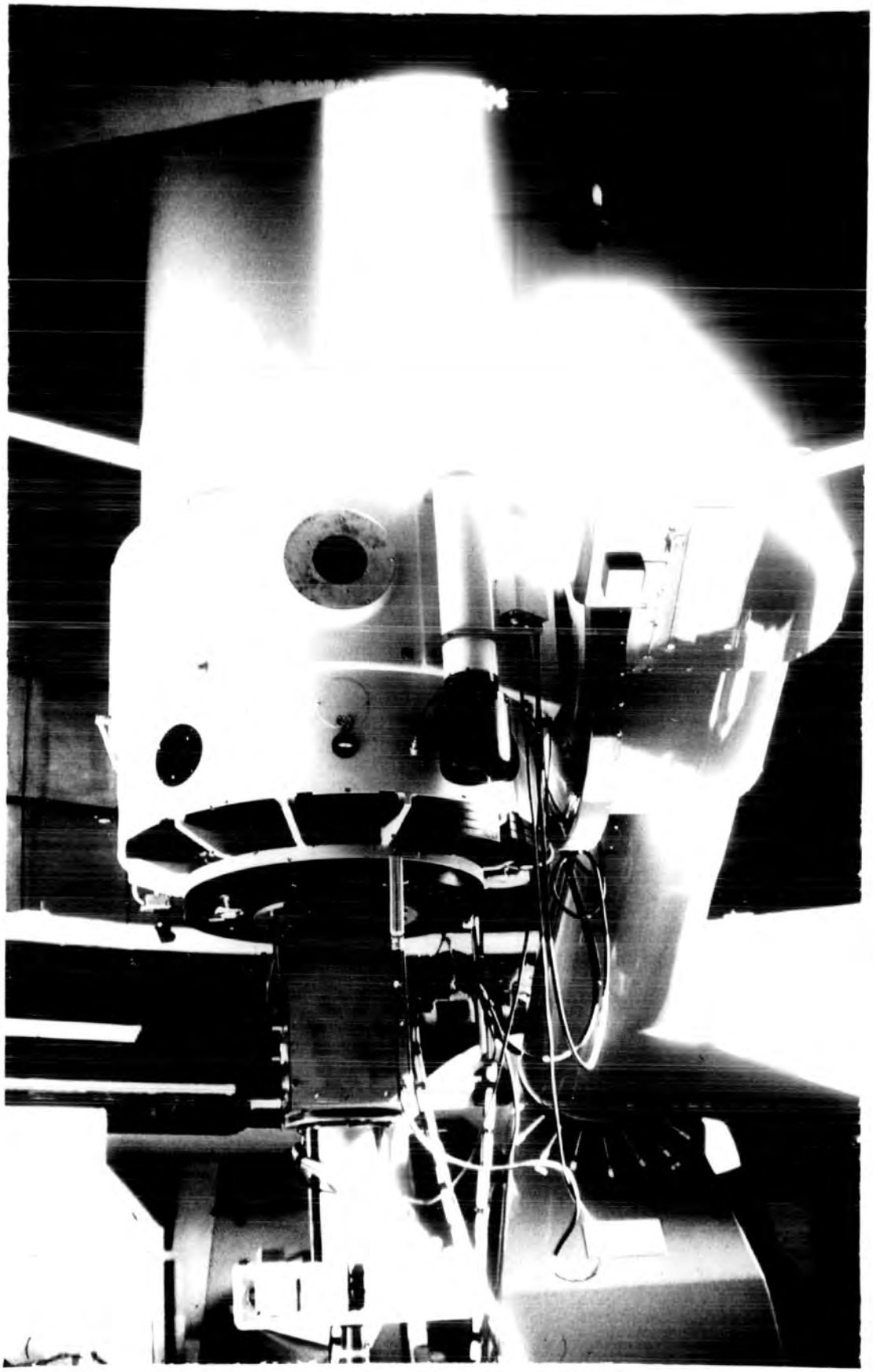

PLATE 6

where the present observations were made. A cross section through the camera is shown in figure 2.6.

The camera can be divided into 3 distinct parts.

Firstly, the long, tubular structure which incorporates the photo-cathode, vacuum tube, focussing coils and the mica window. Secondly, the rectangular base which contains relays and pumping equipment for the tube, and has the control box mounted on it. Finally, the applicator, on which the emulsion is mounted, inserted, and vacuum sealed into the camera.

The base, into which the applicator is inserted, has two vacuum chambers as shown in figure 2.6. The loading procedure is therefore to insert the applicator, which seals chamber A, and then evacuate this chamber. Chamber B, which is in contact with the mica window is continuously maintained at 1 torr, and is connected by the gate valve to chamber A. When chamber A is evacuated, the gate valve opens, and the end of the applicator on which the emulsion is mounted is moved up to the mica window. The exposure is taken, and then the procedure is reversed to extract the emulsion, without subjecting the mica window to atmospheric pressure.

2.4.4. Advantages of the Electronographic Camera

The detector quantum efficiency of the electronographic camera, is wavelength dependent, and has a peak value of approximately 10% at 5,000 Å, for the S 20 extended photo-cathode used during the present observations. This compares favourably with the most recent photographic plates, (even after electron loss has been considered) which struggle to

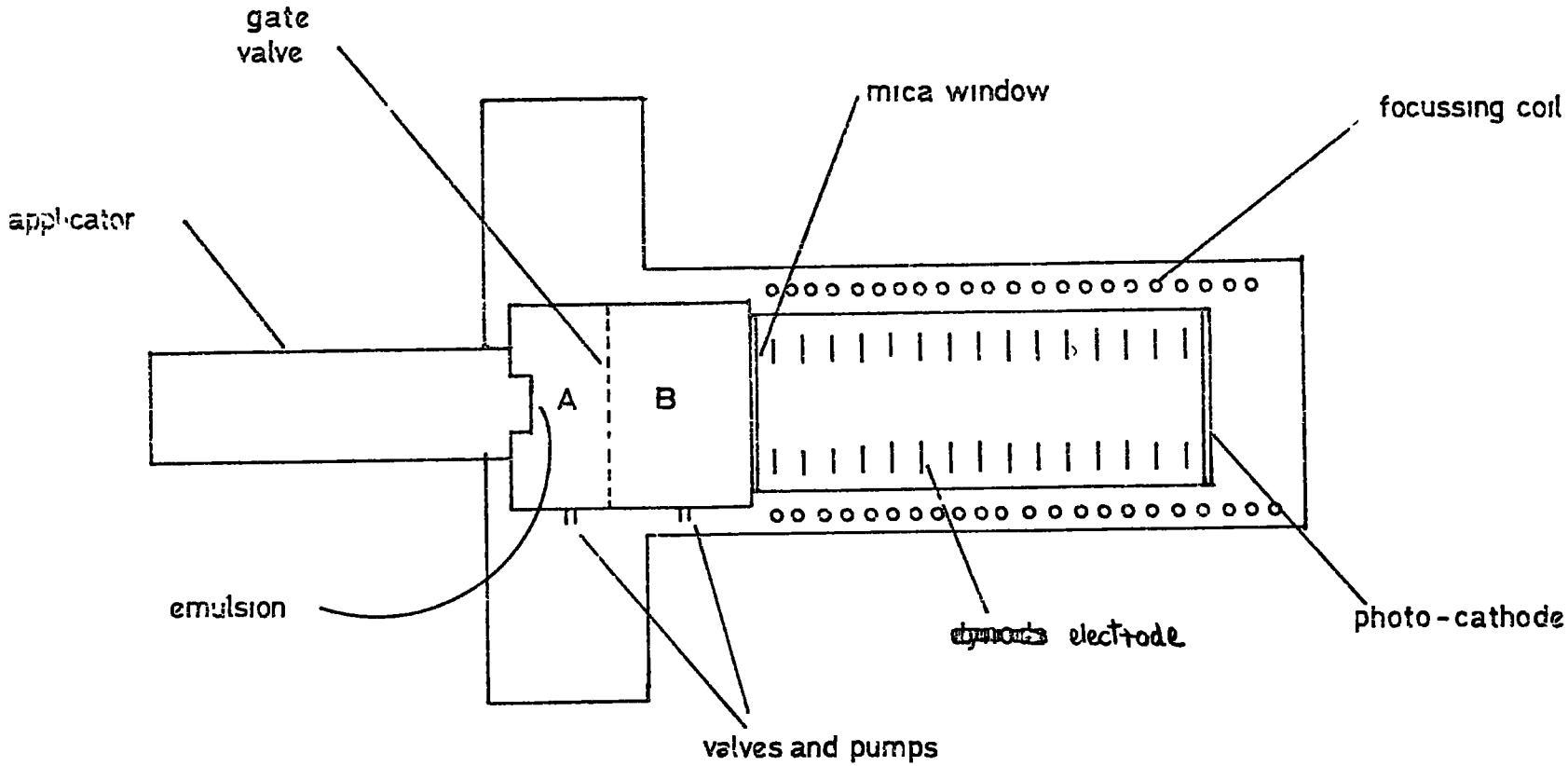

FIG 26 DIAGRAM SHOWING THE PRINCIPLE OF THE ELECTRONOGRAPHIC CAMERA

attain the above efficiency, even after presensitisation. This is of prime importance when faint astronomical objects, and hence long exposure times are involved.

As all the electrons incident on the emulsion are of the same high energy ($\sim$ 40 keV), each electron causes the same amount of development along its track. Also, the grain size is much smaller than with photographic plates, and therefore saturation occurs at a much greater density The net effect, is that with the electronographic camera, the density on the plate is proportional to the intensity of the incident radiation, and this linearity law is exhibited over a dynamic range of at least 5 in density.

Ilford L4, a fine grain emulsion, was used for the present series of observations

CHAPTER 3

POLARIMETER ALIGNMENT, AND MAKING THE OBSERVATIONS

3.1 Introduction

The polarimeter was initially aligned in the laboratory, before installation on the telescope. Further alignment checks were made at the observing site In the laboratory the optical components were mounted in turn, into the polarimeter, checking at each stage, that their centres were on the principal axis of the polarimeter, and their respective angular orientations were correct.

3.2 Defining the Principal Axis

This was simply achieved by attaching crosswires to the two end apertures of the polarimeter, and aligning a laser beam to cut the intersections at both ends. The spot of light caused by the pencil beam was used to centre each of the components as they were mounted.

3.3 The Half Wave Plate

It is extremely important that the half wave plate is inserted into its housing, with the optic axis vertical with respect to the vertical as defined by the grids, when the adjusting knob is set at the zero degrees position Any deviation from this correct alignment will cause a systematic error in the position angle measurement of the polarisation.

The alignment was achieved by mounting accurately calibrated polaroids at each side of the plate, and viewing an intense blue light source through the three components. If one polaroid is vertical, and the second one horizontal, extinction of the light will occur providing the half wave plate does not rotate the plane of polarisation.

Extinction of the light therefore ensures that the optic axis of the half wave plate is in the required vertical direction.

3.4 The Wollaston Prism

The prism was inserted into its rotateable housing, which then required locking at the required orientation so that the deviation between the O and E rays was in the horizontal plane.

The remainder of the components were inserted into their respective positions, and, with the polarimeter now in operational mode, the 'photo-cathode' image of the grids was viewed by mounting a simple eye-piece on the camera-end of the polarimeter. The image seen, is illustrated in figure 3.1a and is just the simple double image of the grid gaps formed by the Wollaston prism. The horizontal lines across the picture are the images of the 20 micron gold wires stretched horizontally across the grids, and described in section 2.3.4.

If the deviation of the prism is not in the horizontal plane, the two orthogonally polarised images of each section of the wire, are vertically displaced and appear as illustrated in figure 3.1a(i). The prism is slowly rotated, until the images of the grid wires have the correct appearance (figure 3 1a(ii)), when the deviation is confined to the horizontal plane.

3 5 Adjustments made on the Telescope

3.5.1 Introduction

Although alignment of the individual components is carried out in laboratory conditions for accuracy, final focussing and setting up procedures have to be done with the polarimeter and camera mounted on

the telescope.

3.5.2. Aligning the Grids

Although not absolutely necessary, it is convenient to rotate the polarimeter on the telescope, until the grid bars run in a North-South direction. This is achieved by imaging a star on the edge of a grid spacing, using the grid viewing mirror and eyepiece. If the telescope is now driven in declination, the star will be seen to move up and down the grids, while remaining exactly on the edge of the grid, if the alignment is correct. The two cases of misalignment and North-South alignment are shown in figures 3.1b.

3.5.3. Focussing the Polarimeter

The Polarimeter is focussed, by moving the relay lens, until the grids are imaged on the photocathode of the electronogrphic camera. The 20 micron gold wires attached to the grids, are used for this purpose, as accurate focussing is necessary before their images can be seen on the electronographs.

A series of test exposures with the grids uniformly illuminated are taken, with the relay lens at several different positions, and the results are interpolated by eye, to find the position of best focus.

3.5.4. Focussing the Telescope

The telescope is focussed, so that the grids lie in the focal plane of the secondary mirror, by means of a knife edge test, which is shown diagrammatically in figure 3.1c. A star is driven onto the edge of a grid, and is viewed using the 45° grid viewing telescope with no eyepiece, so that the light is not brought to focus. If the main telescope is

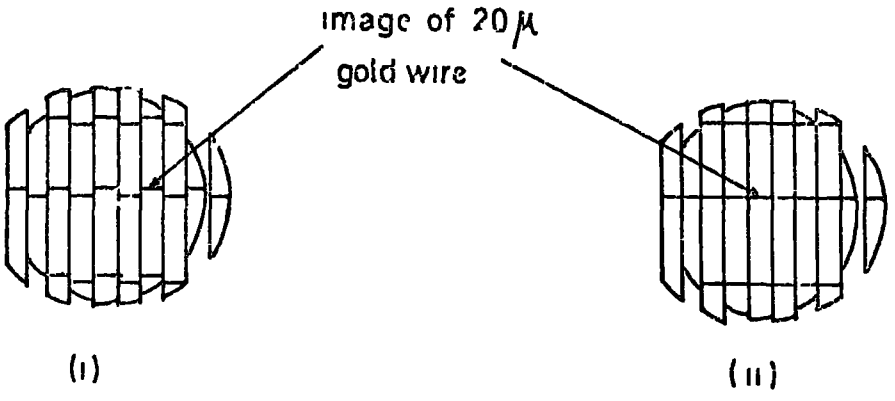

FIG 31a ALIGNING THE WOLLASTON PRISM HORIZONTALLY

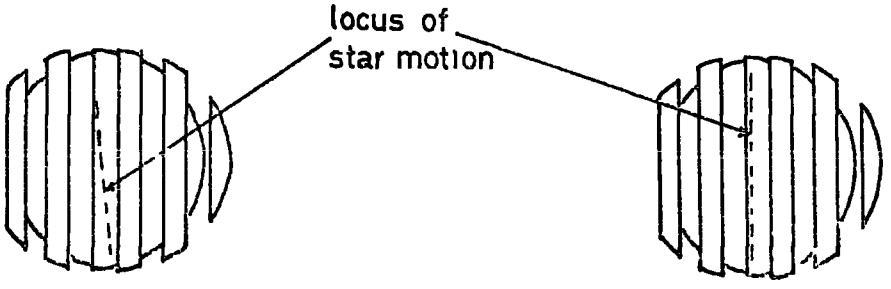

FIG 31b ALIGNING THE GRIDS NORTH-SOUTH

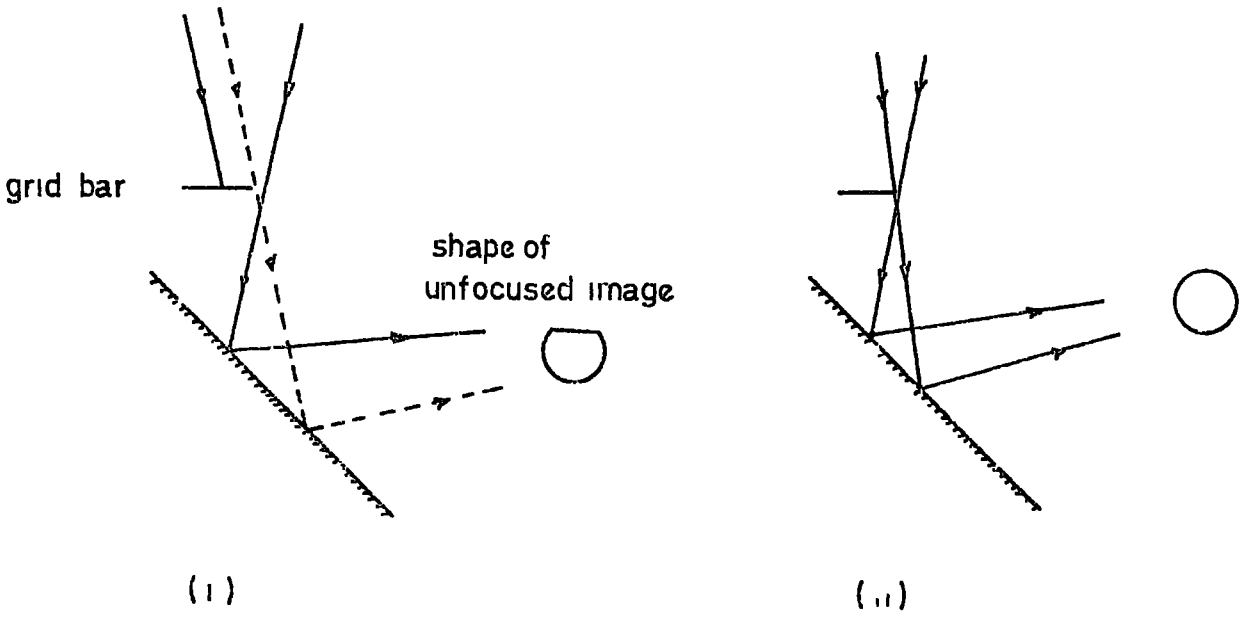

FIG 31c FOCUSSING THE TELESCOPE

focussed (figure 3.1c(ii)), the star image acts as a point source, and a uniform diffuse circle of light is seen in the grid viewing telescope. If the main telescope is not focussed (figure 3 1c(i)), part of the initial star image is obstructed by the grids, and the resulting image in the grid viewing mirror has a dark area corresponding to the obstructed light.

Focussing is simply achieved by slowly moving the telescope secondary.

3.6 The Series of Observations

3.6.1. Introduction

With the polarimeter adjusted in the manner described, a series of exposures are taken of the object to be observed, (in this case M82), so that after reduction, the polarisation of the light incident from each part of the object, will be completely specified

3.6.2. Preliminaries before each Series of Observations

The object is centered in the grid field using the grid viewing mirror, and then the off axis guider eyepiece is traversed across the field of view provided by the 45 degree mirror, until a suitably bright star is positioned on the illuminated cross wires For the duration of the observations on a particular object, the telescope is manually guided on this star, to ensure that the telescope image does not wander on the grid field. The camera therefore records information from each point of the object at exactly the same place on the photo-cathode, for as many exposures as are required so that errors produced by variations in the photo-cathode sensitivity are therefore minimised.

3.6.3. A Sequence of Exposures

With the polarimeter adjusted as described, four exposures are taken at half wave plate orientations of 0, 22½, 45 and 67½ degrees respectively. These four electronographs contain all the information necessary, to uniquely determine the polarisation magnitude and direction for each element of the image.

Half the galaxy is obscured behind the grid bars during the first four exposures, and the hidden half of the galaxy is brought into view by moving the grid system exactly one grid width horizontally. If the first 'half' of the galaxy was taken at the 'grid in' position, the grids are automatically moved the correct distance, set by the stop, to the 'grid out' position, for the remaining exposures.

A further series of four exposures, at half wave plate orientations of 0, 22½, 45, 67½ degrees, is then taken, to provide a polarisation map of the second 'half' of the galaxy Electronographs 1 and 5 of M82 taken at the 1 m telescope of the Wise Observatory, Israel, are shown in plate 7.

(5)

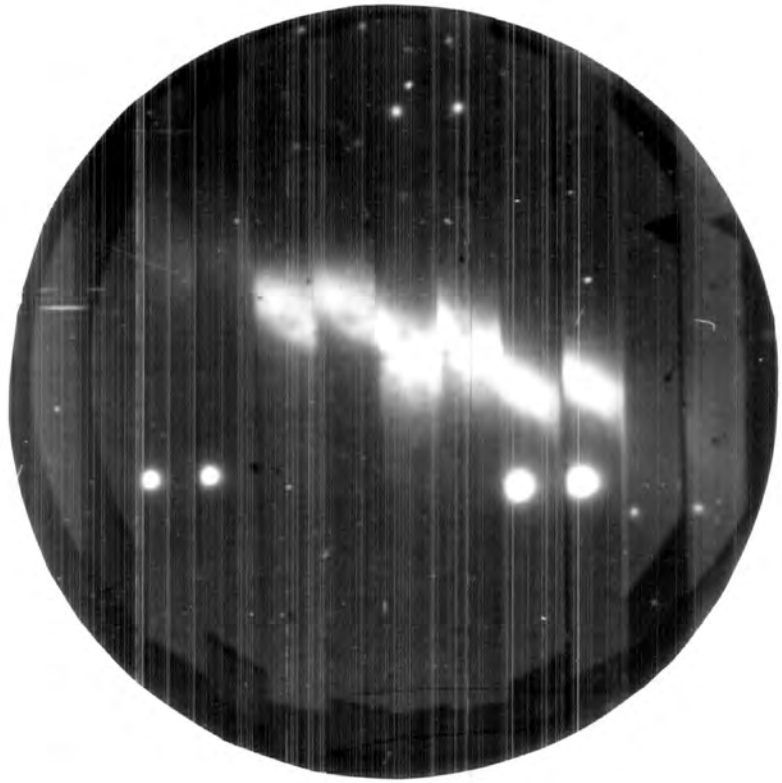

(1)

PLATE 7

CHAPTER 4

APPLICATION OF THE BASIC THEORY TO THE DURHAM POLARIMETER

4.1 Introduction

The measurements made with the astronomical polarimeter are simply related to the basic method described in section 1.3. If a light ray is traced through the analysing components of the polarimeter, for the various half wave plate orientations, a set of equations similar to those of section 1.3 can be derived, which connect the polarisation parameters of the incident ray, and the recorded intensities. Any small element of the image formed in the focal plane of the telescope, can be regarded as a point source or pencil beam of light, and the transmitted intensities for various half wave plate orientations, can be reduced to give the polarisation parameters of the integrated light forming that small element of the image The transmitted intensity is of course recorded, as the density of the image of the same small element on the electronographic plate.

The transmission of a partially plane polarised pencil beam of light, (corresponding to an elemental area of the image), is shown in figure 4 1, for the four different orientations of the half wave plate. Expressions for the transmitted intensities (I_1 - I_8) in terms of the polarisation parameters of the incident beam, are shown for each of the four exposures taken.

4.2 Electronographs 1 and 2

Electronograph 1 is taken with the half wave plate optic axis vertical (i.e 0^o), which results in the plane of polarisation of the plane polarised component of the incident radiation being reflected about the vertical

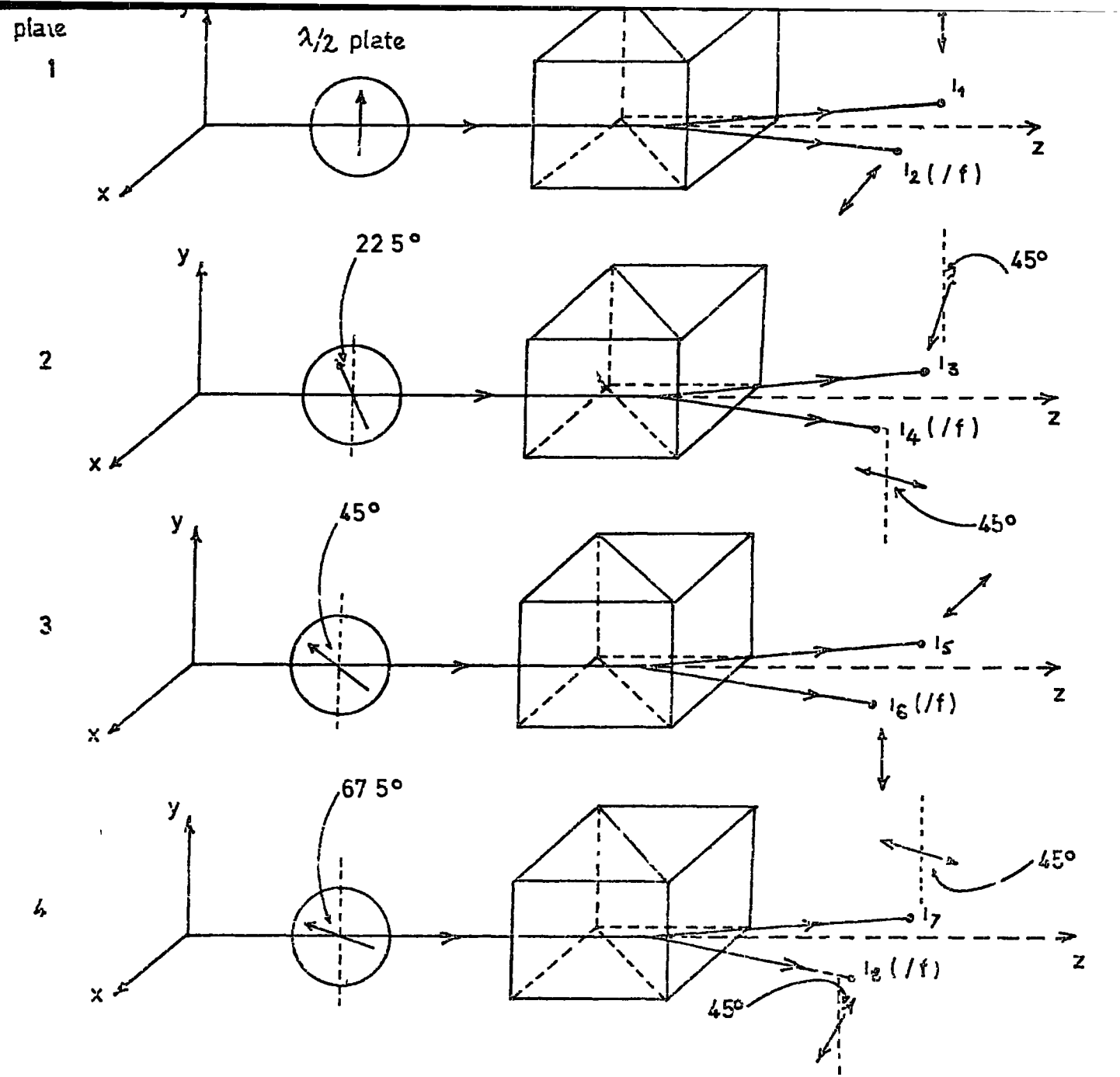

$$I_1 = \frac{I - I_p}{2} + I_p \cos^2\theta$$

$$\frac{I_2}{f} = \frac{I - I_p}{2} + I_p \sin^2\theta$$

$$I_3\, e_1 = \frac{I - I_p}{2} + I_p \cos^2(45-\theta)$$

$$\frac{I_4\, e_1}{f} = \frac{I - I_p}{2} + I_p \sin^2(45-\theta)$$

$$I_5\, e_2 = \frac{I - I_p}{2} + I_p \cos^2(90-\theta)$$

$$\frac{I_6\, e_2}{f} = \frac{I - I_p}{2} + I_p \sin^2(90-\theta)$$

$$I_7\, e_3 = \frac{I - I_p}{2} + I_p \cos^2(135-\theta)$$

$$\frac{I_8\, e_3}{f} = \frac{I - I_p}{2} + I_p \sin^2(135-\theta)$$

FIG 41 REDUCTION EQUATIONS FOR THE DURHAM POLARIMETER

after transmission. The Wollaston prism then separates the light into horizontally and vertically polarised components, which are deviated in the horizontal plane, and brought to their separate foci on the photo-cathode of the electron camera. The intensities of the two beams incident at points A and B on the photo-cathode are recorded by the density of the images they produce (i_1, i_2).

It is important to remember, however, that point B on the photo-cathode may have a slightly different photoelectric sensitivity than point A. and therefore. the measured density 'i_2', must be corrected by a relative sensitivity factor 'f', between points A and B before a direct comparison can be made. This sensitivity or 'f' factor, is included in equations 1 and 2, which relate the measured densities (i_1, i_2), to the polarisation parameters to be determined. 'f' also eliminates the sensitivity of the photo-cathode to plane polarised light.

Electronograph 2 is taken with the half wave plate rotated to an angle of $22\frac{1}{2}$ degrees with the vertical, which results in the plane of polarisation making an angle of (45 - θ) degrees, after transmission. The Wollaston prism, which remains fixed for the whole series of exposures, splits the light into vertically and horizontally polarised components as before, which are then incident on exactly the same points of the photocathode (A and B), as for electronograph 1.

The effect of rotating the plane of polarisation of the light by 45 degrees, and keeping the analyser fixed, is exactly the same as simply rotating the analyser to 45 degrees in the simple method described in section 1.3. The transmitted beams for electronograph 2, are therefore the intensities of the incident light polarised at ± 45 degrees to

the vertical, and are completely analogous to the intensities 'i_3' and 'i_4' described in section 1.3. The intensity at B, 'i_4', must be corrected by the same 'f' factor before comparison with 'i_3', and both values must be modified by an exposure factor 'e_1', before comparison with the intensities from plate 1. The exposure factor 'e_1' describes the ratio of the exposure times between electronographs 1 and 2.

After correction, plate 2 yields a further pair of equations, connecting the polarisation parameters with the measured densities. These four equations are similar to the basic equations of section 1.3, except for the inclusion of the quantities 'f', and 'e_1', which need to be determined, before the same reduction procedure can be used to find the Stokes parameters of the incident light.

The exposure factor 'e_1' is simply the ratio of the total amount of light received on electronograph 1 to electronograph 2 and is given by,

$$e_1 = \frac{i_1 + i_2/f}{i_3 + i_4/f} \qquad 4.1$$

It is only necessary therefore to determine the 'f' factor between points A and B, before the required reduction can be carried out.

4.3 Electronographs 3 and 4

To facilitate the measure of 'f', a further two electronographs are taken with half wave plate orientations of 45 and 67½ degrees. The plane polarised component of the radiation, therefore makes angles of (90 - θ), and (135 - θ), with the vertical, respectively, after transmission through the plate

A further set of four equations are obtained, linking the measured density to the incident polarisation, with the inclusion of only 2 new unknowns, the exposure factors 'e_2' and 'e_3', needed to normalise the intensities to electronograph 1 The equations 1 - 8 in the figure can now be mathematically solved to give 'f', 'e_1', 'e_2', 'e_3' and hence the required polarisation parameters 'p' and 'θ'. It is instructive however to look at the information on the electronographs in turn, and find the 'f' factor on a simple logical basis, and then reduce the equations by comparing the intensities with those derived from the simple method described in section 1.3.

Comparison of electronographs 1 and 3, shows that the plane of polarisation of the incident light has been rotated through 90 degrees in electronograph 3 compared to electronograph 1, for transmission through the half wave plate The vertical component of the radiation selected by the Wollaston prism for electronograph 3, is therefore exactly the same as the horizontal component selected in electronograph 1. The only difference between the two beams, is that in electronograph 1 the intensity is recorded at point B while in electronograph 3 it is recorded at point A. Similarly the horizontal component of electronograph 3 is the same as the vertical component of electronograph 1 except for the difference in sensitivity factor between points A and B. Including the relative exposure factors needed to compare electronographs 1 and 3, two equations connecting the intensities (i_1, i_2, i_5, i_6) can be written,

$$i_1 = \frac{i_6}{f} \cdot e_2 \qquad 4.2$$

$$i_{2/f} = i_5 \quad e_2 \qquad 4.3$$

which can be solved to give the required estimate of 'f', i.e.

$$f_1 = \sqrt{\frac{I_6 \cdot I_2}{I_5 \cdot I_1}} \qquad 4.4$$

Electronographs 2 and 4 also have a rotation difference of 90 degrees, which means that the locations on the photocathode where the ± 45 degree intensities are recorded are also interchanged. The intensities from electronographs 2 and 4 can also be used therefore to obtain a second independent estimate of the same 'f' factor, i.e.

$$I_3 = \frac{I_8}{f} \cdot e_3 \qquad 4.5$$

$$\frac{I_4}{f} = I_7 \cdot e_3 \qquad 4.6$$

$$f_2 = \sqrt{\frac{I_8 I_4}{I_7 I_3}} \qquad 4.7$$

The mean value of the sensitivity factor 'f' is therefore taken to be,

$$f = (f_1 + f_2)\ /2, \qquad 4.8$$

and the agreement between the two estimates, is a measure of the uncertainties associated with the technique.

With the 'f', and hence 'e' factors determined, the initially measured densities can be normalised (for example I_4 becomes $I_{4/f} \cdot e_2$), and the basic equations derived in section 1.3 used to obtain an estimate of the Stokes parameters of the incident light, i.e

$$Q_1 = I_1 - I_{2/f} = Ip \cos 2\theta \qquad 4.9$$

$$U_1 = (I_3 - I_{4/f}) \quad e_1 = Ip \sin 2\theta \qquad 4.10$$

$$I_1 = I_1 + I_{2/f} \qquad 4.11$$

The intensities (i_6, i_5, i_8, i_7) from electronographs 3 and 4, which were originally taken to find the sensitivity factor, also comprise a set of polarised intensity measurements at (0, 90, ± 45) degrees respective. They can also be substituted into the basic equations to give a second estimate of the Stokes parameters for the incident beam.

$$Q_2 = (i_{6/f} - i_5) \quad e_2 = Ip \cos 2\theta \qquad 4.12$$

$$U_2 = (i_{7/f} - i_3) \cdot e_3 = Ip \sin 2\theta \qquad 4.13$$

$$I_2 = (i_{6/f} + i_5) \cdot e_2 = I_1 \qquad 4.14$$

The two estimates of the Stokes vectors are averaged to obtain the best values, before returning to the practical units of percentage polarisation and preferred direction, via the transformations described in section 1.5.

$$P = \frac{\sqrt{\bar{U}^2 + \bar{Q}^2}}{I} \qquad 4.15$$

$$\theta = 0.5 \arctan\left(\frac{\bar{U}}{\bar{Q}}\right) \qquad 4.16$$

4.4 Discussion of the Technique

The four electronographs, in a series of observations, contain eight images of one half of the object. The relative densities of a particular area, on each of the eight images, determine the polarisation parameters (I, Ip, θ) of the incident light. It is of paramount importance therefore, that exactly the same element is located on each of the images, before the density is determined.

If we require to measure the polarisation over an area of ~ 5 x 5 arc seconds, it is necessary to locate precisely, an element of area

$\sim$ 100 μ^2 on each of the 1 cm^2 images. This must then be repeated for several thousand different locations on the electronographs, so that a matrix of points on the image of the galaxy is obtained, where the magnitude and direction of the polarisation is known for each element. To meet the above criteria of accurate alignment, and repetition for many points, a sophisticated computer reduction procedure is probably the only satisfactory method.

CHAPTER 5

THE COMPUTER REDUCTION TECHNIQUE: I

5.1 Introduction

The technique was developed on the two sets of 4 electronographs of M82 (described in section 3.6), necessary to produce a complete polarisation map of the galaxy. Although electronographs of several interesting objects were taken during the trial run with the mark II polarimeter in March 1975, M82 was chosen for the initial reduction, because previous photo-electric measurements (Visvanathan and Sandage 1969, 1972 and Elvius 1963, 1969) had already revealed a large amount of polarisation, and a regular orientation of E vector The validity of the first map to be produced by our new technique could therefore be readily checked by comparison with previous work

The reduction procedure is summarised in the flow chart shown in figure 5.1.

5.2 Digitisation

5.2 1. The P.D S Procedure

The information on the electronographic plates has first to be converted to a digital form, before it can be processed in a computer This means dividing the electronograph into a huge matrix of elements, and storing the density for each point of the matrix. The 'visual' plate is therefore replaced by a large number of representative densities stored on magnetic tape.

The electronographs were digitised on the P.D.S. machine at the Royal Greenwich Observatory, and the digital output was stored on 7 track unlabelled tapes.

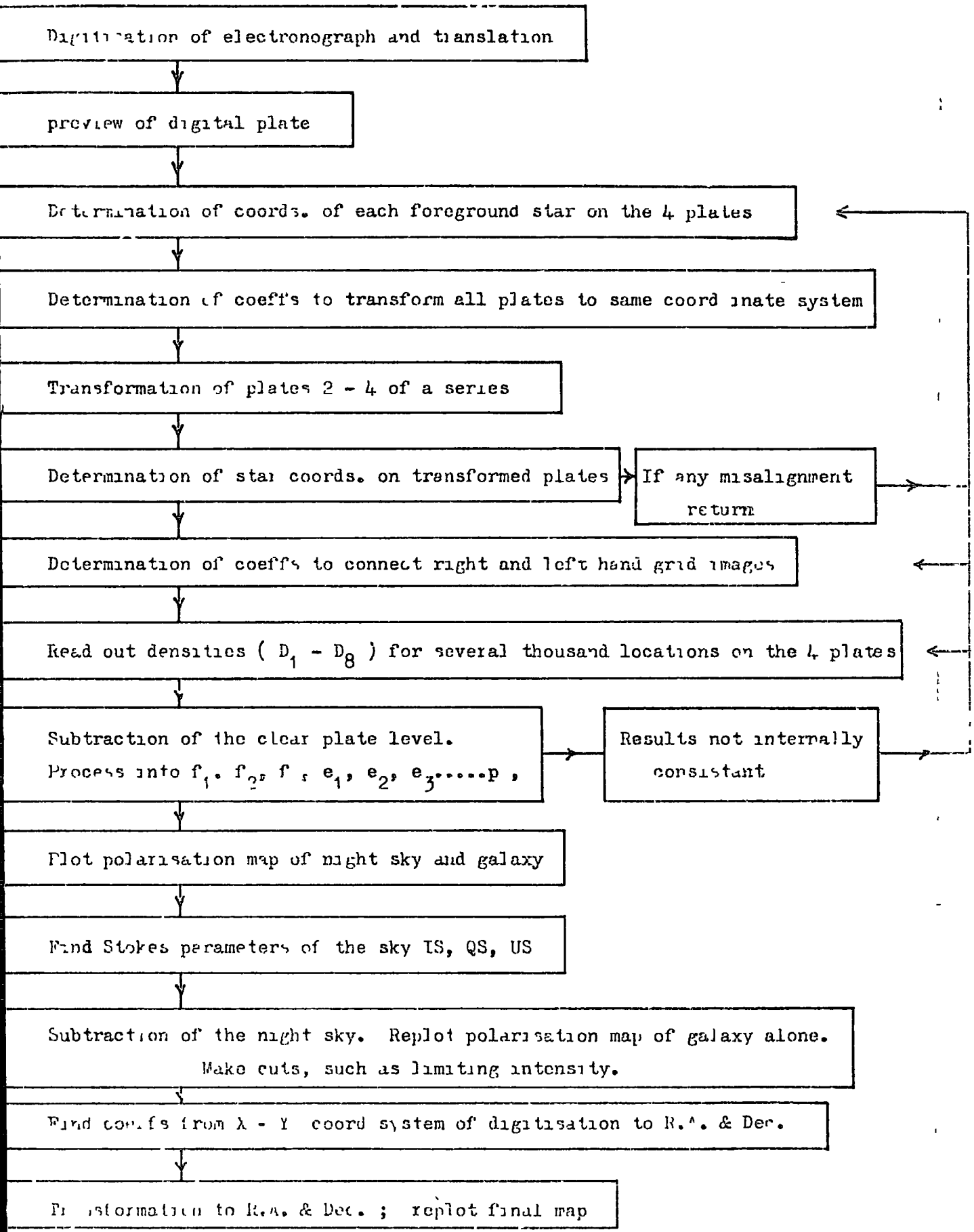

FIG 51 FLOW DIAGRAM OF THE REDUCTION TECHNIQUE

The machine was adjusted to scan an area slightly larger than the image of the grids on the electronograph, (see figure 5 2), so that the density corresponding to an area outside the region illuminated by the polarimeter could be determined This residual density, which is the sum of the emulsion noise, shot noise from the electron camera, and the fluctuations in the zero level introduced by the P D.S. machine itself, must be subtracted from every location on the electronograph to obtain the true density.

The digitisation procedure is diagrammatically shown in figure 5.2. An aperture corresponding to 24 microns squared on the electronograph was selected The machine therefore travelled along in the X direction, continuously monitoring the density of the 24 micron squared area directly beneath the aperture At time intervals corresponding to a 26 micron translation of the aperture, the density was recorded on the magnetic tape At the end of each scan in X, the machine automatically steps 26 microns in Y, before rescanning back to the origin in the X direction A total of 512 scans were made on each electronograph, each scan depositing 512 densities on to the magnetic tape, resulting in the electronograph being digitised into approximately a quarter of a million pixels of information.

Each electronograph was placed on the P.D.S. machine so that the Y scan axis accurately corresponded to a North/South direction. This was achieved by ensuring that when the aperture was hand traversed in 'Y', the spot of light followed the edge of a set of grid images. The electronographs of a particular set were all accurately placed in the same position on the scanning table by using the edges of the image of the grids as reference points This minimises the errors at a later

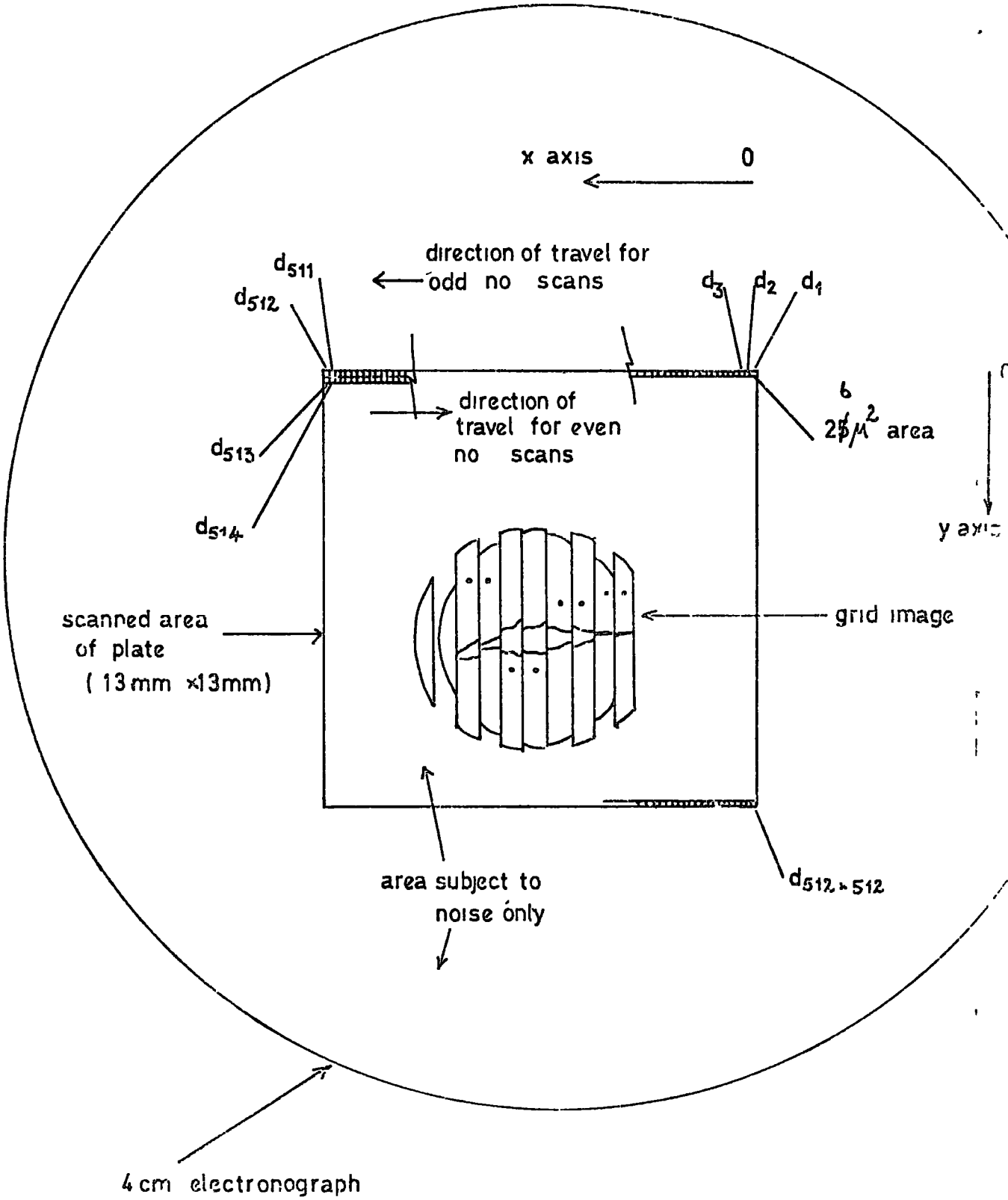

FIG 5.2 THE DIGITISATION PROCEDURE

stage, when the digital electronographs have to be aligned extremely accurately inside the computer, to ensure that the densities (i_1 - i_8) are taken from exactly the same area of the multiple polarised images.

The density, (which is proportional to the intensity of the incident light because of the linearity property of the electron camera), was recorded as an integer number between 1 and 1024. The two limits correspond roughly to densities of zero and 5 on the electronograph respectively For the M82 electronographs, the highest number recorded for the brightest parts of the disk were approximately 500.

5 2.2. Translation of the Tapes and Disk Storage

It is only possible to write the densities onto 7 track magnetic tape with the P.D.S. machine, and the system on which the tapes were to be read and analysed, only had a 9 track tape read facility. It was first necessary therefore to send the tapes to the Cambridge Computing Laboratory, where they could be translated from 7 to 9 track, before being forwarded to the Northumbrian Universities Multiple Access Computer at Newcastle

When the tapes were finally read from Durham, the data was transferred from tape to disk storage, which provides easier accessibility for the user At the same time, the data sets of 512 elements, corresponding to even numbered scans, were turned round, to undo the effect of the raster scanning

5 3 Primary Inspection of the Digital Data

5.3.1 Introduction

Whenever an operation was to be carried out on a particular data file, it was first read from storage in sequential disk files, where the quarter of a million numbers were stored one after the other. The

densities were read into a 512 by 512 matrix so that any element could be accessed immediately, and operated on.

Before starting any lengthy reduction on a series of electronographs, it is first important to check that the digitisation has been carried out correctly, and the data forms a true representation of the density on the electronographs. Any imperfections in the digitised data, for example the P.D.S. machine not working absolutely correctly, can then be taken into account, before 'blindly' proceeding with the mass reduction of numerical data.

5.3.2. Visual Display of a Digital Electronograph

To be able to see what the digital information actually looked like, the 512 x 512 pixels were compressed so that a new array of 128 x 128 points were formed, where each new density value corresponded to the average of 16 original digitisation values. This size of array is much more manageable to view as line printer output.

Figures 5.3 and 5.4 show the digital information for electronographs 4 and 2 displayed visually. A form of contour map is produced by dividing the total density range (0 - 1000) into 20 bins, and replacing the actual numerical density of a point, by a symbol for that particular density bin. The symbols used were blank, • , 1, 2, - - - 9, A, B, - - - J, and have a width of 50 density units each.

Comparison with the actual electronographs in section 3.6 3. shows that all the major features are visible on the contour map, and that the digital data appears to form a true representation of the original electronograph. It is also apparent, looking at the contour levels, that

FIG 53 A CONTOUR MAP OF ELECTRONOGRAPH 4

FIG 5 4 A CONTOUR MAP OF ELECTRONOGRAPH 2

residual density

the ~~noise~~ on the plate has a value between 0 and 50, and the combined noise and night sky signal is between 50 and 100. The densest parts of the galaxy are approximately 600, while the brightest foreground stars are actually out of the density range (0 - 1024) of the P.D.S. machine.

5.3.3 Investigation of the Noise Density

The residual density due to noise on the electronograph, is an important quantity, as it must be subtracted from the total signal, for each location on the grid image, before the polarisation can be calculated The only method of determining the noise density underneath the image, is by interpolating from the peripheral regions of the electronograph, where the entire signal is attributable to noise.

Figure 5.5 shows a frequency distribution of the pixel densities of electronograph 4, for the 128 x 128 matrix in the lower density range. (The density values shown on the axis of the plot are for the integrated densities of the 16 bins rather than their mean). The histogram shows the expected form, with a narrow peak at a density value of 415 (26 per pixel), corresponding to the noise. Figures 5 6 and 5.7 show scatter plots of the density versus the X and Y co-ordinates of the scan respectively. The density of points is shown by a symbol in a similar way to that described for the contour map In both plots, the large number of points with densities of approximately 415, confirms that the noise is constant over the plate, and has no variation with either the X

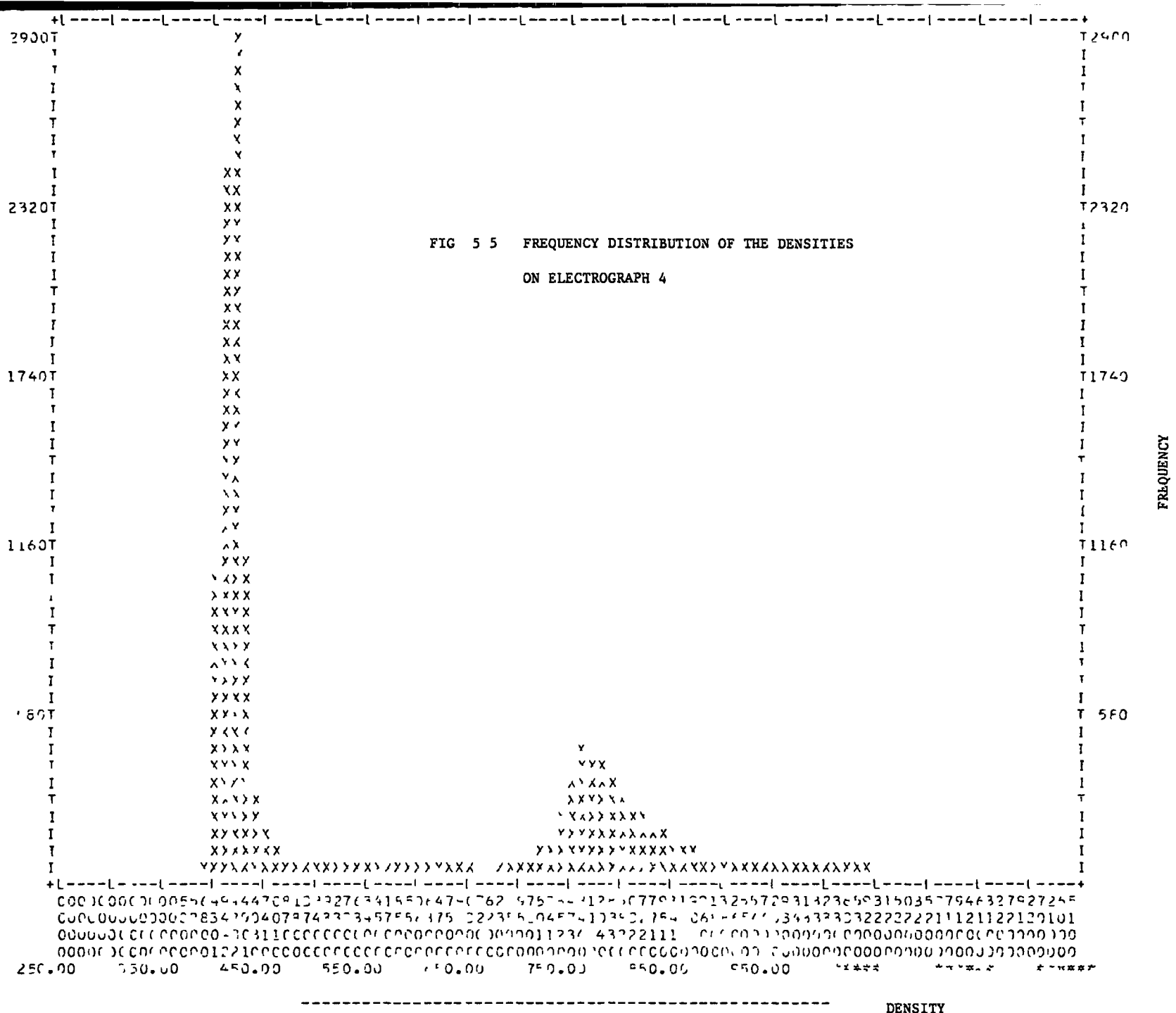

FIG 5 5 FREQUENCY DISTRIBUTION OF THE DENSITIES

ON ELECTROGRAPH 4

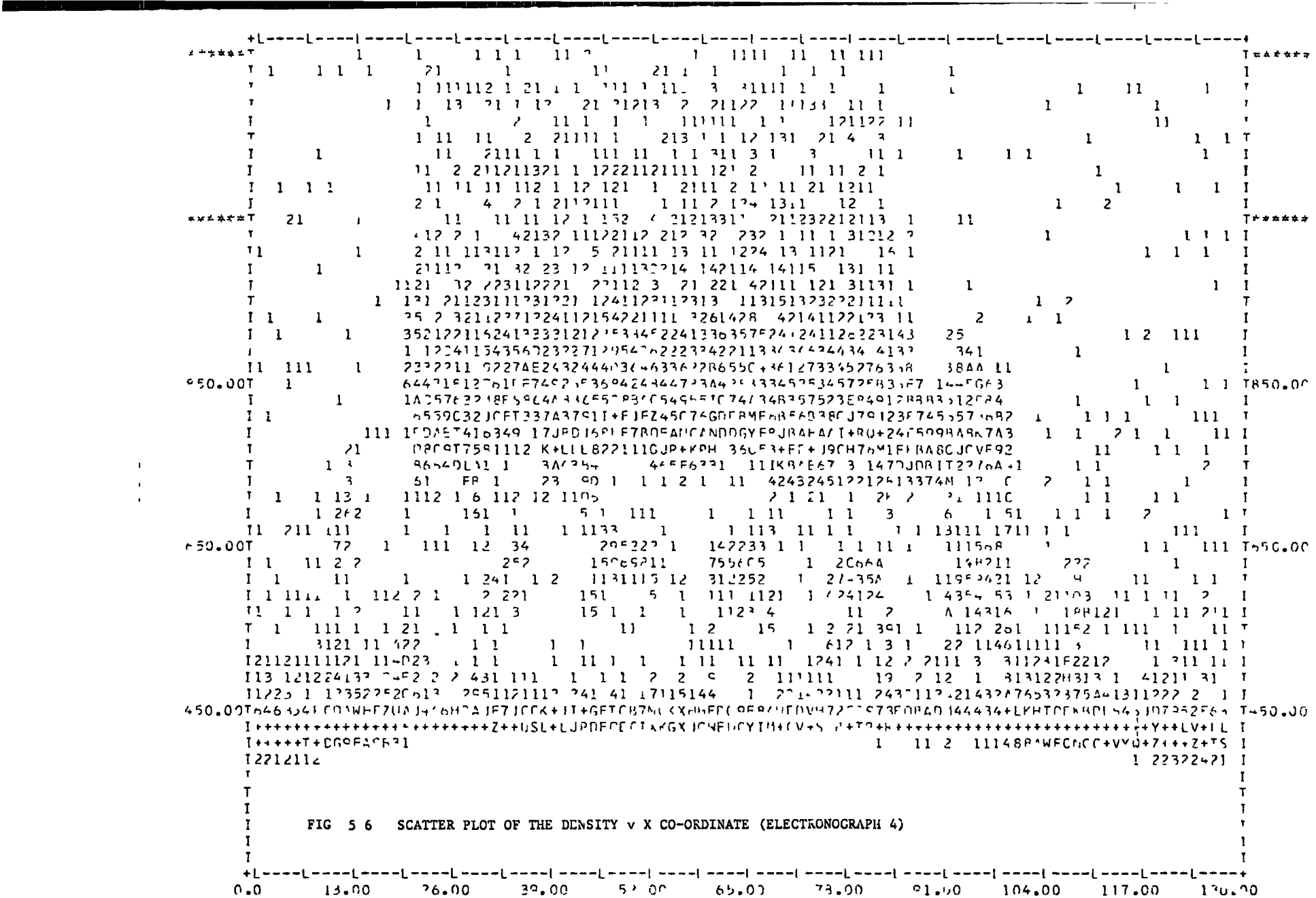

FIG 5 6 SCATTER PLOT OF THE DENSITY v X CO-ORDINATE (ELECTRONOGRAPH 4)

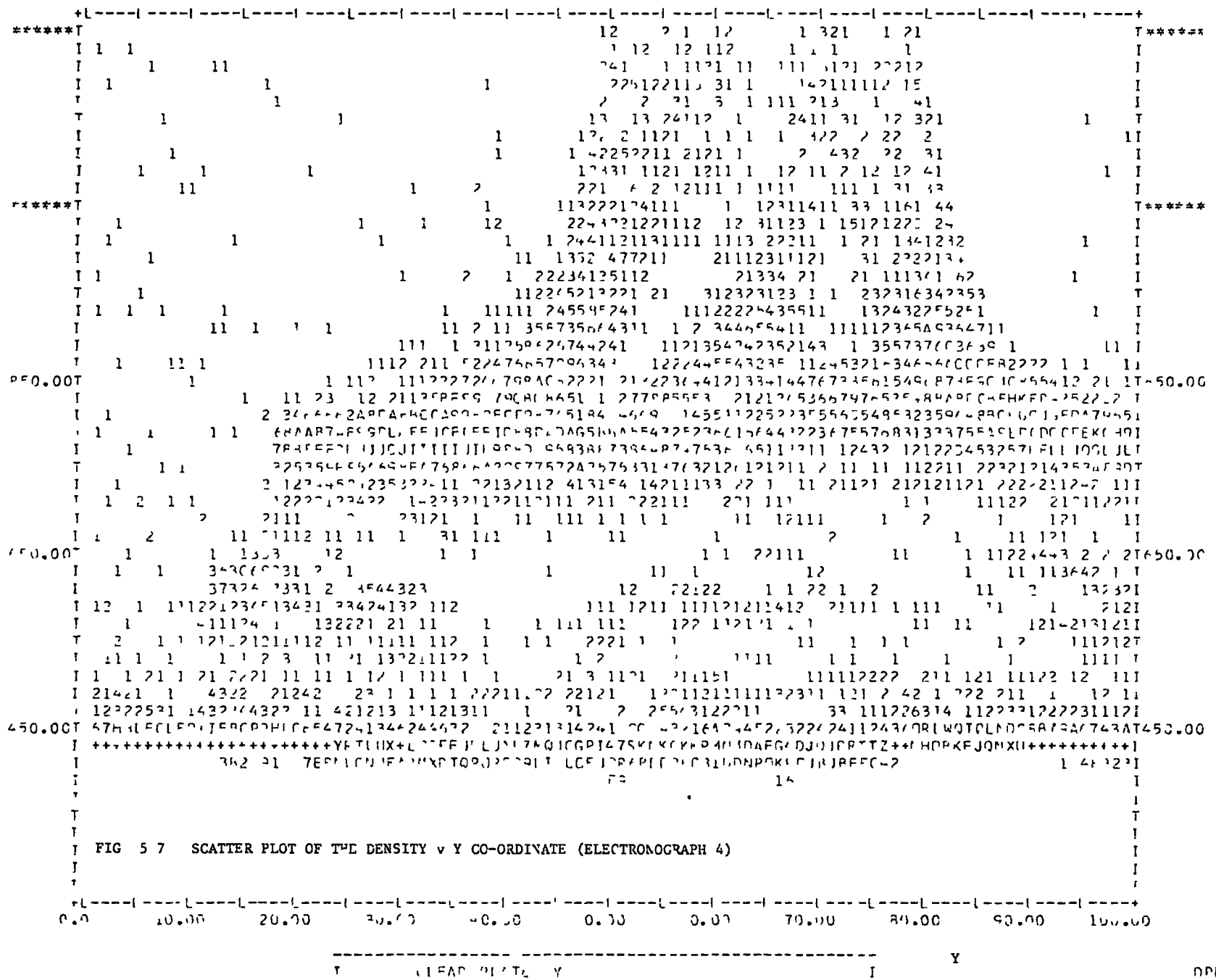

FIG 5 7 SCATTER PLOT OF THE DENSITY v Y CO-ORDINATE (ELECTRONOGRAPH 4)

or Y axis of the scanning direction. The second smaller peak which shows up in figure 5.7 is due to the relatively large number of pixels which have a density corresponding to the noise + night sky value. As expected, this second peak also shows up as a dense region in the scatter plots, but exhibits no variation with the scanning axes.

For electronograph 4, the subtraction of a constant noise level (equal to 26 per pixel), for the entire plate, should be a satisfactory method of extracting the real signal, representative of the incident light polarisation, from the total density.

Figures 5 8, 5 9 and 5.10 show the same plots for electronograph 2 in a series of observations. It is immediately obvious that the noise density, is not restricted to a constant value for the whole electronograph. The scatter plots show that the density changes with the Y direction of the scanning axes, but is constant for a particular Y co-ordinate The density versus X co-ordinate has the required constant value which is broadened because of the Y dependence of the density. After close inspection, most of the electronographs (including different objects), were found to have noise levels which were dependent on the Y scan co-ordinate, but the variation was different and apparently fairly random in each case. Redigitising the same electronograph several times, and obtaining a different functional variation each time, showed that the apparent non-uniformity of the noise was not real, but was introduced at the digitisation stage

The variation is caused by instability in the P D.S. machine, possibly caused by the gain of the amplifier changing as the scan proceeds slowly down the electronograph. (The scan time for one electrono-

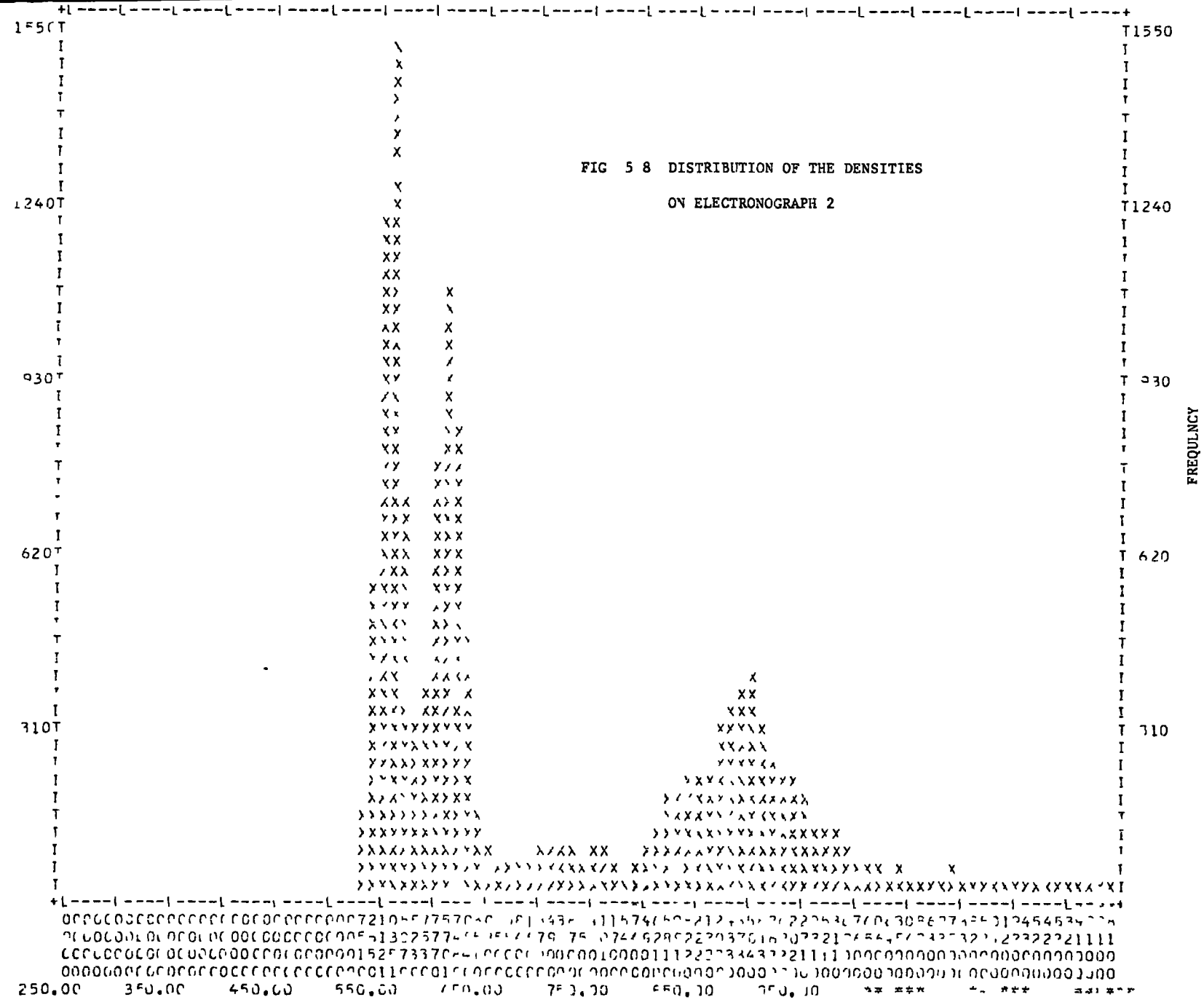

FIG 5 8 DISTRIBUTION OF THE DENSITIES ON ELECTRONOGRAPH 2

PLOT NUMBER 1

FIG 5 9 SCATTER PLOT OF THE DENSITY v X CO-ORDINATE (ELECTRONOGRAPH 2)

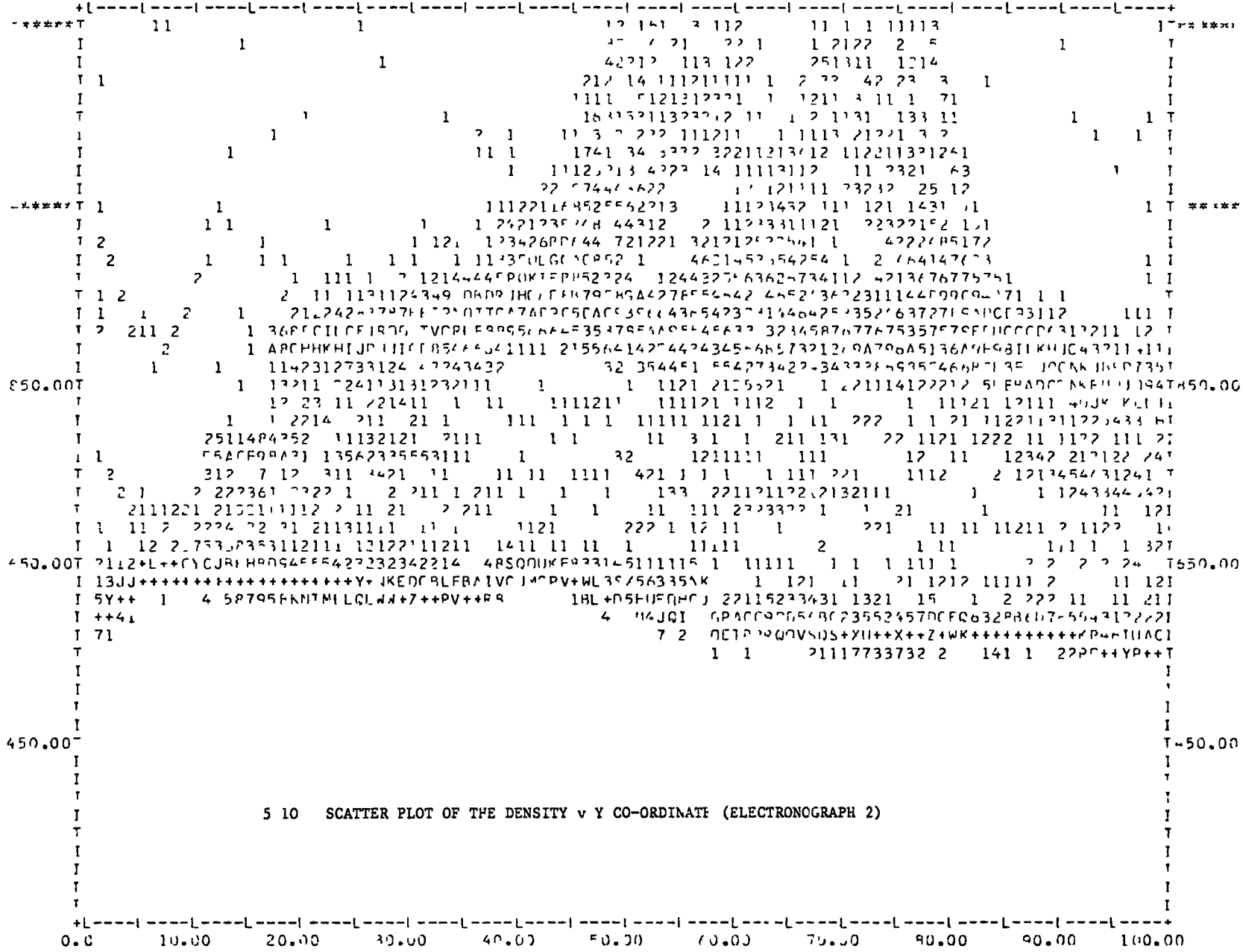

5 10 SCATTER PLOT OF THE DENSITY v Y CO-ORDINATE (ELECTRONOGRAPH 2)

CLEAR PLATE /

INSIDE 11447 OUT LOW 0 OUT HIGH 4937 TOTAL 16384

PLOT NUMBER 1

graph is approximately 30 minutes). The variation is therefore not a function of the X axis, where all the densities are recorded at approximately the same time.

The P.D.S. machine operates by measuring the transmission through the emulsion, and then logarithmically amplifying the signal, to produce a number which is proportional to the density of the element on the electronograph. Because of this logarithmic nature of the amplifier, the change in gain only causes a constant to be added onto the true density, to obtain the one which is actually recorded. The necessary correction to obtain the true density from the recorded one (for any pixel on the electronograph), is therefore additive and not multiplicative. If the noise to be subtracted from the total signal is allowed to vary as a function of the Y co-ordinate on the electronograph, then the remaining night sky + galaxy signal should have the true density value.

The subtraction of the noise component of density on the electronograph is important therefore, not only to determine the density representative of the polarised light signal, but also to correct for malfunction of the P.D.S. machine

5.4 Reducing the Size of the Original Digital Electronographs

Although the 128 x 128 matrices are adequate to produce pictorial representations of the electronographs, and determine their general characteristics, details such as faint stars in the field of view, which are needed for alignment purposes are smeared out, when the 16 individual pixels are integrated. The original 512 x 512 digital plates

have a large amount of 'waste' around the edge of the image, which is only useful initially, to examine the variation of noise signal over the electronograph This waste, if retained as part of the data during the reduction stage, only serves to slow up the procedure because of the large amount of storage needed.

By inspecting the contour map for a particular electronograph (e.g. figures 5.3 and 5.4), it is possible to find the central region of the matrix, which if retained, while the rest is discarded, will contain the image of the grids and a small amount of plate noise on the Y axis of the scan direction. This is all the information that is required to produce the final map.

Each 512 x 512 data matrix was shortened to a matrix of 384 x 384 which required approximately half of the storage space of the former electronograph. The shortened versions were then used to produce contour maps similar to figures 5.3 and 5.4, except that each pixel was allocated a density symbol rather than integrating the 16 bins together. The spatial resolution of these contour maps is therefore 4 times finer than the earlier versions and clearly shows up small details such as faint stars. The 'shortened' versions of the original digitised electronographs (1 - 8) will be referred to as matrices (S1 - S8) in future sections.

5.5 Alignment of the Matrices

5.5 1. Introduction

The individual electronographs are placed on the P.D.S. machine at approximately the same position for each of the digitisations (see section 5 2 1.). This means, that an element of the image, for which

the density is recorded at pixel (I, J) on plate S1, for example, will be recorded at pixel (I', J') for the corresponding element of the image on matrix S2.

Before comparing the densities on the digitised electronographs, to obtain the polarisation parameters, it is therefore necessary, to know how to find the corresponding pixel on matrix S2, S3, S4, for a given one on matrix S1. Similarly, given a pixel in a right hand image strip of a particular matrix, it is necessary to know the location of the corresponding pixel in the left hand image strip.

Once these translations are known, it is then possible to rewrite the matrices describing the second, third and fourth electronograph, so that their elements bear a one to one correspondence with those of matrix S1. The required intensities (i_1 - i_8) can then be read in a straight forward manner, for any XY location on the matrices.

In order to achieve this matrix alignment, it is necessary to have some common fiducial points on all four of the digitised electronographs.

5.5.2. Determination of the Star Co-ordinates

There is no need to have artificial fiducial points formed on the electronographs by the polarimeter, because the foreground stars in the field of view provide natural fiducial marks. If the translation needed to line up the stars from one matrix to the next is found, then it must also align the entire diffuse image. Similarly, the light from each star is split into two orthogonally polarised components by the Wollaston prism, and forms an image in both the right and left hand strips. The translation necessary to go from the right to left hand

image for the stars in the field of view again applies to the diffuse galactic image. If the star centres for all the foreground stars can be accurately located then the necessary translations can be determined.

The star centres were found using a computer program, in which an approximate centre (measured from the contour map), was given as data, and the position of the accurate centre was calculated from the density distribution of the region surrounding the estimated star position.

The procedure is a two stage one, in which the computer first finds the centre in the X dimension, and then uses the same method to calculate the centre in the Y dimension. Figure 5.11 shows the densities of the 25 micron pixels around the point (40, 120) where the initial estimate was chosen. It is immediately obvious on inspection of this part of the matrix, that a star image is located in this region.

To calculate the centre in the X dimension (horizontal axis), the densities in the box which is drawn on the figure, are projected onto the X axis so that the 'histogram' shown in figure 5.12 is obtained. The density shown underneath each bin is the sum of the 10 individual densities which form a column in the box. The plot is in fact a profile of the X projected density for this region of the plate, and clearly shows a slowly varying background component with a gaussian like star profile superimposed

A linear approximation is made to the background component, by taking the histogram values five bins on either side of the density maximum of the distribution, and interpolating under the star image This background value is then subtracted and the resultant plot of the star signal alone

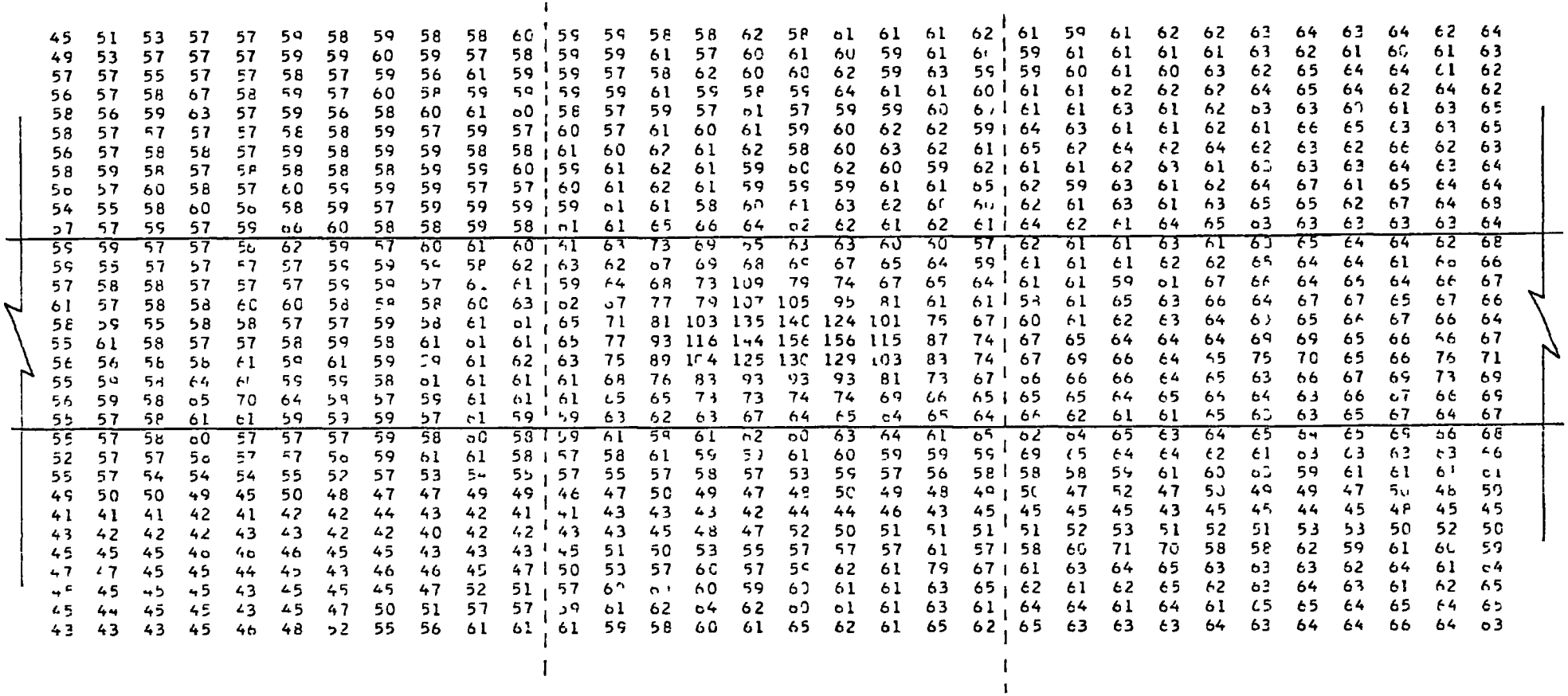

FIG 5 11 DENSITIES IN THE REGION OF A STAR

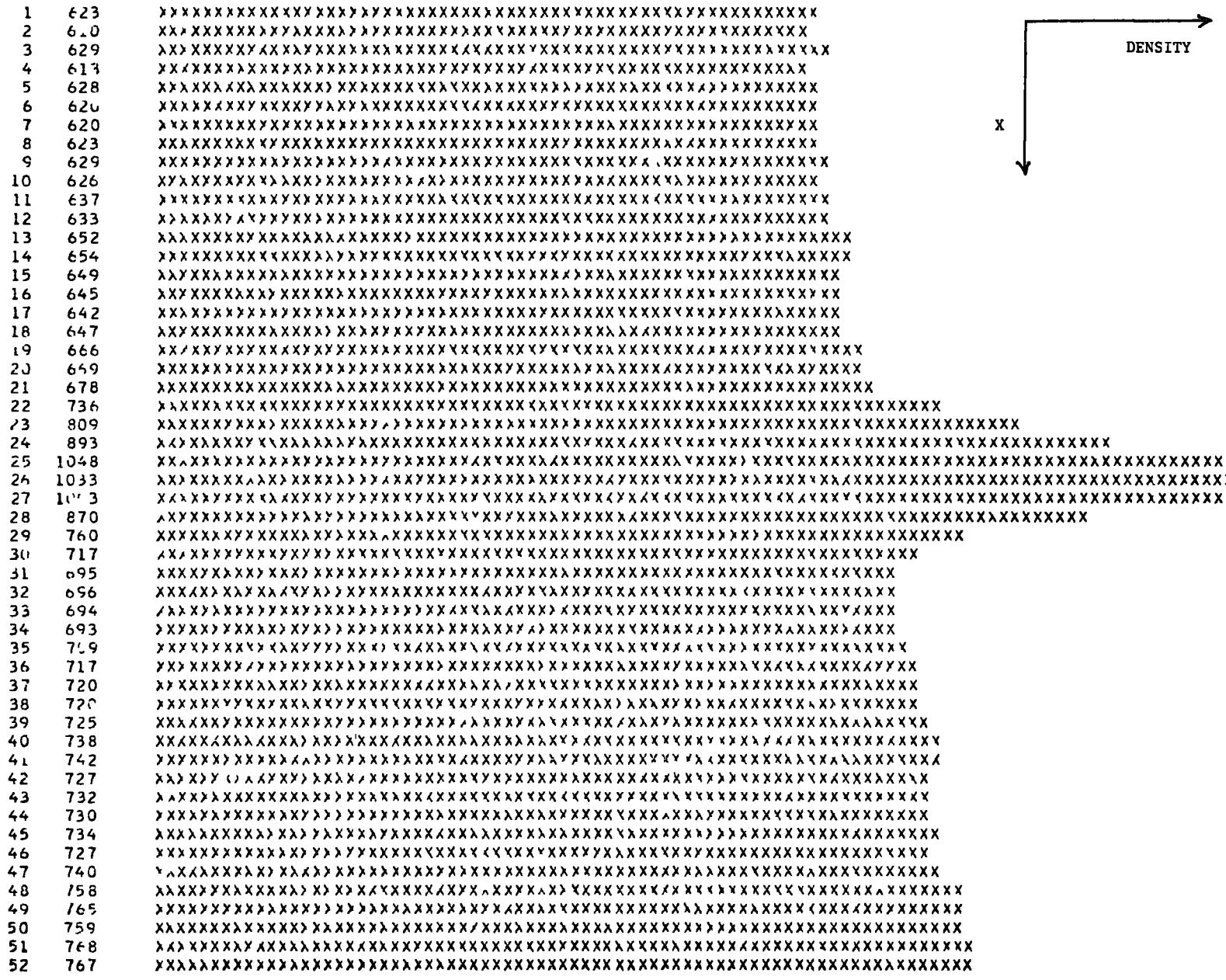

FIG 5 12 THE λ PROJECTED DENSITY NEAR A STAR

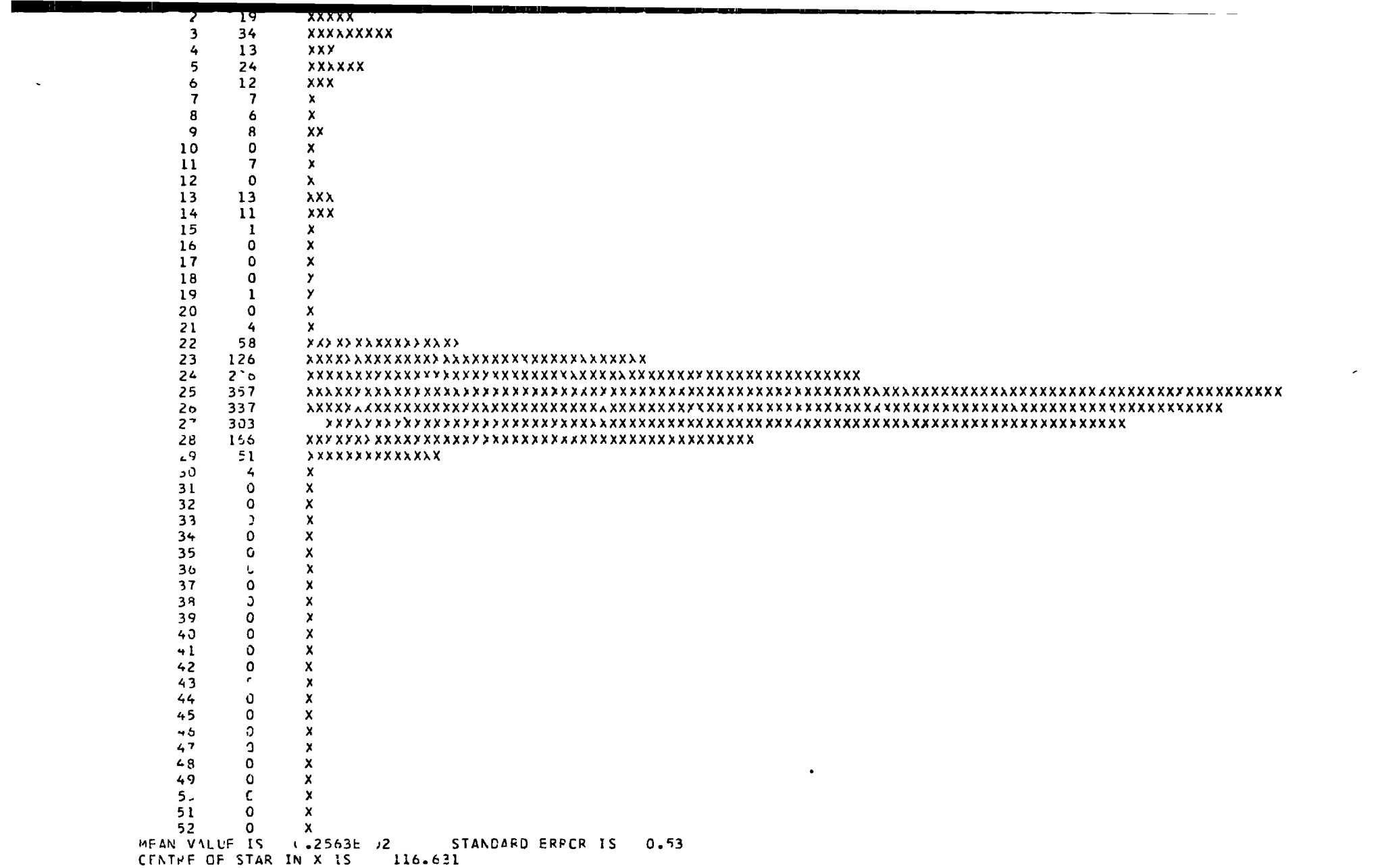

FIG 5 13 THE X PROJECTILD DENSITY AFTER BACKGROUND SUBTRACTION

is shown in figure 5.13. The mean of this density distribution in X, is then taken for the five bins at each side of the mode, and is given by,

$$\bar{X} = \frac{\sum_{X = X_m - 5}^{X = X_m + 5} d_x \cdot X}{\sum_{X = X_m - 5}^{X = X_m + 5} d_x} \qquad 5.1$$

where d_x is the density of the X^{th} projected column

The whole process is then repeated by projecting the densities near the star (shown by the dashed box in figure 5.11), onto the Y axis to ascertain the accurate centre of the density distribution in the Y dimension. The program which is iterative, then takes the accurate co-ordinates as the approximate ones, and repeats the whole procedure to ensure that the best centre has been found The accurate X and Y co-ordinates of the star centre are finally given as output (see figure 5.13).

The program was run on all the star images in the field of view for the two independent sets of matrices S1 - S4, and S5 - S8, describing the two halves of the galaxy, and the results for matrices S1 - S4 are shown in Table 1 As expected, the tables show that the matrices are approximately aligned, but a small translation in both X and Y co-ordinates is required to get from a particular star image on one matrix, to the corresponding star image on another matrix.

5 5 2. Determining the Transformation Coefficients

The co-ordinates of the stars on any two matrices, represent a series

PLATE ⟶ / STAR ↓	S1		S2		S3		S4	
	X	Y	X	Y	X	Y	X	Y
1	51.29	96.59	52.24	97.69	52.22	96.25	51.09	96.18
2	84.83	95.18	85.76	96.65	85.71	95.10	84.43	95.06
3	130.57	247.68	130.16	249.31	130.22	247.90	129.15	247.91
4	162.89	246.45	162.46	248.51	162.34	246.86	160.93	246.97
5	114.92	169.55	115.31	171.12	115.28	169.73	114.10	169.66
6	147.21	168.31	147.61	170.17	147.75	168.70	146.52	168.60
7	302.92	213.52	302.69	216.87	302.89	215.00	301.65	215.11
8	333.68	212.36	333.45	215.89	333.67	214.00	333.22	214.16

TABLE 1 STAR LOCATIONS ON MATRICES S1 - S4

of fiducial points where the location of the same piece of the electronograph image is known in each of the 384 x 384 matrices.

If the general form of the transformation in X and Y, to link corresponding elements on two matrices is known, then these fiducial points can be used to determine the exact form of the relationship Any differences in the co-ordinates of the spatially identical electronographs are due to misalignment of the electronographs on the P.D.S. machine at digitisation, and will be eliminated in the next stage of matrix alignment. The co-ordinate system, which describes the position of any point on one matrix, is assumed to be linearly translated and rotated with respect to the XY co-ordinate system of the second matrix. The co-ordinates of any point on matrix B should be given by a linear transformation of the co-ordinates of the same point on matrix A, i.e.

$$X_2 = a + b X_1 + c Y_1 \qquad 5.2$$

$$Y_2 = d + e X_1 + f Y_1 \qquad 5.3$$

where the subscripts 1 and 2 refer to the co-ordinates on the first and second matrices respectively, and the coefficients a-f have to be determined to give the exact form of the transformation. The positions of the fiducial stars (X_1, Y_1), (X_2, Y_2), provide the necessary information for the solution of the coefficients a - f.

More fiducial points per matrix were known than the number of parameters to be determined, so a least squares fit was made by a computer program to determine the best value for the coefficients Comparison of the predicted and true values for the fiducial points on the second matrix, gives an indication of the goodness of fit of the

linear transformation used.

The fiducial stars on matrices 2, 3 and 4 of each series were compared with those on matrix 1, and a set of coefficients, linking the location of an element of the image on matrix 1 with the location of the same element on each of the other matrices was obtained.

As an example, Table 2 shows the coefficients arrived at for the transformation between matrices S1 and S4, and the computed values of the fiducial star locations on matrix 4 (X_2^t, Y_2^t) using the coefficients, are compared with the true values (X_2, Y_2).

The close agreement between (X_2, Y_2) and (X_2^t, Y_2^t) indicates that the linear transformation is accurate to approximately 2 microns on the electronograph, which corresponds to 0.15 seconds of arc. The spatial resolution of the final polarisation map aimed at is $\sim$ 10 seconds of arc, so that the alignment achieved by the linear transformation should be more than adequate.

5.5.3. Transformation of the Matrices

Although the coefficients make it possible to locate the same point on all four matrices, the task of rewriting the matrices corresponding the second, third and fourth electronographs, so that the same information is contained in the same element of the matrix for all four matrices, is not entirely straightforward. The transformation of an initial pixel on matrix S1, which has integer co-ordinates in X and Y between 1 and 384 will give a fractional location for the same pixel in matrices S2, S3 and S4. This is illustrated in figure 5.14, where it is attempted to find the density on matrix S2 corresponding to the density

COEFFICIENTS

a = 0.665319 b = 0.99953 c = -0.0089

d = -0.79468 e = 0.007969 f = 0.9998

STAR	X_1	Y_1	X_2	Y_2	X_2^t	Y_2^t
1	51.29	96.59	51.09	96.18	51.07	96.18
2	84.83	95.18	84.43	95.06	84.61	95.04
3	130.57	247.68	129.15	247.91	128.97	247.68
4	162.89	246.55	160.93	246.97	161.28	247.00
5	114.92	169.55	114.10	169.66	114.02	169.64
6	147.21	168.31	146.52	168.60	146.31	168.65
7	302.92	213.52	301.65	215.14	301.54	215.10
8	343.68	212.36	332.22	214.16	332.30	214.18

TABLE 2 TRANSFORMATION COEFFICIENTS FOR MATRIX S4

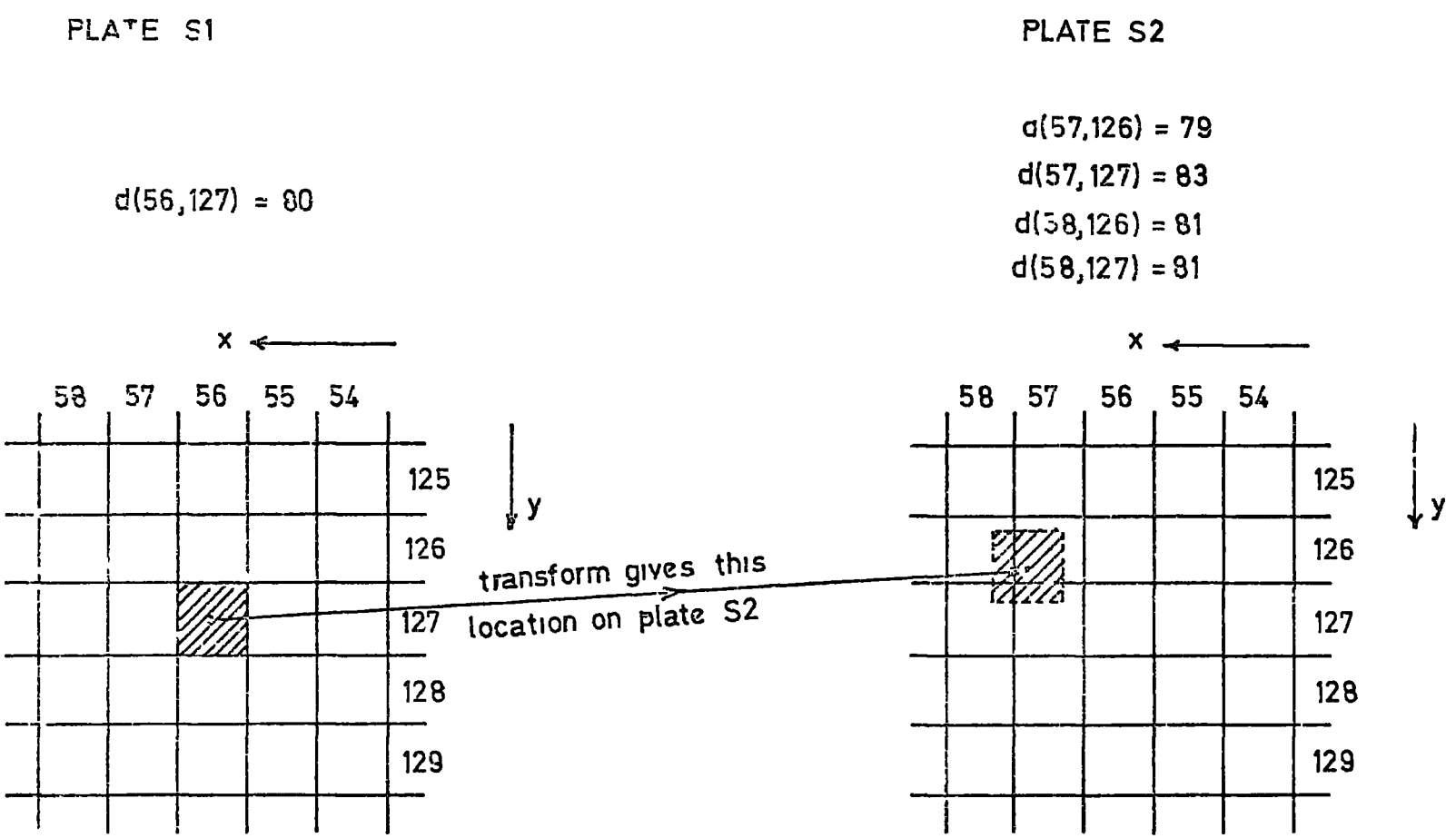

$$d(57.3, 126.3) = 0.49\,d(57,126) + 0.21\,d(57,127) + 0.21\,d(58,126) + 0.09\,d(58,127)$$

$$= 80$$

FIG 5.14 DETERMINING A CORRESPONDING DENSITY ON MATRIX S2

in pixel (56, 127) of matrix S1. Applying the coefficients for matrix S2 to the co-oidinates of the pixel on matrix S1 gives a location of (57.3, 126.3) on matrix S2. The density on matrix S2 however, is only recorded in integer units of X and Y, which means that the nearest pixels to the required one are (57, 126), (58, 126), (57, 127), (58, 127). The density required for matrix S2, is for a 24 micron squared bin centred at (57 3, 126.3) and is shown by the dashed square.

A first approximation, might be to take the density at (57, 126) on matrix S2, as this is the area which most closely approximates the required one. A better approximation however, is to take fractional parts of the densities in all four pixels which are overlapped by the required area; the fraction of each pixel taken being proportional to the amount of overlap the required area makes with that pixel. This approximation amounts to a linear interpolation between pixels. The figure shows the density computed for the non-integer location (57.3, 126 3).

Using the coefficients for a particular matrix, and the interpolation technique described, the entire matrices S2, S3, S4 and S6, S7, S8 were rewritten pixel by pixel so that a one to one correspondence existed between all the elements for a particular series. (S2 when rewritten, would have a density of 80 recorded in pixel (56, 127)).

The accuracy of the matrix alignment, can be checked by finding the positions of the fiducial stars on the transformed matrices (denoted by S1T - S8T), to see if they occur at exactly the same location on each matrix The result of rerunning the star finding program on the transformed matrices is shown in Table 3, inspection of which confirms that

PLATE → / STAR ↓	S1T		S2T		S3T		S4T	
	X	Y	X	Y	X	Y	X	Y
1	51.29	96.59	51.24	96.60	51.26	96.64	51.27	96.66
2	84.83	95.18	84.77	95.19	84.72	95.17	84.73	95.18
3	130 57	247.68	130.59	247.65	130.73	247.72	130.80	247.73
4	162.89	246.45	162.85	246.61	162.82	246.44	162.62	246.52
5	114.92	169.55	114.97	169.64	114.97	169.62	115.00	169.58
6	147.21	168.31	147.26	168.29	147.29	168.32	147.37	168.29
7	302.92	213.52	302.87	213.52	302.89	213.62	302.96	213.63
8	333.68	212.36	333.64	212.29	333.66	212.31	333.70	212.31

TABLE 3 STAR LOCATIONS ON THE TRANSFORMED PLATES

a matrix alignment to an accuracy of approximately 2 microns has been achieved.

If a particular area is chosen on matrix S1T, in a position corresponding to a right hand grid image, and the density d_1 read out of the matrix, then the densities d_3, d_5 and d_7 can be immediately read for the same location on matrices S2T, S3T and S4T. (The symbol 'd' is used for the density read from the matrix, because the noise must be subtracted before this density is proportional to the intensity of the transmitted light 'i')

It is only necessary now, to know the translation necessary to go from ar element (or pixel) in a right hand grid image, to the element which contains the density for the same piece of the image in the left hand grid to determine the remaining densities d_2, d_4, d_6 and d_8.

5.6 The Strip to Strip Transformation Coefficients

The method of determining the location and density of a pixel in the left hand strip corresponding to a given pixel in a right hand strip, is done in a similar manner to the image location from matrix to matrix. It is again assumed that a linear transformation is sufficent to describe the translation necessary to go from a point (X^R, Y^R) in a right hand strip to the corresponding point (X^L, Y^L) in the left hand strip. The equations have a similar form to those of section 5.5.2. and the transformation is given by

$$\Delta X = a' + b' X^R + c' Y^R \qquad 5.4$$

$$\Delta Y = d' + e' X^R + f' Y^R \qquad 5.5$$

where $\Delta\bar{X}$ and ΔY are the differences in X and Y co-ordinates for the corresponding points (X^R, Y^R, X^L, Y^L).

The fiducial stars on the transformed plates again provide a set of data points where X^R, Y^R, ΔX, ΔY are known, and a least squares technique was used to solve for the coefficients a'-f'. Table 4 shows the value of the coefficients, together with the experimental and best fit values of ΔX and ΔY for each of the image pairs of fiducial stars. An integer location for a right hand strip pixel will again transform to a fractional value of the left hand strip pixel, and the interpolation method described in section 5.5.3. must be applied to determine a right hand strip density.

5.7 Reading out the Densities D_1 - D_8 from the Matrices

Although the electronographs are initially digitised at a 24 micron bin size, to provide the high spatial resolution necessary for accurate alignment, the density sets for the individual pixels (d_1 - d_8) are not suitable for reduction to polarisation parameters. This is because the fluctuations due to the photo-cathode sensitivity variations, PDS noise, scratches on the emulsion, and specks of dust in the polarimeter, are too large. It was therefore decided to integrate the individual 24 micron bins up to a size of 120 microns squared, (by adding the relevant 25 densities), before reduction. This 'irons out' the fluctuations, and gives a convenient spatial resolution of 7.5 arc seconds squared.

The grid images are approximately 30 pixels wide and 300 pixels long, which means that after summation into the larger 5 x 5 units, it is possible to obtain the integrated density sets (D_1 - D_8) for more than

COEFFICIENTS

$a' = 34.27$ $b' = 0.00849$ $c' = 0.00453$

$e' = -1.6037$ $f' = -0.00012$ $g' = 0.00184$

STAR	X	Y	ΔX	ΔY	ΔX^t	ΔY^t
1	57.29	96.59	33.50	-1.44	33.40	-1.43
3	130.57	247.68	32.12	-1.17	32.04	-1.16
5	114.92	169.55	32.32	-1.29	32.53	-1.25
7	302.92	213.52	30.76	-1.25	30.73	-1.25

TABLE 4. THE STRIP TO STRIP COEFFICIENTS

300 locations in each right hand grid width.

The procedure adopted to read out the densities for a particular set of grid images (left and right hand), is illustrated in figure 5.15. The network of small squares represents the matrix, each square being the area of the electronograph covered by a 24 micron pixel, and for which a density is recorded in the matrix. The image of a pair of grids is shown superimposed to indicate the area of the matrix corresponding to the photocathode grid image (c.f. the contour map shown in figure 5.3). The large squares in the left hand strip are the integrated areas for which the densities and hence polarisation parameters are to be calculated. The density for a large area (D_1, if the area is in a right hand grip on plate S1T for example), is found by adding up the 25 individual densities of the pixels contained in the large square

For each of the individual pixels in the right hand strip, the density of the corresponding area in the left hand strip can be found using the coefficients and interpolation procedure described in the previous two sections. These values can then be summed to give the density of the corresponding 120 x 120 micron area in the left hand strip (e.g. D_2). As the four matrices bear a one to one correspondence, this can be repeated for matrices S2T, S3T, S4T to obtain the remainder of the integrated densities (D_3 - D_8), for the particular element of the image covered by the large square. The only further information required before the several thousand density sets (D_1 - D_4) can be read from the matrices, is the X locations in the right hand grid images at which the integrated areas are to be taken. These are easily estimated from the contour map, and a set of X locations is shown for the grid illustrated

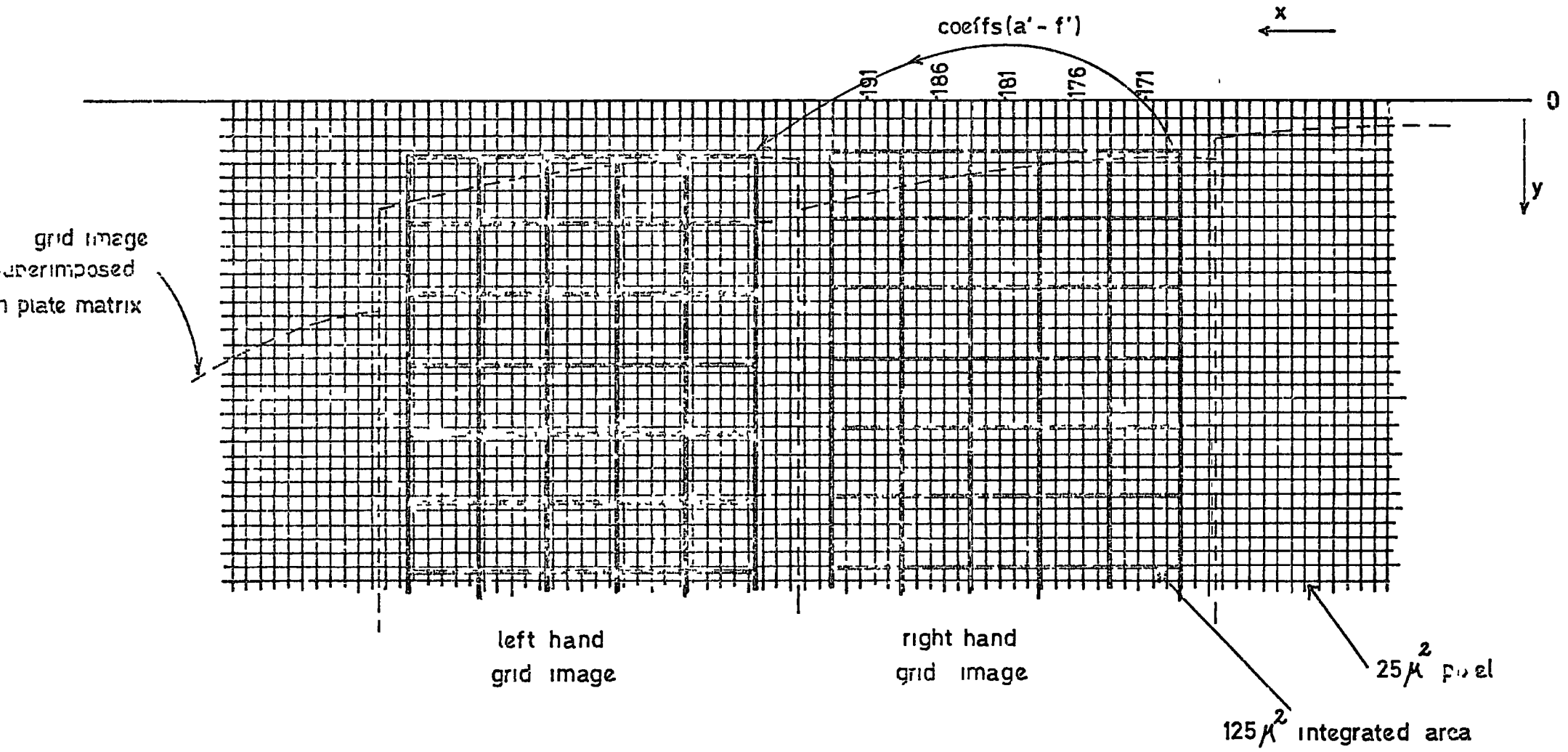

FIG 5.15 READING OUT THE DENSITIES

in figure 5.15. As the grids are approximately parallel to the Y scan axis, once an X location has been decided, the bins are integrated along the length of the Y axis without changing the X value.

A program was developed which took the X co-ordinates in turn (see figure 5.15), and for each of them, traversed the length of the matrix in Y in steps of 5, calculating and storing for each step, in a separate data set, the 25 densities to be integrated in the right hand strip, and the corresponding densities in the left hand strip. The XY location of the particular 120 micron squared bin was also stored for future use.

Although it would have been easy to sum the 25 densities at this stage, so reducing storage by a factor of 25, the individual densities were retained so that a quality control test could be applied to each of them, before they were included in the integrated sum. This was repeated for each of the matrices S1T - S4T, so that the eight sets of 25 component densities for an integrated area could be immediately accessed for any location on the matrices.

(The reduction procedure applied to the matrices S5T - S8T, is exactly the same as that for matrices S1T - S4T. For reasons of brevity the reduction procedure is only described as being applied to the latter set of matrices).

5.8 Subtraction of the Noise

The densities extracted from the matrices in the manner described, are inclusive of the noise component, and this must be subtracted before the true density, due to the polarised light signal can be obtained As described in section 5 3 2 , the noise would normally have a constant

value for a particular electronograph, but the effect of the PDS machine instability is to make it a slowly varying function of the Y axis of the matrix. The variation must be monitored, so that the correct value to be subtracted for a particular pixel at location (X, Y) on the matrix can be ascertained.

The noise on each matrix was recorded, by using a modified version of the program described in section 5.7. The densities were read out for each matrix in turn, taking a column of small X value ($\sim$ 5), where the total signal on the electronograph is due to the noise component alone. The 25 individual pixels for each 125 micron squared location were averaged, and the 75 mean values for the density, as Y varied from 6 to 381 (in steps of 5) were stored for each of the matrices.

Each of the density data sets described in the previous section, were taken in turn, and the relevant values for the noise density subtracted from each of the 25 component densities in each of the 8 sets corresponding to the densities $D_1 - D_8$. The component densities are therefore given by

$$r_j^k = d_j^k - n_l^m \qquad 5\ 6$$

$k = 1, 2 \ldots 25$

$j = 1, 2 \ldots 8$

$l = 1, 2, 3, 4$

$m = 1, 2 \ldots 75$

where 'd' is the initial density of a component pixel, 'n_l^m' is the relevant noise density as a function of Y position on the first, second, third or fourth matrix, and 'r' is the residual density

proportional to the transmitted intensity. the subscript 'j' describes the eight polarised images, and the superscript 'k' the 25 component densities in each of these eight integrated areas.

The densities (i_1 - i_8) for a particular 120 micron squared area of the image, from which the polarisation parameters can be calculated according to the equations given in Chapter 4, are given by

$$i_j = \sum_{k=1}^{k=25} i_j^k \qquad 5\ 7$$

$$j = 1, 2 \ldots\ldots 8$$

5.9 Reduction to Polarisation Parameters

5.9.1. Quality Control

Before summing the sets of 25 component pixels of an integrated area, the individual pixels were first examined to try and filter out any erroneous density values (i_j^k) caused by scratches or specks of dust. These could then be excluded from the summation to find the density of the integrated area (i_j), which would then need renormalisation to a density for 25 components

Although the fluctuations are too great, to use the component density sets (i_1^k - i_8^k) for reduction to polarisation parameters, they can be used to try and locate any erroneous density values in a particular set Each of the 25 sets of (i_1^k - i_8^k) can be substituted in the equations of Chapter 4. The first step in the reduction equations, is to calculate the two independent estimates of the sensitivity factor 'f_1' and 'f_2' given by equations 4.4 and 4 7. If these two estimates of the same quantity do not agree, one of the densities (i_1^k - i_8^k) from

which they were calculated must be wrong. As there is no straightforward way to deduce which is the erroneous value, the complete set of eight component densities must be omitted from the summation. Because the normal fluctuations in the densities of the individual pixels is quite large, ($\sim$ 10%), the 'f' factor agreement criterion cannot be too strict, or perfectly normal, yet highly fluctuating densities will be filtered from the summation. The quality control described, while filtering out the fairly large defects from the electronographs, can therefore not be expected to remove all the erroneous density values.

Each of the data sets was read from storage, and the 25 components subjected to the quality control described. After the erroneous values had been filtered out, the remaining densities were summed and renormalised to a density for 25 components

5.9.2 Polarisation Parameters

The density set (i_1 - i_8) was read for each integrated area, and the values of (i_1 - i_8) were inserted into the equations described in Chapter 4. The 'f' and 'e' factors, together with the Stokes parameters and the final descriptive units 'p' and 'θ' were calculated for each location on the matrix. The numerical results were displayed as line printer output as shown in figure 5.16 and also stored for later use The figure shows a typical page of line printer output, with the polarisation parameters calculated for each X Y location of an integrated area on the matrices S1T - S4T.

5.10 The Results Displayed Visually and their Interpretation

5.10.1. Introduction

The form of the polarisation map produced, is not easily discerned

X	Y	f_1	f_2	f	ℓ_1	ℓ_2	ℓ_3	I	Q_1	Q_2	Q	U_1	U_2	U	P_1	P_2	P	θ_1	θ_2	θ
183	266	1.01	0.95	1.00	0.97	0.93	0.93	1495.	-71.	-55.	-63.	-13.	-30.	-21.	4.8	4.2	4.4	84.8	75.8	80.6
183	271	1.00	1.00	1.00	0.88	0.85	0.86	1380.	-44.	-45.	-45.	1.	2.	2.	3.2	3.2	3.2	-89.1	-88.7	-88.9
183	276	1.00	0.90	0.95	0.97	0.95	0.95	1330.	-90.	-25.	-58.	-64.	-132.	-98.	9.3	10.1	9.6	72.3	50.4	60.2
183	281	1.00	1.01	1.00	0.97	0.83	0.85	1250.	-56.	-65.	-61.	-14.	-5.	-9.	4.6	5.2	4.9	83.3	87.9	85.7
183	286	1.01	1.01	1.01	0.94	0.80	0.82	1245.	-67.	-63.	-65.	-14.	-20.	-18.	5.5	5.3	5.4	83.2	81.4	82.3
183	291	1.00	1.04	1.02	0.86	0.81	0.79	1192.	-34.	-60.	-47.	13.	38.	26.	3.1	6.0	4.5	-79.8	-73.8	-75.8
183	296	1.01	0.97	0.99	0.91	0.84	0.81	1162	-70.	-47.	-58.	37.	13.	25.	6.8	4.2	5.5	-76.0	-82.0	-79.3
183	301	1.02	1.04	1.03	0.81	0.76	0.81	1189.	-51.	-65.	-58.	1.	15.	8.	4.3	5.6	4.9	-89.4	-83.6	-86.1
183	306	0.99	1.06	1.02	0.66	0.77	0.82	1185.	-71.	-111.	-91.	-13.	27.	7.	6.1	9.7	7.7	84.7	-83.3	-87.8
183	311	1.01	0.99	1.00	0.83	0.80	0.84	1155.	-77.	-62.	-70.	31.	15.	23.	7.2	5.5	6.3	-73.2	-83.3	-80.9
183	316	1.04	1.03	1.03	0.82	0.76	0.84	1114.	-86.	-82.	-84.	9.	6.	7.	7.8	7.4	7.6	-86.9	-88.1	-87.5
183	321	0.98	1.00	0.99	0.94	0.80	0.82	1094.	-74.	-84.	-79.	-18	-8.	-13.	7.0	7.7	7.3	83.1	87.1	85.2
183	326	0.96	1.01	0.98	0.80	0.79	0.84	1139.	-19.	-50.	-34.	-21.	9.	-6.	2.5	4.5	3.1	65.9	-85.0	84.5
183	331	0.97	1.07	1.02	0.92	0.93	0.93	1020.	-24.	-75.	-50.	-32.	18.	-7.	3.9	7.6	4.9	53.4	-83.4	86.0
183	336	0.96	0.97	0.96	0.85	0.90	0.90	1124.	-12.	-16.	-14.	-38.	-36.	-37.	3.7	3.5	3.6	53.5	57.0	55.2
183	341	0.98	0.99	0.98	0.84	0.83	0.84	1055.	-29.	-35.	-32.	1.	6.	4.	2.8	3.4	3.1	-89.2	-84.8	-86.8
183	346	1.00	0.98	0.99	0.96	0.95	0.95	938.	-20.	-14.	-17.	-22.	-29.	-25.	3.2	3.4	3.2	66.4	59.0	62.1
183	351	1.00	0.99	1.00	0.85	0.88	0.91	1008.	-32.	-27.	-30.	-14.	-21.	-17.	3.5	3.3	3.4	78.	72.1	75.1
183	356	1.03	1.06	1.05	0.90	0.84	0.89	1025.	-35.	-50.	-43.	-40.	-34.	-42.	5.9	5.9	5.9	62.8	72.8	67.8
183	361	0.99	0.99	0.99	0.78	0.81	0.76	1100.	-31.	-31.	-31.	-18.	-19.	-18.	3.3	3.3	3.3	74.8	74.6	74.7
183	366	1.01	0.98	1.00	0.75	0.81	0.82	1080.	-34.	-21.	-27.	-7.	-20.	-14.	3.2	2.7	2.8	84.1	67.9	76.7
183	371	0.99	0.99	0.99	0.92	0.90	0.90	950.	-98.	-99.	-98.	29.	30.	29.	15.7	15.9	15.8	-81.7	-81.6	-81.7
183	376	0.97	0.97	0.97	0.78	0.79	0.83	966.	-304.	-303.	-304.	93.	97.	97.	87.3	87.1	87.2	-81.1	-81.2	-81.1
188	11	0.98	0.96	0.97	0.82	0.90	0.93	531.	-63.	-59.	-61.	22.	18.	20.	12.5	11.7	12.1	-81.5	-81.5	-81.6
188	16	0.96	0.91	0.94	0.91	0.84	0.76	1082.	-50.	-23.	-37.	33.	6.	20.	5.6	2.2	3.8	-73.2	-82.9	-75.9
188	21	1.01	1.03	1.02	0.86	0.86	0.76	1073.	-23.	-31	-27.	-23.	-16.	-19.	3.1	3.2	3.1	67.6	76.7	72.3
188	26	1.00	0.99	1.00	0.87	0.85	0.79	1063.	-19.	-15.	-17.	-15.	-19.	-17.	2.3	2.3	2.3	70.3	64.3	67.3
188	31	1.00	1.02	1.01	0.86	0.81	0.80	1073.	-21.	-29.	-25.	-22.	-14.	-18.	2.8	3.1	2.9	66.4	76.9	71.8
188	36	0.98	1.04	1.01	0.89	0.80	0.84	1056.	-8.	-35.	-23.	-31.	-5.	-18.	3.0	2.7	2.7	52.0	89.7	73.1
188	41	0.93	0.98	0.95	0.85	0.95	0.81	1060.	-18.	-46.	-32.	-41.	-13.	-27.	4.2	4.5	3.9	59.9	87.1	79.
188	46	0.96	0.98	0.97	0.85	0.81	0.73	10 ..	-29.	-37.	-32.	-40.	-32.	-36.	4.5	4.5	4.5	62.4	69.9	66.0
188	51	1.05	0.92	0.98	0.82	0.76	0.81	1149.	-113.	-32.	-67.	-44.	-119.	-81.	9.4	10.4	2.9	78.5	52.5	64.8
188	56	0.98	0.87	0.92	0.99	0.92	0.79	1167.	-65.	4.	-31.	99.	27.	63.	10.2	2.3	6.0	-81.5	-41.2	-57.9
188	61	1.00	0.96	0.98	0.95	0.91	0.85	1063.	-29.	-4.	-16.	22.	-4.	9.	3.4	0.5	1.8	-71.6	68.6	-75.7
188	66	1.01	0.97	0.99	0.93	0.89	0.84	1125.	-53.	-34.	-44.	-30.	-48.	-39.	5.4	5.3	5.2	75.3	62.7	69.0
188	71	0.95	0.96	0.96	0.85	0.86	0.8	1151.	-49.	-57.	-53.	-40.	-33.	-37.	5.5	5.7	5.6	70.4	75.1	72.8
183	76	0.95	1.02	0.98	0.84	0.85	0.82	1117.	-0.	-27.	-9.	-56.	-22.	-39.	5.1	3.1	4.6	40.7	70.4	51.5
188	81	1.00	0.94	0.97	0.82	0.8.	0.79	1164.	-61.	-22.	-41.	22.	-18.	2.	5.5	2.5	3.6	-80.2	70.5	-88.7
188	86	0.95	1.03	0.99	0.84	0.81	0.78	1213.	-15.	-66.	-41.	-81.	-33.	-57.	6.9	6.1	6.5	50.3	76.8	62.7
188	91	0.97	1.03	1.00	0.82	0.85	0.76	1163.	-11.	-46.	-29.	-41.	-7.	-24.	3.7	4.0	3.2	52.4	85.7	69.9
188	96	1.01	1.01	1.01	0.87	0.83	0.75	1142.	-40.	-44.	-42.	-55.	-51.	-53.	5.9	5.8	5.9	53.0	65.4	64.2
188	101	0.98	0.95	0.97	0.83	0.84	0.82	1212.	-74.	-62.	-68.	-36.	-5 .	-43.	7.0	6.6	6.7	77.5	70.5	74.1
188	106	0.97	0.98	0.98	0.85	0.86	0.81	1229.	-47.	-53.	-50.	-44.	-38.	-41.	5.2	5.3	5.3	68.4	72.0	70.2

FIG 5 16 THE POLARISATION PARAMETERS AS LINE PRINTER OUTPUT

from the mass of numerical data displayed in figure 5.16, and the results were therefore displayed in a graphical form to make them more easily digestible. Scatter plots and frequency distributions of the interesting reduction parameters were computer plotted for the 2,000 locations taken on a series of electronographs These are shown in figures 5.20 - 5.27 for the half of the image corresponding to matrices S1T - S4T. The actual form of the produced map for the two series of matrices (S1T - S4T, S5T - S8T), is shown in figures 5.17 and 5.18, where the polarisation of the light forming the image at each location on the electronograph is represented by a vector of length proportional to the degree of polarisation, and having the direction of the E vector of the linearly polarised component of the radiation. Figure 5 19 shows the two halves (which are completely independent of each other), aligned by eye, to give the complete polarisation map of the M82 area (Accurate alignment will be discussed in the next section).

5.10.2. The Polarisation Map

The map shown in figure 5.19 describes the polarisation of the total light signal forming the image at each point on the electronograph. It is therefore not the polarisation of the galactic light emanating from M82 alone, but includes a component, which must be subtracted out, due to the diffuse light of the night sky radiation which in itself can be partially plane polarised. The region of the map corresponding to the disk of M82 is drawn on the figure

The night sky component is clearly seen as a series of vectors of similar length and orientation around the edge of the map, where the

FIG 517 THE POLARISATION MAP FROM ELECTRONOGRAPHS 1 - 4

FIG 518 THE POLARISATION MAP FROM ELECTRONOGRAPHS 5-8

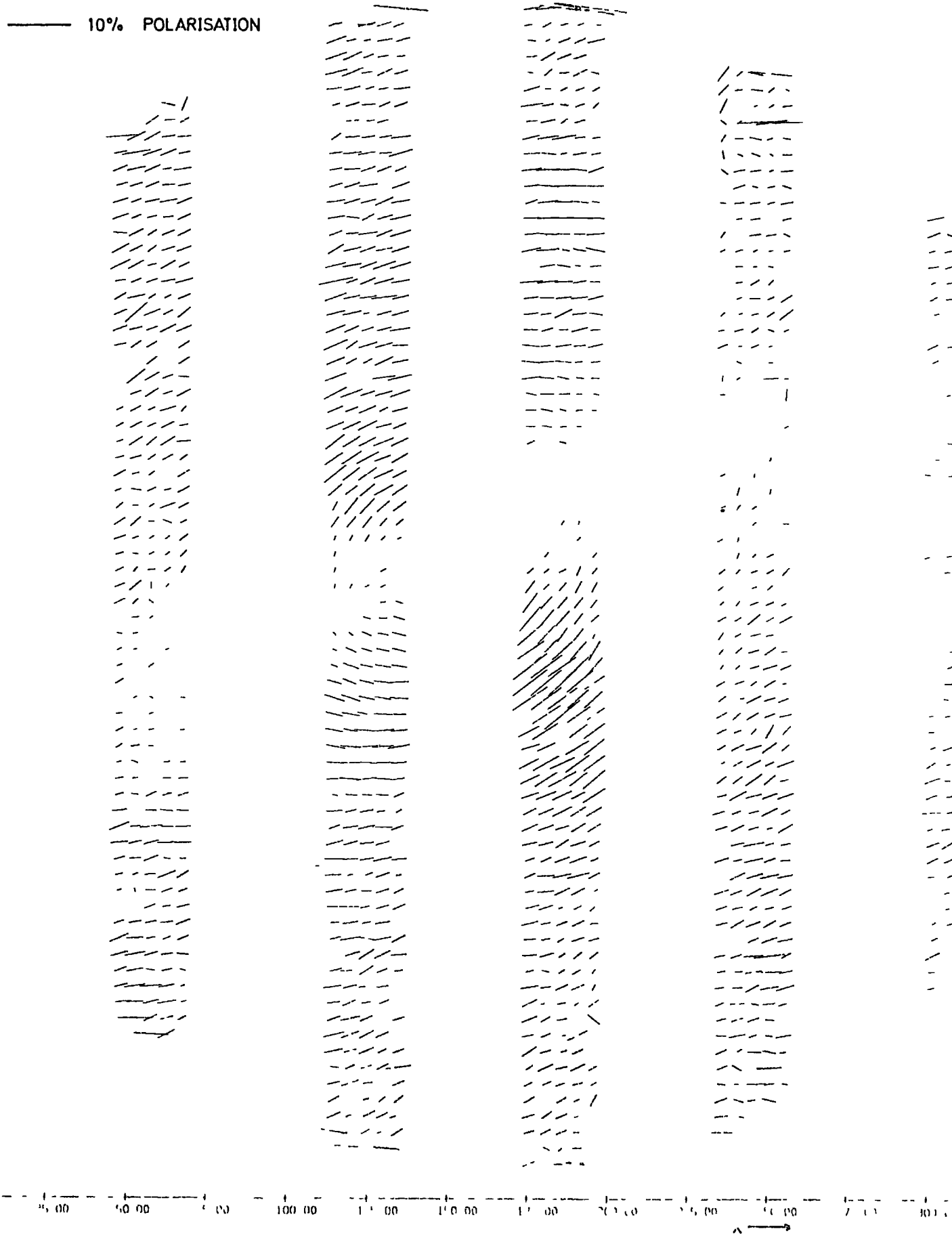

FIG 519 THE COMPLETE POLARISATION MAP OF THE GALAXY + NIGHT SKY

surface brightness of M82 is small, and the signal is almost entirely night sky. In the central regions of the map, where the galactic light flux is high, the contribution is mainly from M82. In this region, the characteristic pattern of the unpolarised disk, and highly polarised halo forming a smooth pattern, is easily distinguished.

5.10.3 The Graphical Output

We can look at the distributions of the various quantities (f, e, etc.), measured at each point, to ascertain the uniformity and quality of the results of the reduction technique As an example, the exposure factor 'e_1' between electronographs S2T and S1T must be a constant for the whole matrix. If all the independent estimates, obtained for each X Y location are not statistically distributed about a mean value, an error must have been incurred at some stage in the reduction procedure.

Figure 5.20 and 5.21 show the distributions of the estimates 'f_1' and 'f_2' of the photo-cathode sensitivity for all the points of the map. The distributions are peaked at 1.0 and have fallen to approximately half the mode for 'f' values of 0.96 and 1.04 This is consistent with the known photo-cathode characteristics for the random sensitivity variations of around 5%. The scatter plot of 'f_1' against 'f_2' shown in figure 5.22 yields the expected straight line at an angle of 45°

Figure 5.23 shows a frequency distribution of the estimates of the exposure factor 'e_1', between electronographs S1T and S2T. The distribution is of the expected form, and is centred around a mean value of 0.87, which is therefore the ratio of the total amount of light recorded

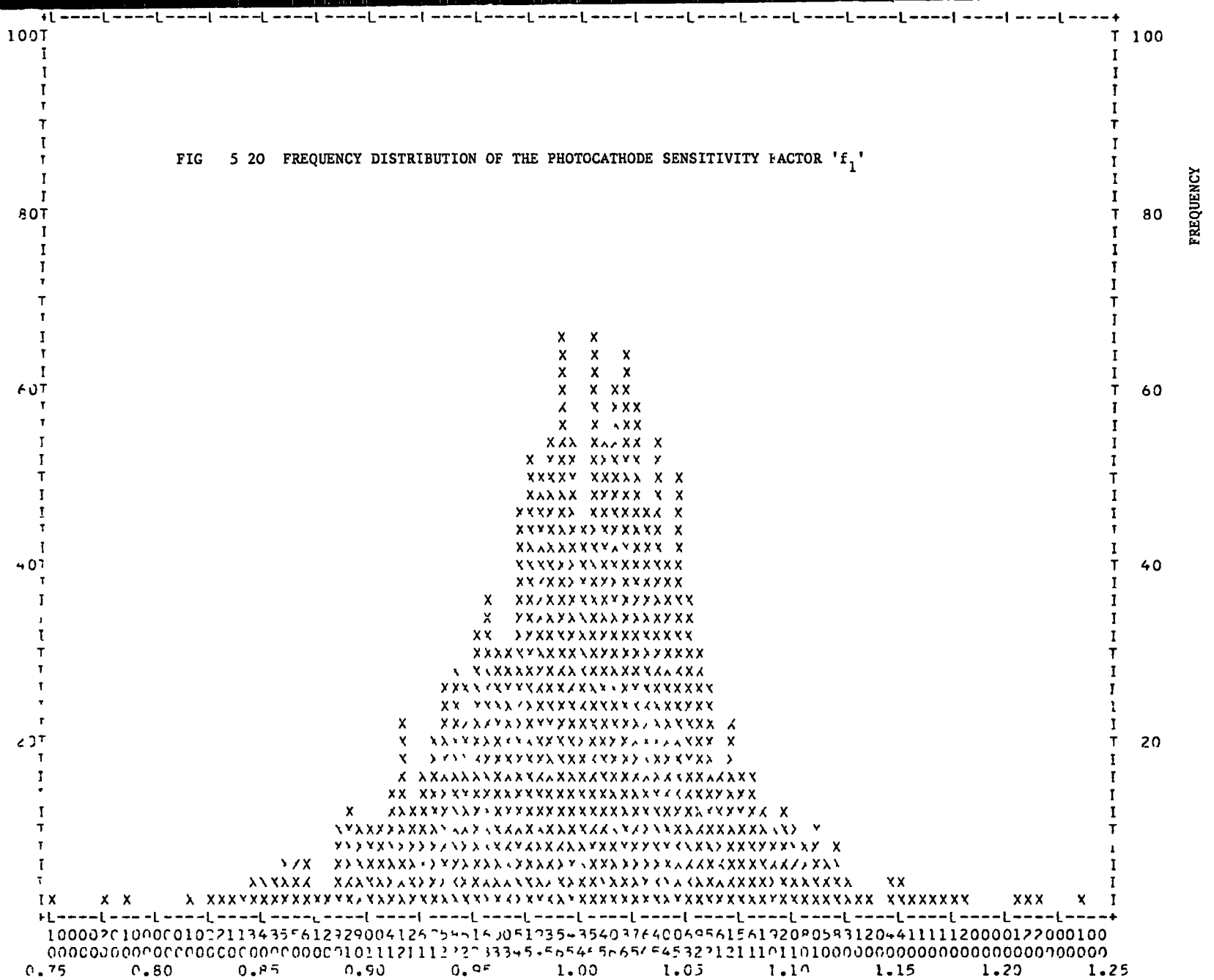

FIG 5 20 FREQUENCY DISTRIBUTION OF THE PHOTOCATHODE SENSITIVITY FACTOR 'f_1'

FIG 5 21 FREQUENCY DISTRIBUTION OF THE PHOTOCATHODE SENSITIVYT FACTOR 'f_2'

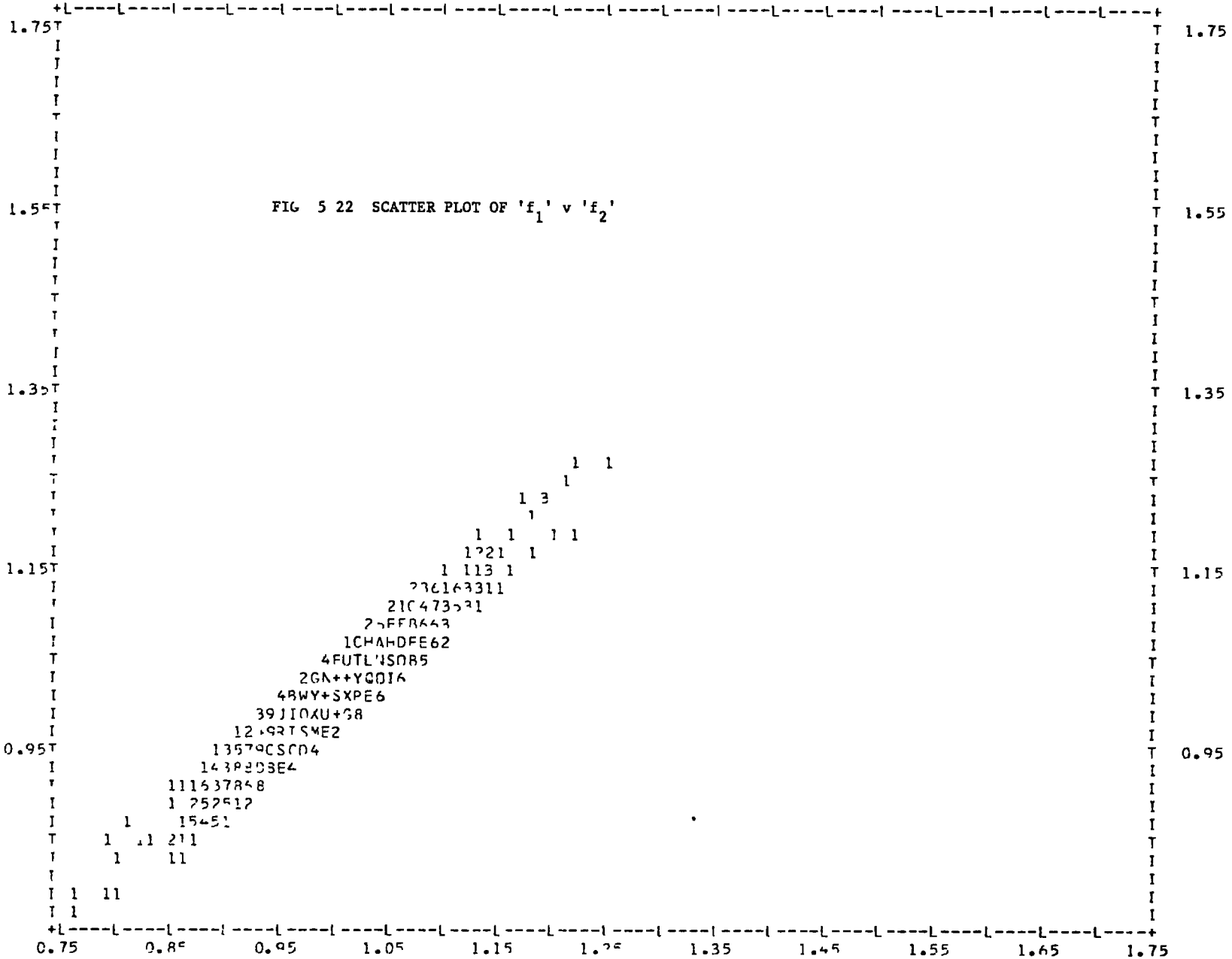

FIG 5 22 SCATTER PLOT OF 'f_1' v 'f_2'

I F1 F2 I

INSIDE 1487 OUT LOW 0 OUT HIGH 0 TOTAL 1487

DPLOT NUMBER 1

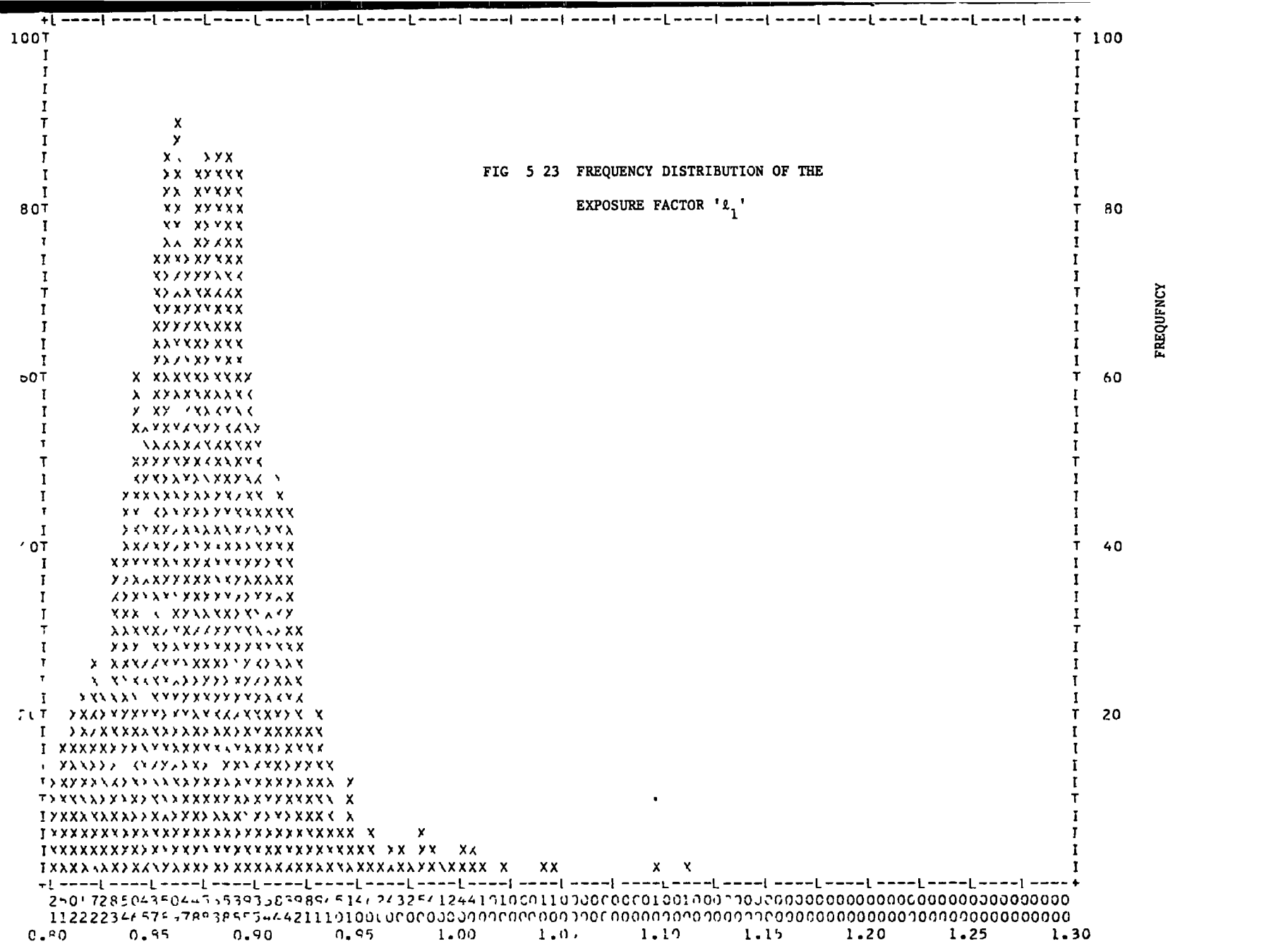

FIG 5 23 FREQUENCY DISTRIBUTION OF THE EXPOSURE FACTOR 'ℓ_1'

PLOT NUMBER 4

on the first and second electronographs. Figure 5.24 shows that the 'e_1' factor does not vary, if plotted against the Y axis of the matrix. This is a useful piece of information to ensure that the correct form of the Y variation of the noise has been subtracted in the reduction stages. Figure 5.25 shows an example of the 'e' factor scatter plot obtained, if a slightly incorrect set of noise values are subtracted.

The reduction equations yield two estimates of both the polarisation magnitude and angle for each plate location, and the distributions of the differences in the two estimates are shown in figures 5.26 and 5.27. The difference between the two estimates is an important quantity, because it is a measure of the uncertainty associated with the determination. The halfwidths of the distributions therefore gives an estimate of the mean uncertainty associated with a typical polarisation point plotted in figure 5.19.

It must be remembered, that those estimates of the errors on the polarisation are for the total light signal incident on the plate The subtraction of the sky signal, to obtain the polarisation parameters of the galactic light alone (see section 5.11) will introduce further errors into the polarisation parameters, the magnitude of which will depend on the ratio of the galaxy and sky signals respectively.

5.11 Subtraction of the Night Sky

The stored output from the reduction described in section 5.9 contains the Stokes parameters (IT, QT, UT) for each location on the plate. The parameters have been given a 'T' suffix, because they describe the total light signal incident at each location on the plate.

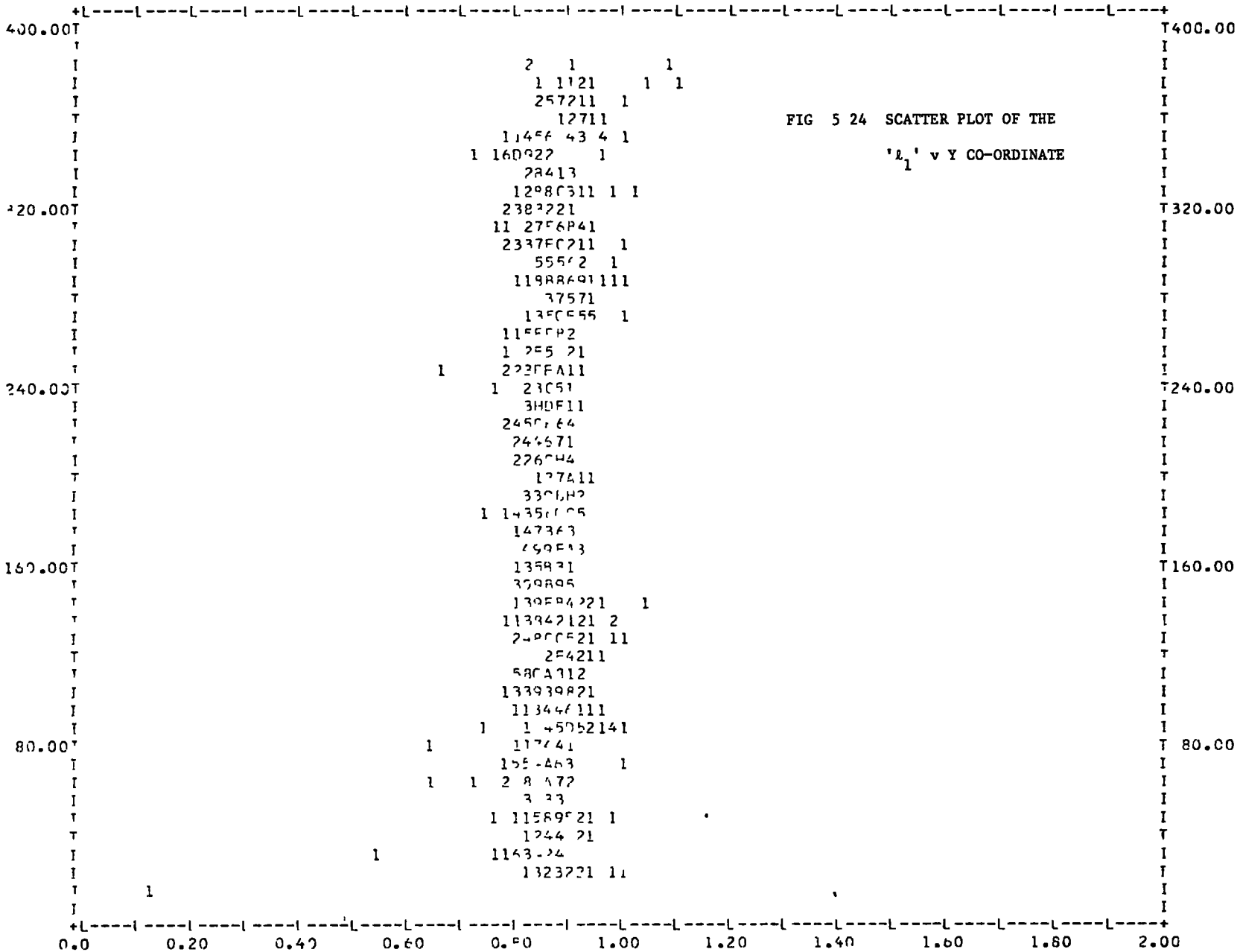
400.00
320.00
240.00
160.00
80.00
0.0
0.20
0.40
0.60
0.80
1.00
1.20
1.40
1.60
1.80
2.00
Y
FIG 5 24 SCATTER PLOT OF THE
'ℓ1' v Y CO-ORDINATE
ℓ1
OPLOT NUMBER 2
INSIDE 1487
OUT LOW 0 OUT HIGH 0
TOTAL 1487

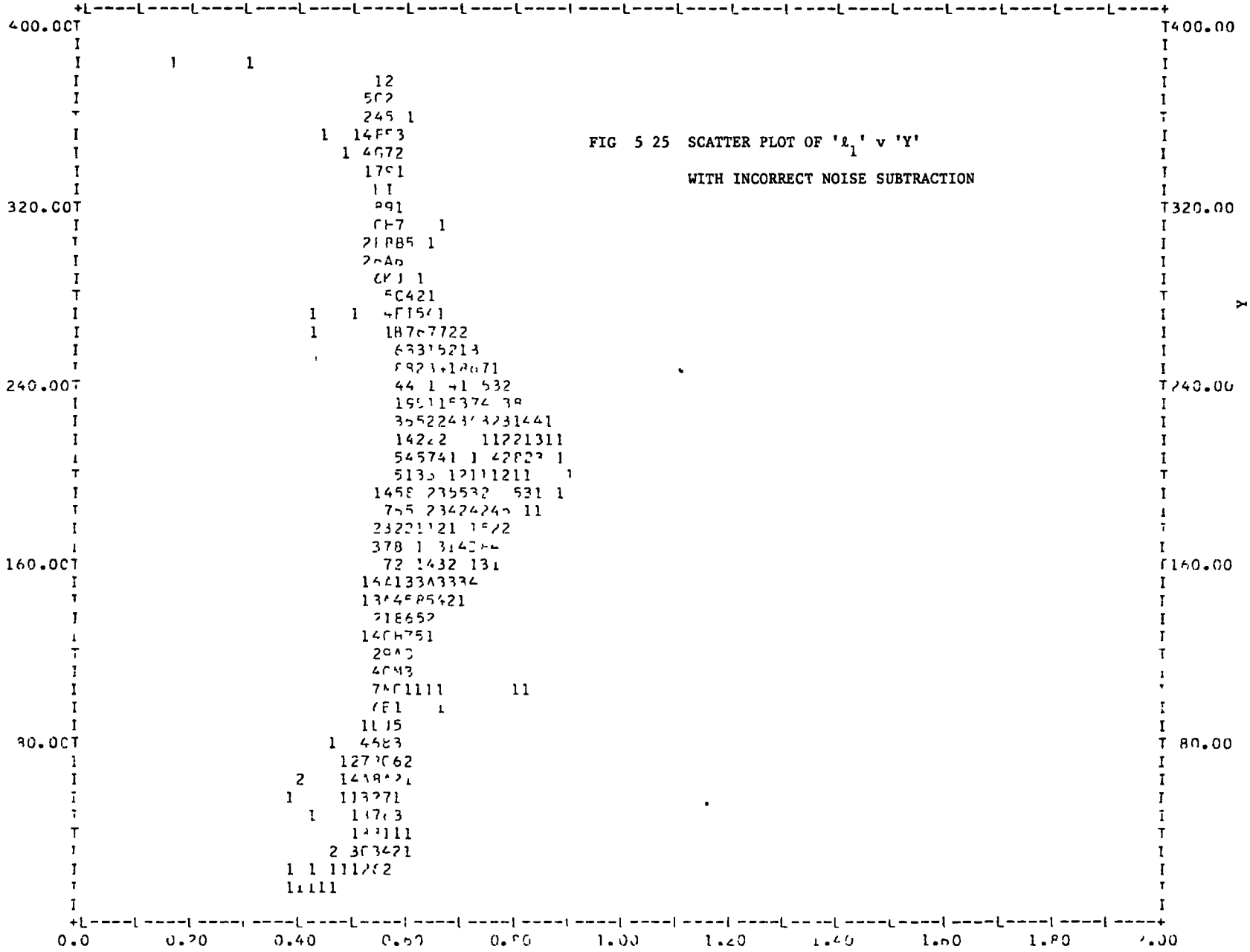

FIG 5 25 SCATTER PLOT OF 'ℓ_1' v 'Y'

WITH INCORRECT NOISE SUBTRACTION

I	Y	E1	I	ℓ_1	OPTION NUMBER 2

INSIDE 1449 CUT LOW 0 CUT HIGH 0 TOTAL 1449

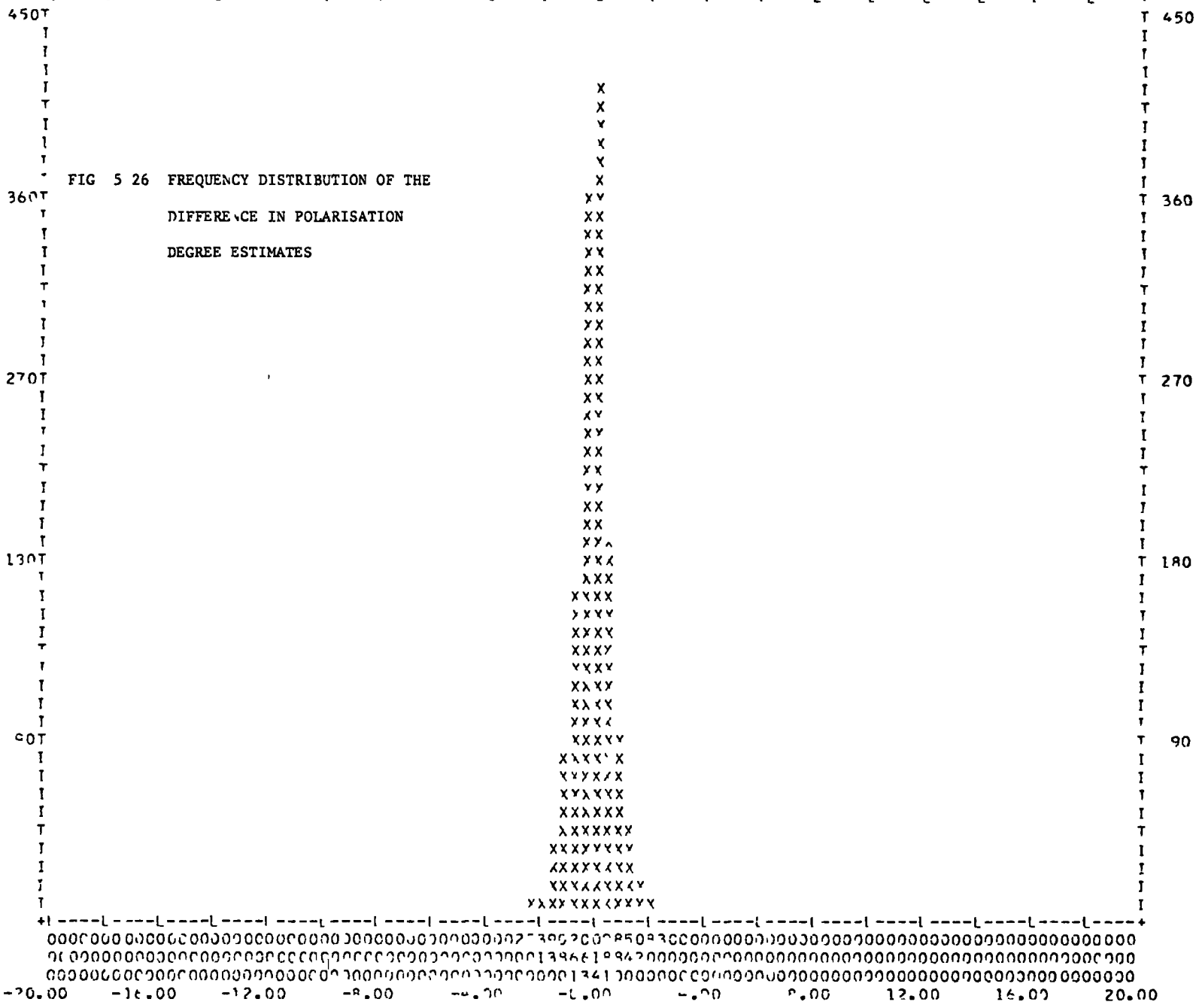

FIG 5 26 FREQUENCY DISTRIBUTION OF THE DIFFERENCE IN POLARISATION DEGREE ESTIMATES

PLOT NUMBER 2

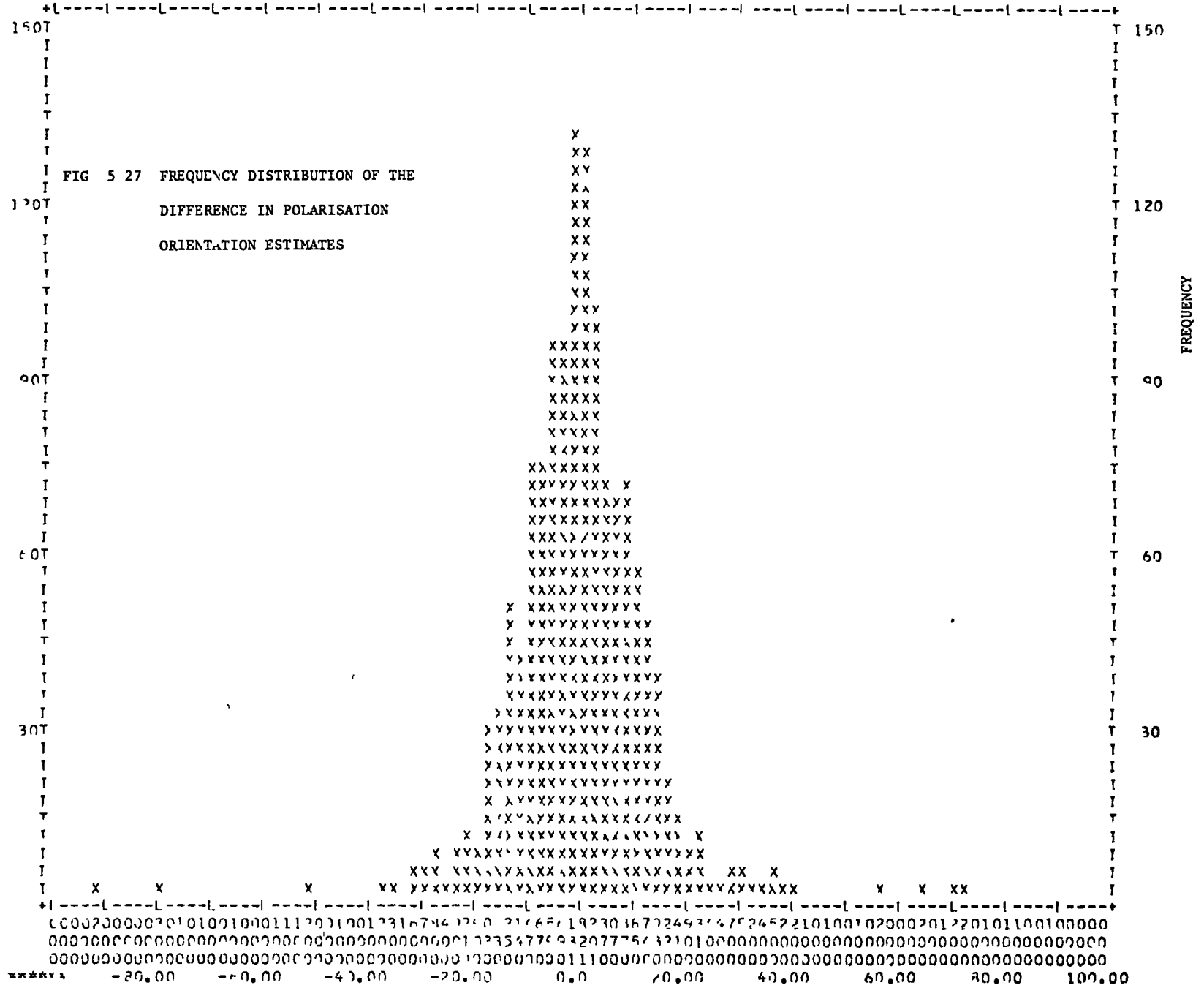

FIG 5 27 FREQUENCY DISTRIBUTION OF THE DIFFERENCE IN POLARISATION ORIENTATION ESTIMATES

It is therefore only necessary to find the mean value of the Stokes parameters for the sky component of the signal (IS, QS, US), and these values can be subtracted from the total to give the parameters for the galactic light (I, Q, U).

The outer areas of the plate, corresponding solely to sky signal, can be isolated by plotting a frequency distribution of the Stokes vector I for all the locations on the plate From the result, shown in figure 5.28, it is easy to identify the large peak at I = 1075 as being due to the sky signal, which should have a constant value independent of plate position. The tail on the distribution is due to the faint extended halo of M82 merging with the sky. If all the points on the plate are discarded, except those having a Stokes vector I between 1050 - 1100, then a distribution of the 'Q' and 'U' vectors of those remaining, will reveal the sky values for these two parameters. Figures 5.29 and 5.30 show the resultant plots from the sky parameters (IS, QS, US) were estimated as (1075, -38 0, -25.0) for the matrices S1T - S4T.

These values were subtracted from the total Stokes vectors for each location on the matrices, and the resulting polarisation parameters (p, θ) calculated from the modified Stokes vectors. The process was repeated on the matrices (S5T - S8T), and the corrected results showing the linear polarisation of the light emanating from M82 were replotted as shown in figure 5.31 (A contour showing the outline of the galactic disk is also plotted)

The peripheral regions of the original map (figure 5.19) correspond to sky signal only, and the resultant polarisation vectors after subtraction of this sky signal are simply statistical noise A cut on the

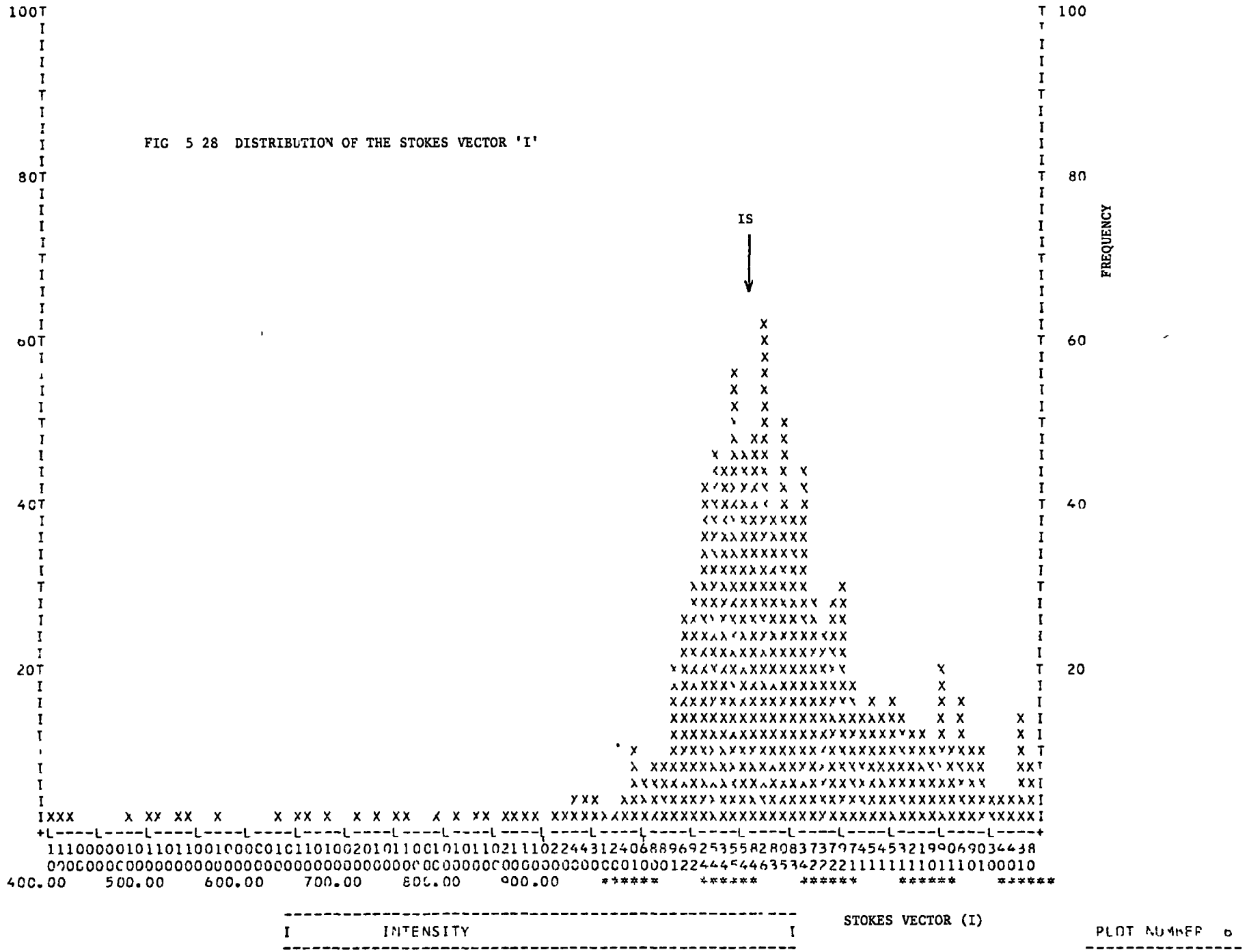
FIG 5 28 DISTRIBUTION OF THE STOKES VECTOR 'I'
IS
FREQUENCY
100
80
60
40
20
400.00
500.00
600.00
700.00
800.00
900.00
INTENSITY
STOKES VECTOR (I)
PLOT NUMBER 6

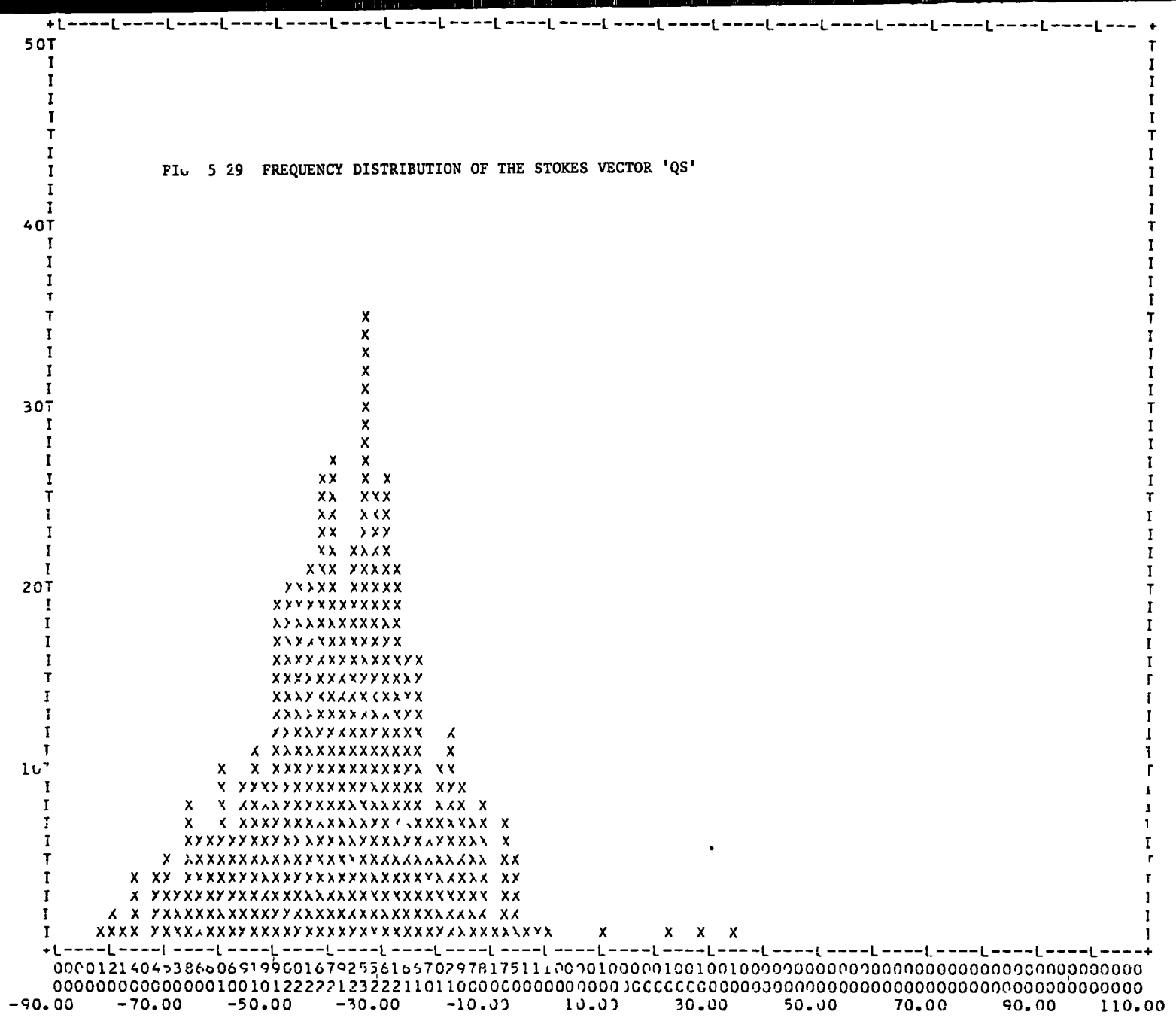
FIG 5 29 FREQUENCY DISTRIBUTION OF THE STOKES VECTOR 'QS'
FREQUENCY
50
40
30
20
10
-90.00
-70.00
-50.00
-30.00
-10.00
10.00
30.00
50.00
70.00
90.00
110.00
Q FOR SKY
QS
PLOT NUMBER 4

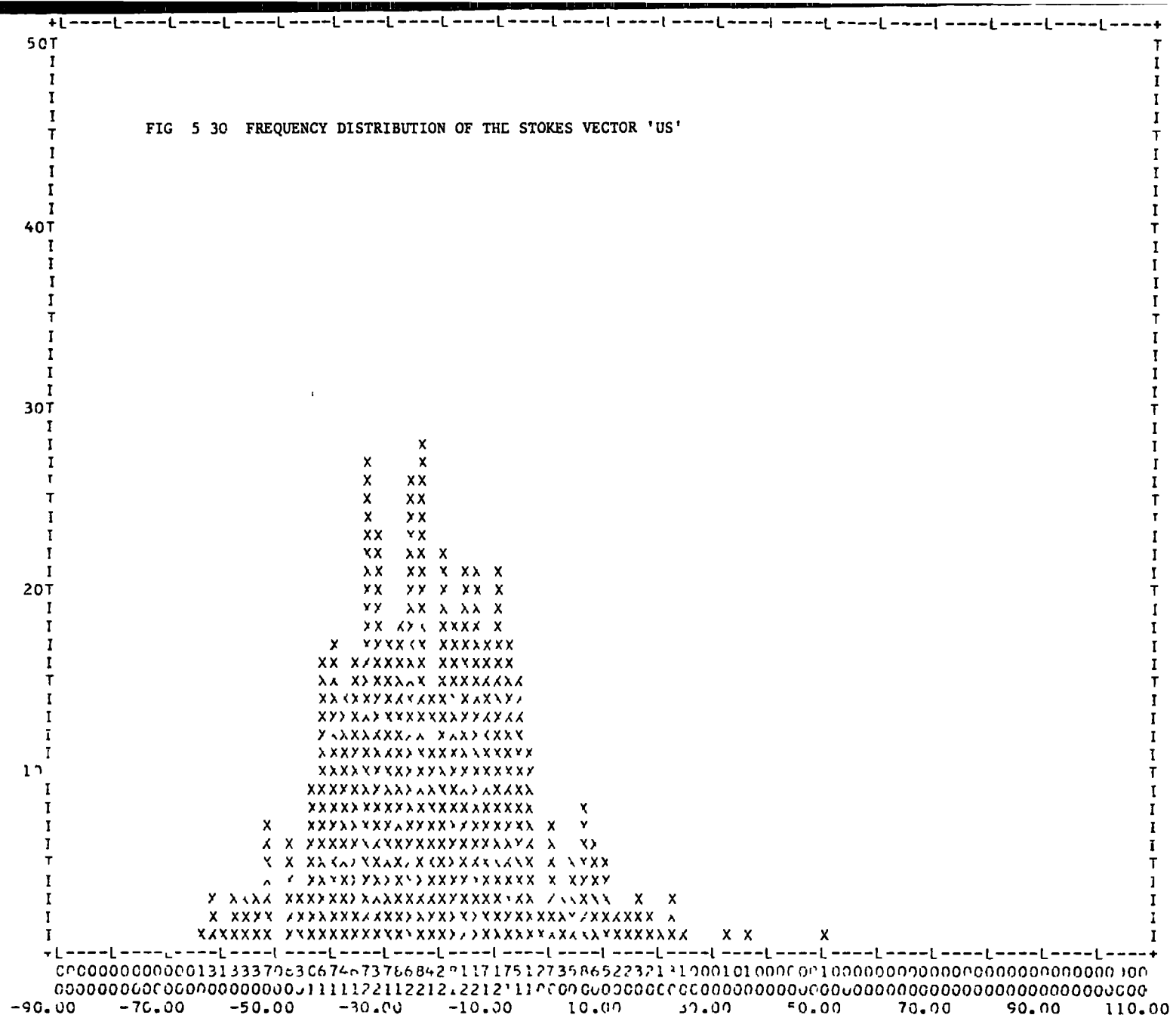
FIG 5 30 FREQUENCY DISTRIBUTION OF THE STOKES VECTOR 'US'
FREQUFNCY
50
40
30
20
10
-90.00
-70.00
-50.00
-30.00
-10.00
10.00
30.00
50.00
70.00
90.00
110.00
U FOR SKY
US
PLOT NUMBER 5

FIG 5 31 THE POLARISATION MAP OF THE LIGHT EMANATING FROM M82

points to be plotted, so that only those for which the galactic signal was at least 15% of the sky signal to be subtracted, made it possible to plot the resultant map (figure 5.31), without the set of irregular 'statistical' vectors around the outside. The limiting intensity of approximately 15% was found by trial and error.

5.12 Transformation to an Absolute Co-ordinate System

The two halves of the map, shown in figures 5.17 and 5.18 are aligned by eye, because each half is plotted in terms of the different arbitrary X Y co-ordinate systems defined by the digitisation procedures. It is therefore necessary, to transform each half, so that the entire map is plotted in the usual absolute co-ordinate system of right ascension and declination.

Using only the central part of the telescope image, at f/13.5 focus, plane geometry is sufficiently accurate to describe the transformation from the X-Y to RA(α) and Dec(δ) systems, which is therefore given by,

$$\alpha = a = b\,x + c\,y \qquad 5.8$$

$$\delta = d + e\,x + f\,y \qquad 5.9$$

where X and Y are the digital matrix co-ordinates of a 120 micron squared area, and α and δ are the absolute co-ordinates for the same region.

A series of fiducial points, where (α, δ, X, Y) are known for several locations on the matrices, are required to solve for the co-efficients (a-f) for each of the sets of matrices (S1T - S4T, S5T - S8T). The stars in the field of view which again provide the obvious reference points are uncatalogued with the exception of HD + 70^{o} 587, the bright

star to the South West of the galaxy. The absolute co-ordinates of the remaining stars were obtained by measurement from a Palomar plate. An astrometric machine at the Royal Greenwich Observatory was used, which automatically reads off the absolute co-ordinates of any point on an electronograph, once it has been initialised by supplying a series of locations corresponding to the co-ordinates of catalogued stars.

The least squares minimisation procedure in section 5.5.2. was used to determine the coefficients for each half of the map, and those obtained for the matrices (S1T - S5T) are listed in Table 5 together with calculated and experimental values for the absolute co-ordinates. The agreement is good, and from a visual inspection the trarsformation to R.A. and Dec. appears to be accurate to approximately 1 arc second. The absolute co-ordinates of the stars, are measured in seconds of arc from an arbitrary origin which was chosen for convenience at 69^{o} 50.00' in declination and 9 hrs 51.00 minutes in right ascension.

The X Y location of each polarisation point was transformed to the absolute scale, using the appropriate coefficients, and the complete map replotted in plate 8, where the map has been superimposed upon an H_{α} Palomar plate of M82. As is normal, the right ascension scale has been multiplied by a cos (declination) factor, so that the plot takes on the appearance of the image of the galaxy on the sky. The positions of the fiducial stars are shown which were used for the plate alignment, and transformation to the absolute co-ordinate scale. The centre of the symmetric pattern formed by the polarisation vectors, the determination of which will be discussed in Chapter 7, is also shown

COEFFICIENTS

a = -21.184 b = 4.5630 c = -0.0412

d = -22.2829 e = 0.06783 f = 1.5676

STAR	X	Y	R.A.	Dec.	R.A.^{t}	Dec.^{t}
1	51.30	96.60	209.14	132.61	208.92	132.62
3	130.60	247.70	565.60	374.81	564.55	374.86
7	302.92	213.50	1351.89	332.96	1352.17	332.94
9	61.03	224.53	247.10	333.88	248.06	333.82

TABLE 5. TRANSFORMATION COEFFICIENTS TO R A. AND DEC

PLATE 8

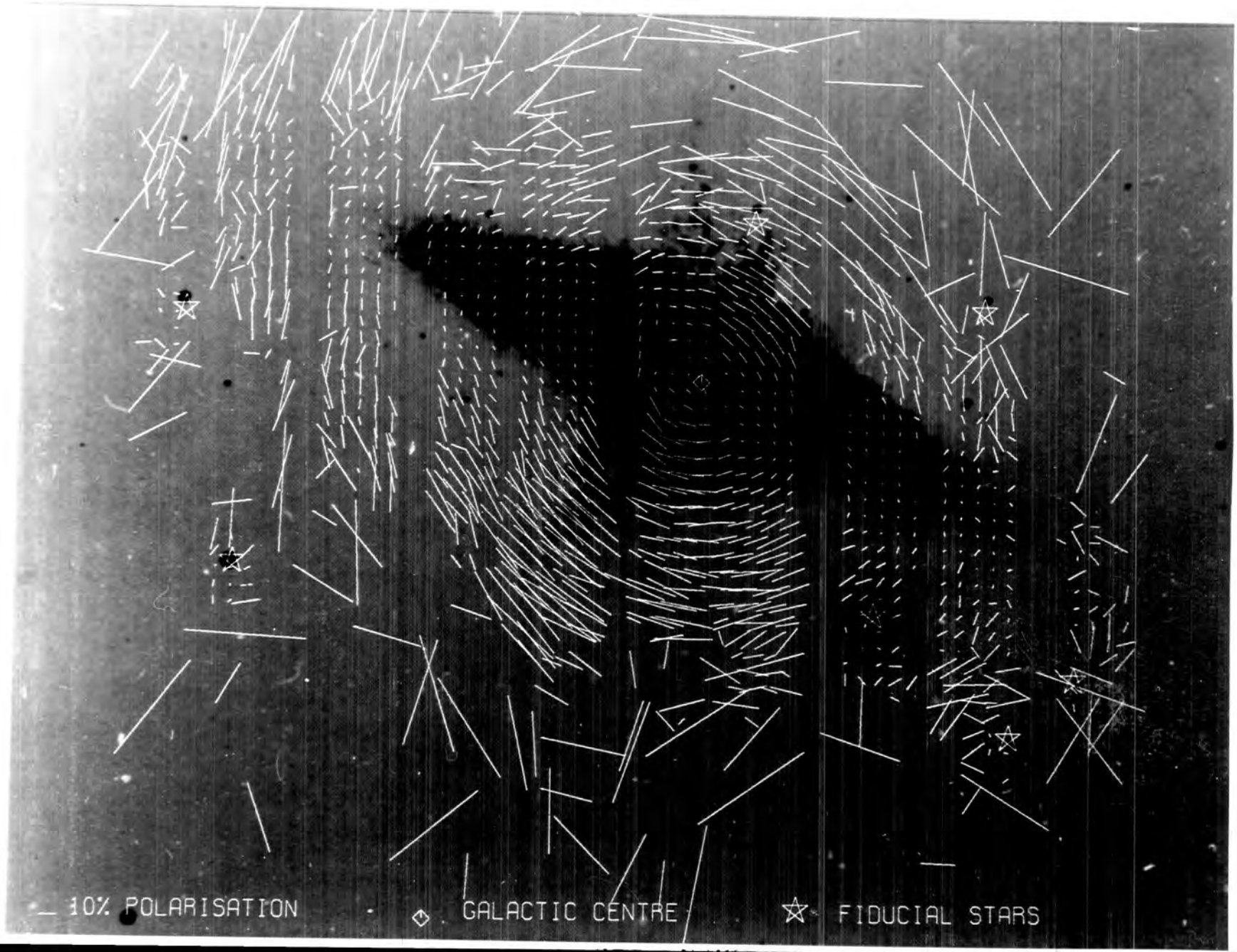

The fact that the polarisation vectors flow smoothly from one gridwidth to the next, (where the determinations are from different electronographs, and are therefore completely independent), is an important test of the reduction technique.

5.13 General Features of the Map

Plate 8 clearly shows how the polarisation pattern divides the galaxy into a region of low and irregular polarisation corresponding to the disk, and a region of higher polarisation corresponding to the halo of the galaxy, where the vectors form a regular pattern around the central region of the disk. Detailed discussion of the features of the map, and their implications, will be discussed in Chapter 7. The present concern is simply to be sure that the technique has successfully reproduced the pattern obtained by other workers.

A quantitative comparison with previous measurements is made in section 6 3.2. For visual comparison however, a map showing results obtained by Elvius (1963, 1969), and Visvanathan and Sandage (1969, 1972), are shown in figure 5 32. The map, obtained by conventional photo-electric measurements, clearly shows the same general features as that of plate 8, and is at least visual confirmation that the electronographic-computer technique, has successfully reproduced the earlier results.

A feature of the two maps, is that the photo-electric measurements have been made further out into the halo (i e where the brightness ratio of sky to galaxy is large) than our measurements. Some of the faintest photo-electric determinations are for a galaxy/sky signal of approximately 5%, whereas the present map terminates at a corresponding value of 15%.

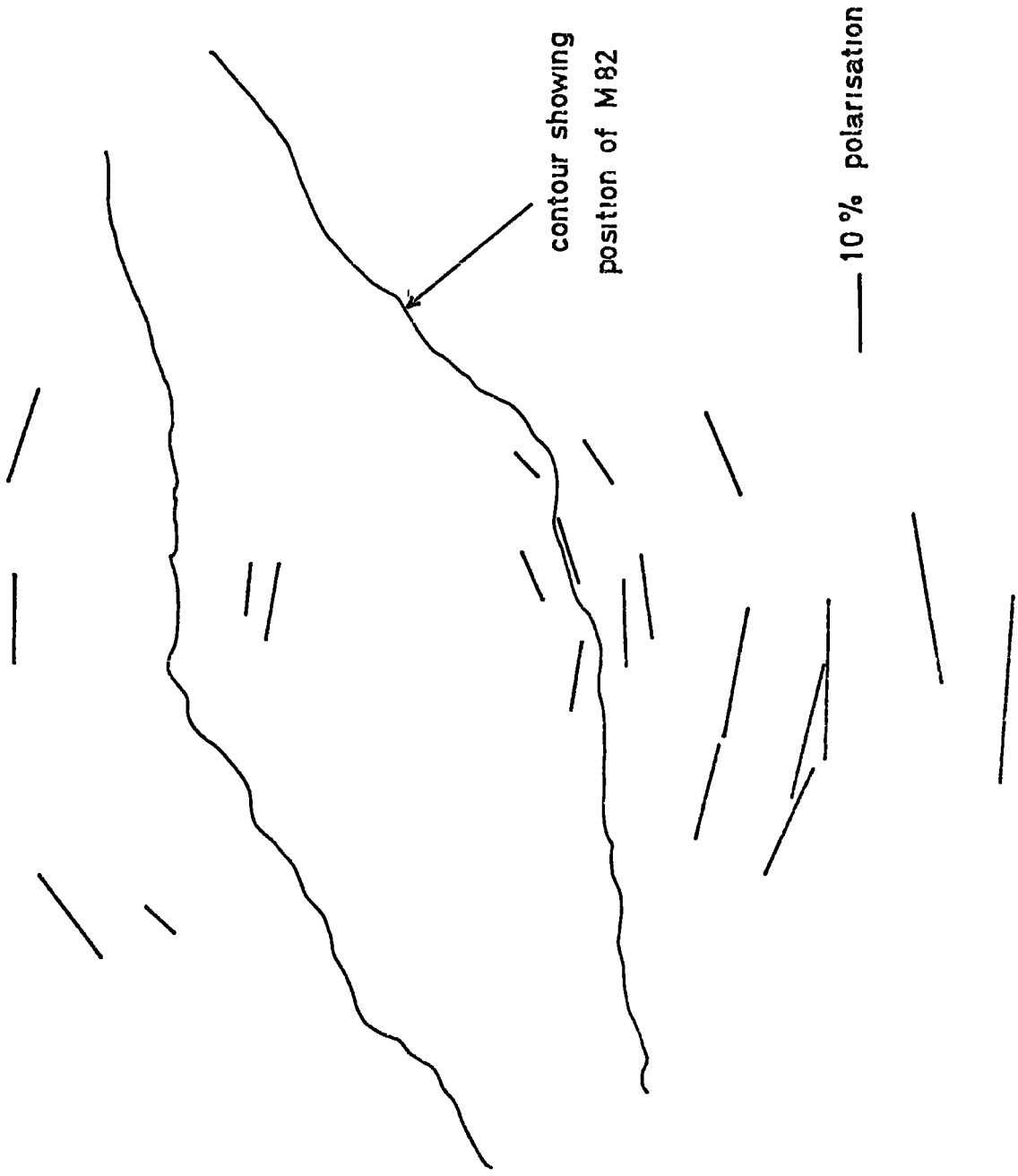

FIG 5 32 PHOTOELECTRIC POLARISATION MEASUREMENTS OF M82

The spatial resolution for the new technique described, is 3 to 5 times finer than that used in the photo-electric measurements, and this accounts, at least partly for the loss in limiting magnitude. Also, the areas in which the galactic signal is becoming increasingly faint, correspond to the innermost boundary of the locations from which the Stokes parameters of the sky were evaluated These parameters are therefore likely to be contaminated with the outer regions of the M82 halo, and their subtraction from the total Stokes vectors near this region will yield a meaningless result

A final feature of the map, is the occasional occurrence of a randomly orientated vector, among the otherwise smooth pattern. This is attributed to an area for which the quality control has failed to extract some density pixels which are unrepresentative of the real polarised light signal, and are probably caused by a scratch or speck of dust.

The map produced, using the basic reduction technique, shows approximately 10 times as many points as previously observed, with a spatial resolution three to five times finer. This is achieved using a single series of observations needed to obtain the eight electronographic plates, rather than the mass of independent observations needed for the corresponding photo-electric measurements. The initial goal, to produce a high resolution polarisation map of low surface brightness nebulous objects, using an image recording technique, has therefore been successfully achieved

In the next chapter, attempts to improve the quality of the already superior map are described, together with an investigation of the accuracy associated with the electronographic measurements.

CHAPTER 6

THE COMPUTER REDUCTION TECHNIQUE II

6.1 A Low Resolution Map

Although the map produced almost extends to the limit defined by the method of sky subtraction, a revised set of programs were written to produce a map with a spatial distribution of points nearer to that of the photo-electric measurements. Instead of adding 25 pixels to form an integrated area, corresponding to the 8 arc seconds squared, 81 pixels were summed to form an area of 14 arc seconds squared. The net effect of taking the mean density from 81 measurements rather than 25 is to reduce the fluctuations involved. With the larger individual area, only 3 points across a grid, and 35 in length could be taken, for each of the measurements to be independent.

The modified programs were run in a similar manner to those described for high resolution, and the map produced is shown in plate 9. The map has exactly the same form as that of plate 8, but it extends slightly farther out into the halo than its highly resolved counterpart. Extension to even larger integration areas for the M82 plates reduced here, is not practicable because of the sky subtraction problem If further electronographs were taken however, with the disk of the galaxy at the bottom of the image rather than in the centre, it would be possible to access parts of the night sky twice as far away from M82. The night sky subtraction problem would then disappear, and a low spatial resolution would make it possible to reach even lower signal/sky ratios than the 5% achieved in photo-electric measurements.

The second noticeable feature of plate 9, is the increased smoothness

PLATE 9

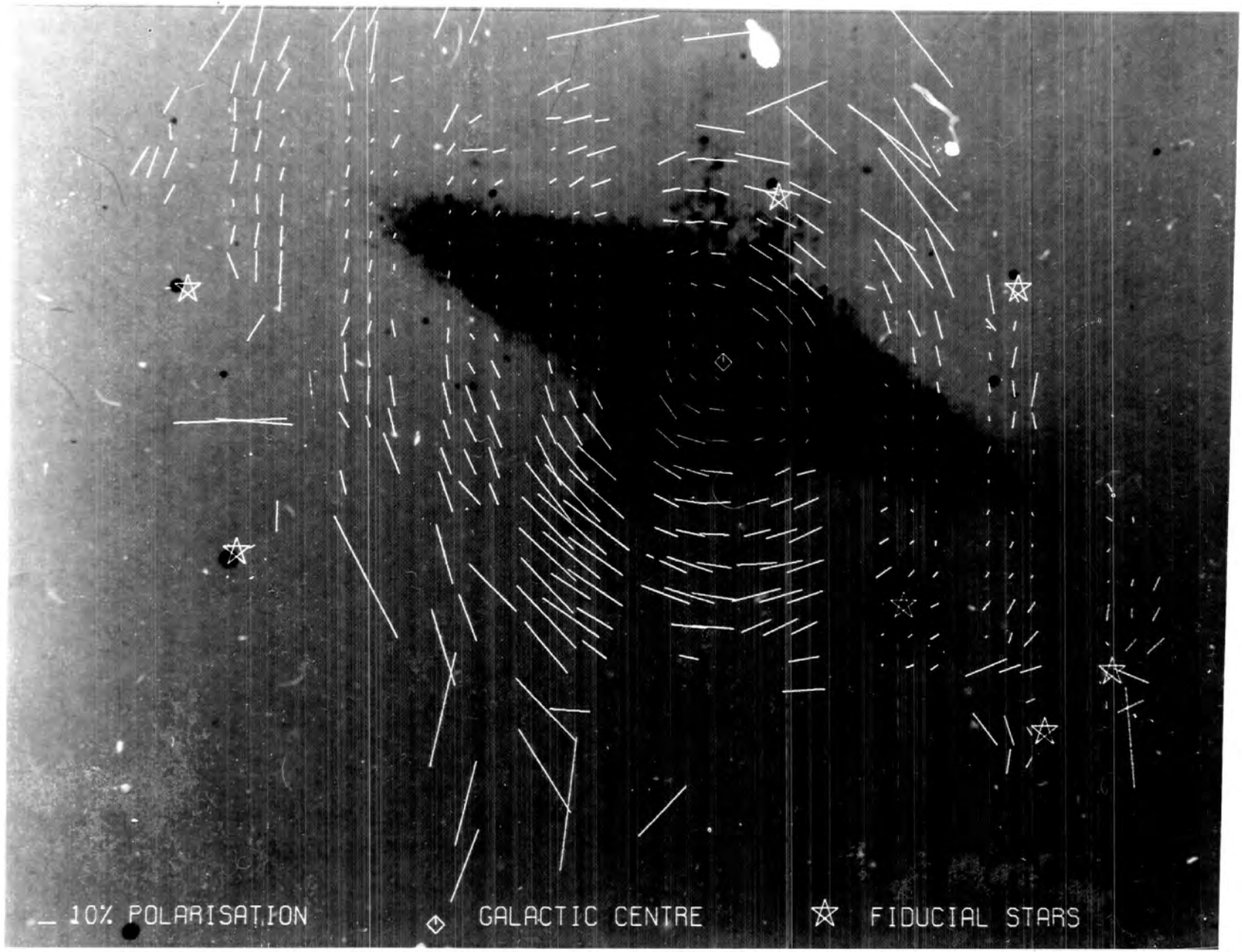

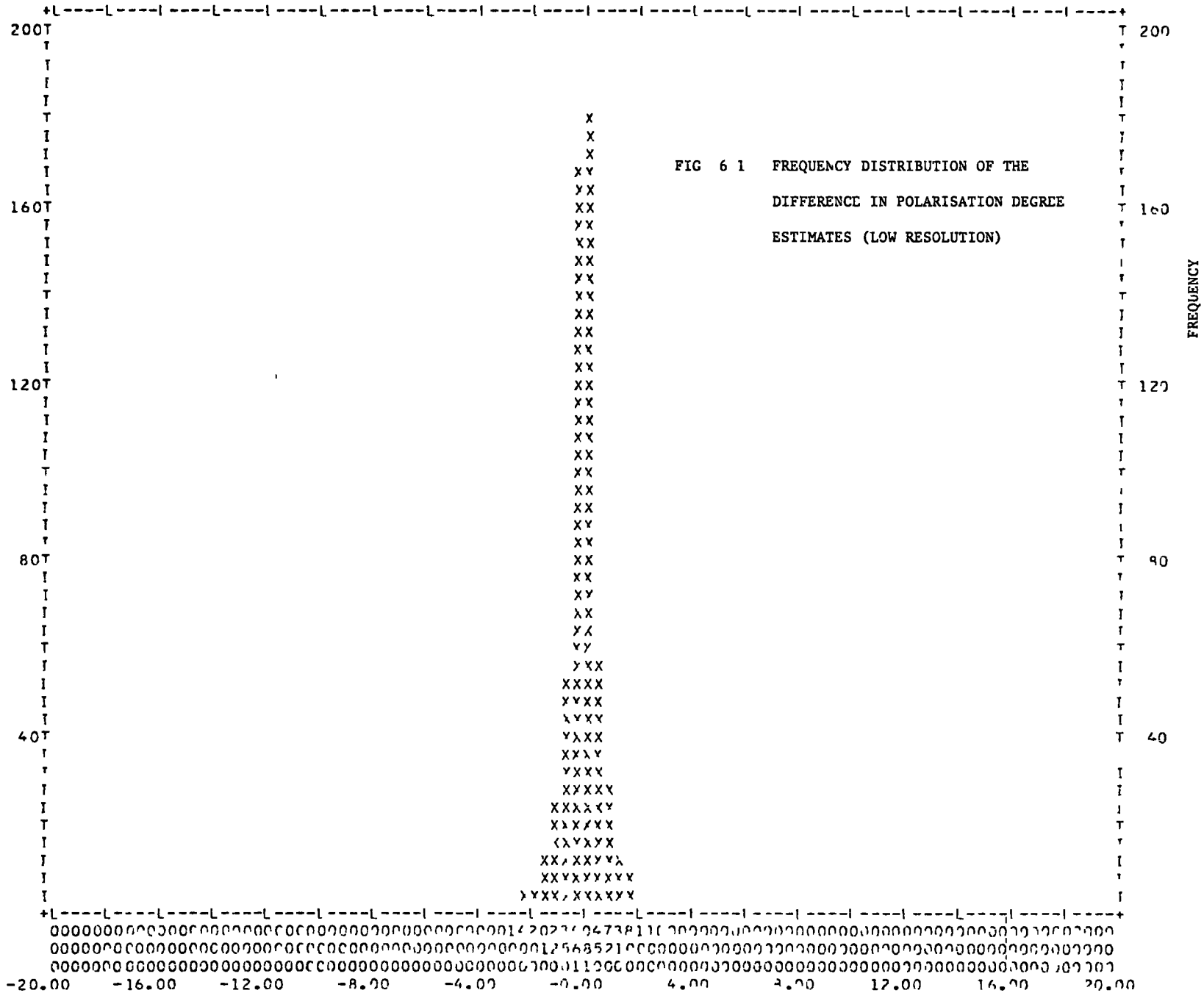

FIG 6 1 FREQUENCY DISTRIBUTION OF THE DIFFERENCE IN POLARISATION DEGREE ESTIMATES (LOW RESOLUTION)

PLOT PHASES 2

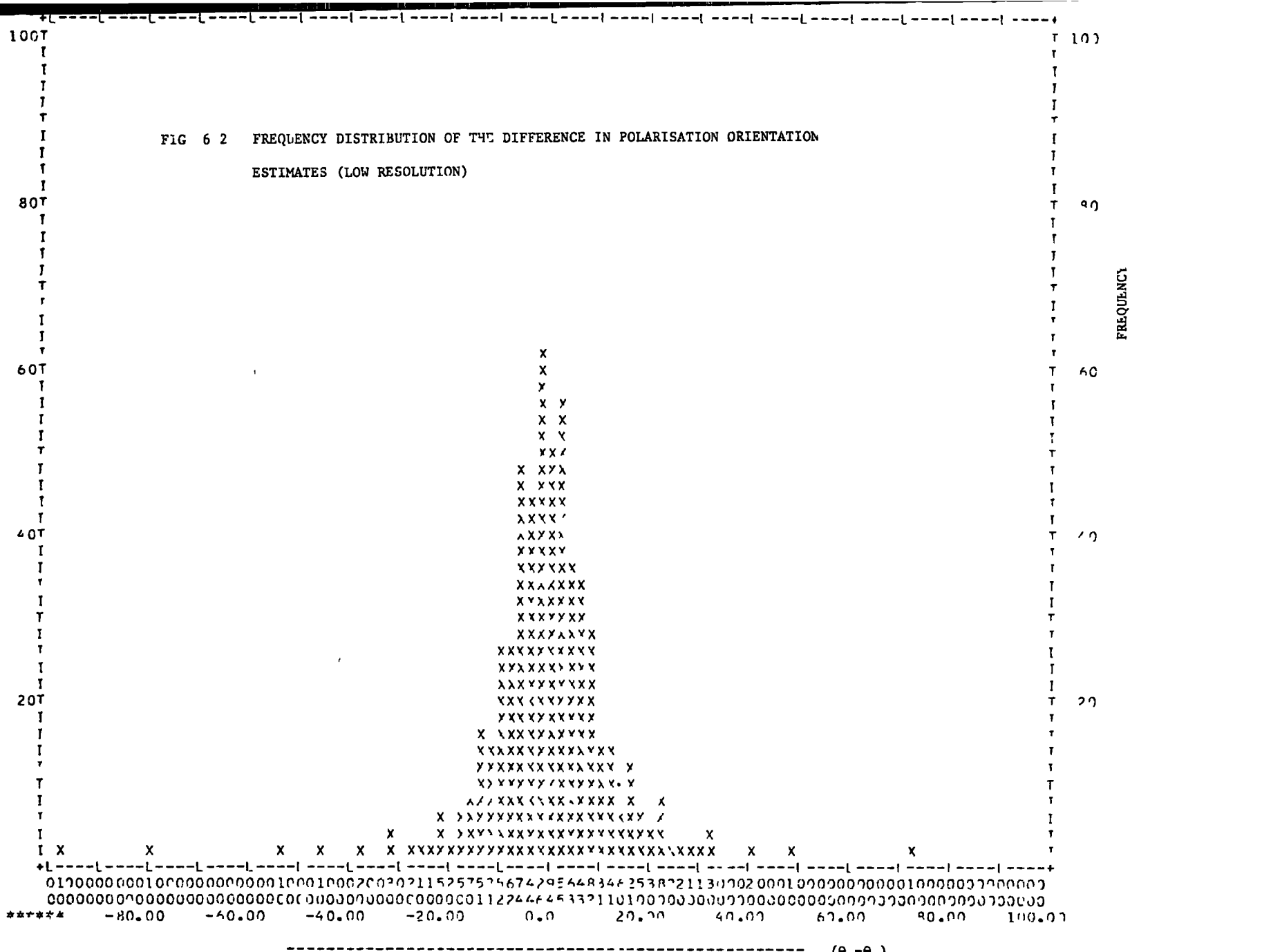

FIG 6 2 FREQUENCY DISTRIBUTION OF THE DIFFERENCE IN POLARISATION ORIENTATION ESTIMATES (LOW RESOLUTION)

ANG1-ANG2

PLOT NUMBER 7

of the pattern due to the damping of fluctuations by using a larger integration area. This point is illustrated in figures 6.1 and 6.2, which show that the frequency distributions of '$p_1 - p_2$' and '$\theta_1 - \theta_2$' for the low resolution map, are considerably narrower than the corresponding plots shown in figures 5.26 and 5.27.

This decrease in the uncertainty associated with a particular polarisation point, has only been achieved by a sacrifice in the total number of points and the spatial resolution, and is therefore not as advantageous as might first appear

6.2 Computer Smoothing of the Matrices

6 2.1. Introduction

A second approach to improving the quality of the final map, without losing the high resolution properties, is to examine the basic digital data, and try to identify, and replace any incorrect density values prior to reduction. The underlying principle upon which smoothing methods depend, is that providing the pixel size of the digitisation is less than the seeing disk, then the intensity profile in a series of neighbouring bins, should form a smooth surface and be devoid of discontinuities. Unfortunately, this criterion is only partially met with the M82 data, and therefore the disk area, with its series of irregular dust lanes crossing the bright central region gives rise to fairly acute discontinuities. The halo area, however, which is the region of primary interest for polarisation studies, conforms well to the necessary smoothing conditions. It was therefore necessary to employ a smoothing method which could be applied to the required area of the plates only and leave the other regions in their natural form.

6.2.2. Smoothing Methods

Smoothing of digital data can be either 1 dimensional, in which case each row or column of the matrix is treated separately, and a form of curve fitted to the data points, or 2 dimensional, when a surface is used to represent the digital array. The M82 electronographs are best suited to one dimensional smoothing, taking each column of the matrix in turn, because of the discontinuity in the X direction formed by the overlapping images of the grids.

Smoothing methods fall into two main categories. The standard approach, is to consider the entire 1 dimensional array to be smoothed, and redescribe the data curve by a series of amplitudes corresponding to the fourier transform, i.e.

$$a(k) = \sum_{i=1}^{i=n} f_i(x).e^{-ikx} \qquad 6.1$$

Equation 6.1 shows the expression for the fourier amplitudes for a one dimensional array 'X' of n data points having the value $f_i(x)$ stored in each bin. The wave number 'k', is evaluated for the range

$$2\pi \leq k \leq {}^{2\pi}/_{n} \qquad 6.2$$

corresponding to wavelengths of the spacing of the data points and the entire length of the array

The amplitudes for large k values are caused by any sharp discontinuities in the data, which have therefore been separated by the large scale smooth component, described by amplitudes for smaller k values. The smoothed data is then reformed from the required amplitudes using the property that the fourier transform of a fourier transform results

in the original curve, i.e.

$$f_1(x) = \sum_{k=2\pi/n}^{k=k(\text{cut off})} e^{ikx} \cdot a(k) \qquad 6.3$$

Although elegant in concept, the Fourier method suffers the limitations that to be fully utilised, the one dimensional array should be considered as a whole, and secondly, if a discontinuity of greater magnitude than the remainder of the relatively smooth array exists, the Fourier transform describes the discontinuity in preference to the bulk of smooth data. The images of bright stars, as well as that of the nuclear regions of M82, form such discontinuities, and make the standard Fourier smoothing technique difficult to apply to the plates in question.

The second type of approach, which is more diverse in nature, is simply to consider each pixel in turn with those in close proximity to the one in question. Tests are made, to see if the value under observation fits in well with the pattern of the surrounding area, and then, if necessary, the value is replaced by an interpolated value from the surroundings. As the pixels are treated individually, this method has the advantage, that any area of known discontinuity can be omitted from the smoothing procedure, and left in its natural state.

The main pitfall of this type of smoothing procedure is that if a correct density under consideration, is surrounded by one or more highly erroneous values, then a simple comparison test of the density, with its neighbours, will show the correct point to be faulty. The interpolation used to replace this density, will then give a value which is at least partly contaminated with the incorrect values

6.2.3. The One Dimensional Smoothing Technique

Because of the grid discontinuities, a one dimensional smoothing technique was developed which read one column of the matrix at a time, and sequentially compared each of the elements of the array with its nearest neighbours. Elements were replaced where necessary, until the entire column of 384 elements had been subjected to the smoothing procedure. This was then repeated for each of the 384 columns forming the matrix.

The method is illustrated in figure 6.3, which shows a sample of a column for a matrix before and after the smoothing procedure has been applied. The sample has purposefully been chosen with two incorrect density values (probably caused by a speck of dust), to show that the two erroneous values have been replaced, while the neighbouring values are left in their natural state.

When a particular pixel is under consideration, the four densities at each side are first investigated to see if there is a large density gradient in the vicinity of the point. If this is so, the pixel is situated near a star image, or the central region of the disk, and the program immediately progresses on to the next pixel, until the test reveals that a region of slowly varying density has been reached. In this way regions of erratic intensity profile are automatically omitted from the smoothing procedure.

Linear interpolations from the three nearest pairs of points at each side of the pixel in question are taken, and each compared with the actual value. If any of the interpolated values disagree with the stored value by more than a set datum level, then the point is

"Y" coord.		"Smoothed density"	"Original density"
1	0	43	43
2	0	43	43
3	0	43	43
4	0	43	43
5	0	43	43
6	0	43	43
7	0	44	44
8	0	45	45
9	0	44	44
10	0	43	43
11	0	43	43
12	0	43	43
13	0	46	46
14	0 Replaced Density	49	49
15	0	52	52
16	0	51	51
17	0	53	53
18	0	53	53
19	X 0	53	72
20	X 0	53	73
21	0	54	54
22	0	53	53
23	0	53	53
24	0	53	53
25	0	53	53
26	X 0	53	64
27	0	52	52
28	0	53	53
29	0	54	54
30	0	53	53
31	0	53	53
32	0	53	53
33	0	57	57
34	0	54	54
35	0	55	55
36	0	54	54
37	0	55	55
38	0	53	53
39	0	53	53
40	0	57	57
41	0	53	53
42	0	55	55
43	0	53	53
44	0	55	55
45	0	56	56
46	0	54	54
47	0	53	53
48	0	57	57
49	0	57	57
50	0	56	56
51	0	57	57
53	0	54	54
54	0	54	54

FIG. 6 3 A SMOOTHED TRACE

considered faulty and needs replacement. It is at this stage, that the difference between a good point surrounded by an erroneous one, and vice versa can be recognised, and is illustrated in figure 6.4, which follows through the procedure for the four points of interest in figure 6 3. The percentage differences between the real and interpolated values always have at least one value for an incorrect point which is approximately twice as large as any of those for a correct point. If the datum level for replacement could be set between the two values, then the incorrect value would be replaced, and the correct value left untouched

The solution, is therefore to have an iterative procedure, in which the column is repeatedly smoothed with a progressively smaller datum, until the dispersion of a particular set of points about the curve is reduced to the desired level. In this way, a good point is never contaminated by the presence of an erroneous one nearby.

Once a particular pixel has been proved faulty, a parabola is fitted to the surrounding eight points, and the interpolated value used to replace the incorrect density If, as in the case shown in figure 6.3, there is more than one faulty density in the neighbourhood, the fit is slightly weighted with the adjacent erroneous value, when the parabola is fitted to obtain the 'new' density at point 19 on the trace. The replacement is therefore a better estimate, rather than the correct value When the datum level is sufficiently reduced, during one of the following iterations, the point is again replaced, by a progressively more correct value. After the total of 6 iterations performed, the point will have assumed the correct value. The datum level for pixel replace-

					X	X				
			X	X			X	X	X	X
	X	X								
Density	52	51	53	53	72	73	54	53	53	53
Y Coordinate	15	16	17	18	19	20	21	22	23	24

Point under observation.		Interpolated Estimates			Fractional diff. with real value.		
Y coord n	density d	$E_1=\frac{d_{n-1}+d_{n+1}}{2}$	$E_2=\frac{d_{n-2}+d_{n+2}}{2}$	$E_3=\frac{d_{n-3}+d_{n+3}}{2}$	$\frac{E_1-d_n}{E_1}$	$\frac{E_2-d_n}{E_2}$	$\frac{E_3-d_n}{E_3}$
18	53	63	62	53	0.16	0.15	0.0
19	72	63	54	53	0.14	0.33	0.36
20	73	63	53	53	0.16	0.38	0.38
21	54	63	63	53	0.14	0.14	0.01

FIG. 6 4. DETERMINING ERRONLOUS DENSITY VALUES

ment was set at 4% for the final iteration, roughly corresponding to the fluctuations due to the photocathode sensitivity.

6.2.4. The Smoothed Map

The set of eight matrices were computer smoothed using the method described in the previous section, and then the entire reduction procedure rerun to result in the map shown in plate 10. The plot, which shows all the expected features, appears to combine the high resolution of the 8 arc second squared map shown in plate 8, with the ordered pattern of the low resolution map. The histograms shown in figures 6.5 and 6.6, also indicate that the average uncertainties associated with a single point have been reduced by the application of the smoothing procedure.

6.2.5. Discussion

Although these attempts to squeeze the best possible map from the data have been partially successful, the full benefit has not been reaped because of the difficulties with the sky subtraction and the effect of non-uniformities in the photo-cathode sensitivity. When more electronographs have been taken, and further investigation to resolve these difficulties have been carried out, these important refinements to the techniques will perhaps result in a substantial increase in the quality of a polarisation map

6.3 Comparison with Previous Measurements

6 3.1. Introduction

Because of the difficulties of recording and extracting low light signals on photographic plates, most studies have used photo-electric methods to determine the surface polarisation of nebulous objects.

PLATE 10

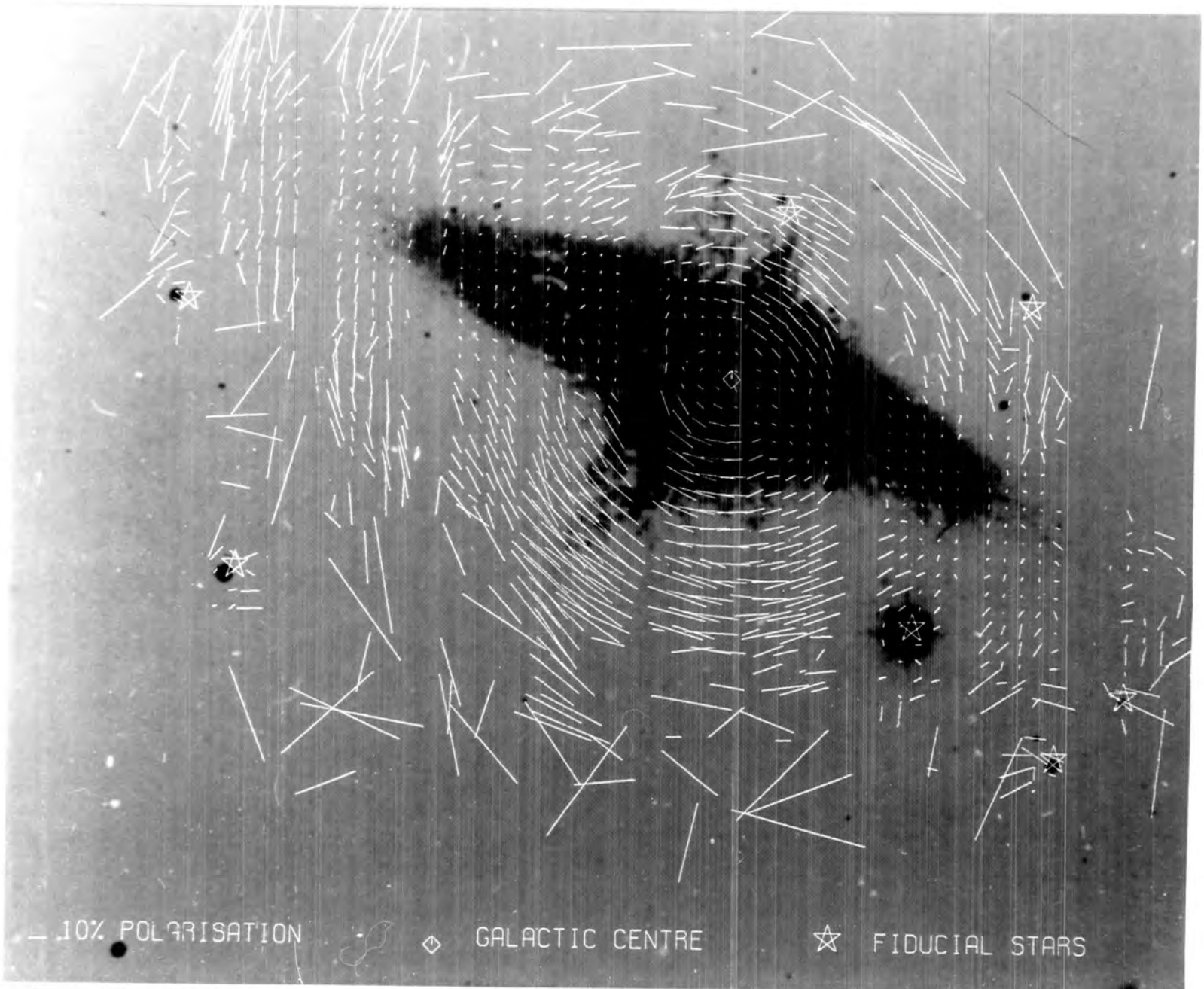

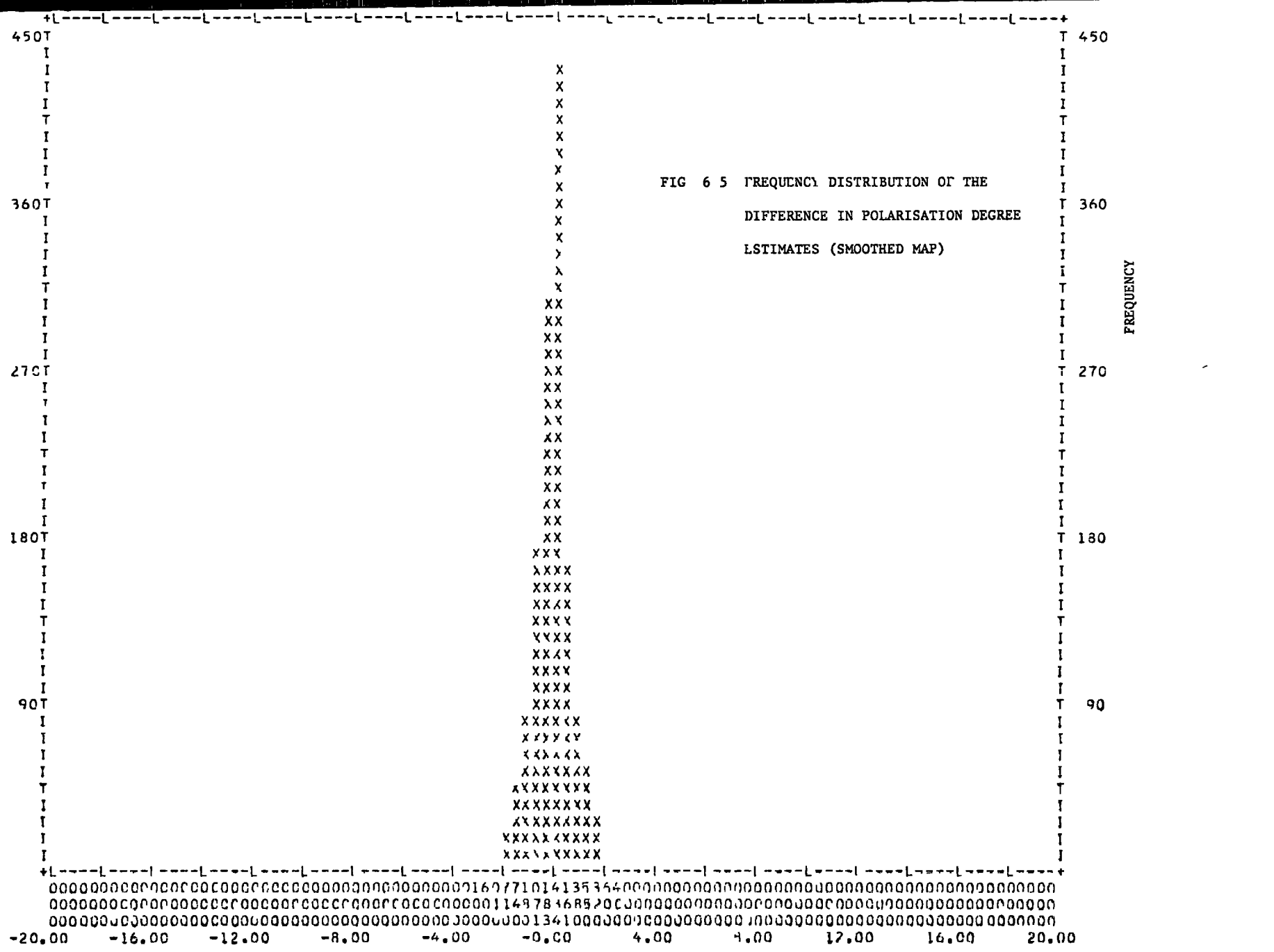

FIG 6 5 FREQUENCY DISTRIBUTION OF THE DIFFERENCE IN POLARISATION DEGREE ESTIMATES (SMOOTHED MAP)

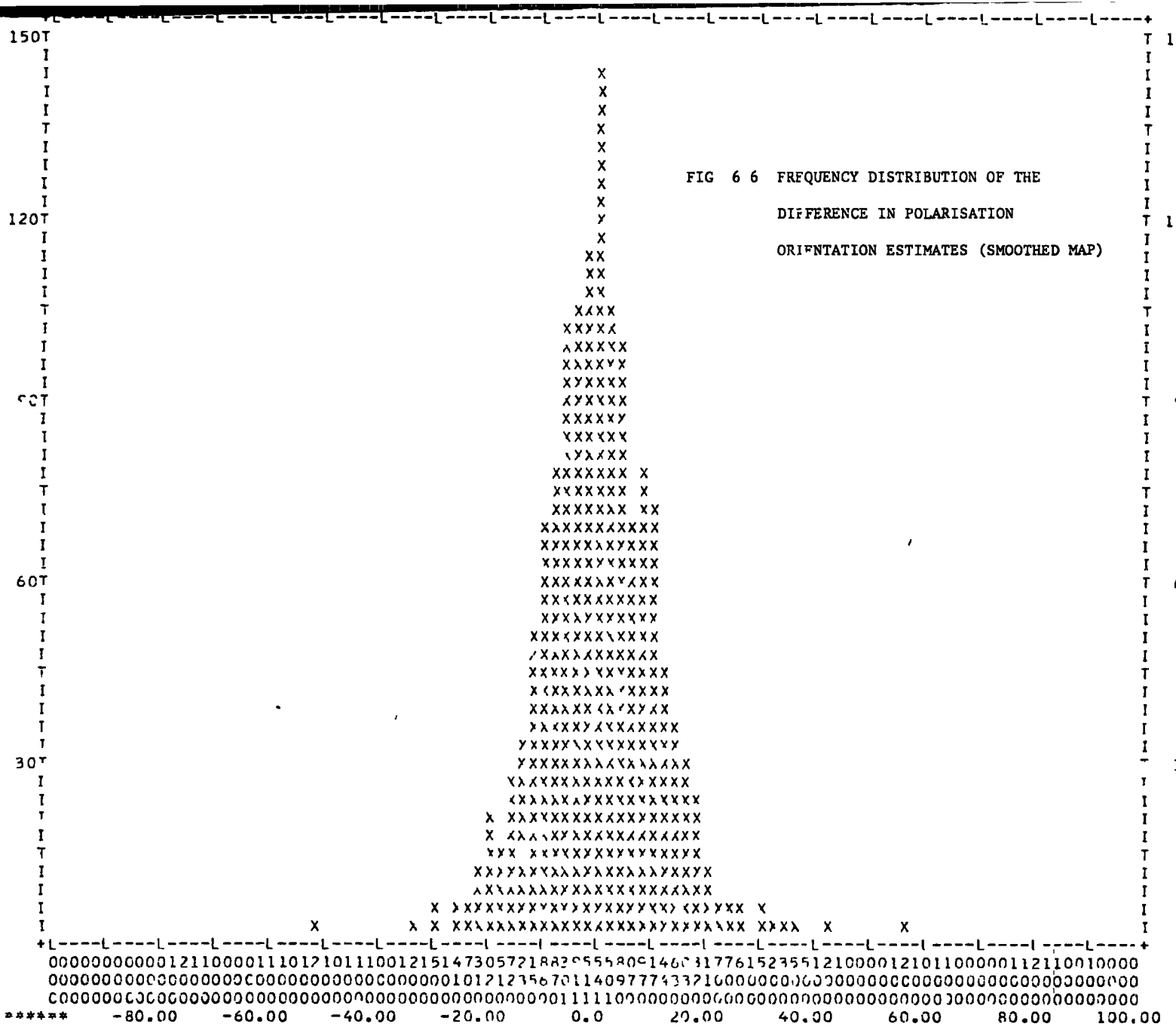

FIG 6 6 FREQUENCY DISTRIBUTION OF THE DIFFERENCE IN POLARISATION ORIENTATION ESTIMATES (SMOOTHED MAP)

PLOT NUMBER 7

The technique is simply to record the intensity of radiation entering the equipment aperture, through a polarising filter at various orientations. A set of values (i_1 - i_4) are recorded as was described for the simple method of Chapter 1 The resolution of the apparatus, is determined by the size of the entrance aperture, and the location of the area to be studied is found by offsetting from a reference point such as a nearby star. With large computer controlled telescopes, this is no real disadvantage. The technique does have the severe limitation, that only one area can be studied at a time, which means that a detailed study of the change of polarisation with location on an extended object, is a long tedious procedure and is therefore open to error.

Although the advent of the electron camera, with its inbuilt calibration, and large dynamic range advantages over the conventional plate, have heralded the way to 'imaging' forms of polarisation studies, the difficulties with image registration on the plates, has only been solved by the use of a sophisticated digital computer reduction technique.

6.3.2. Photo-Electric Measurements

The map shown in figure 5.32 shows most of the previous determinations of the surface polarisation of M82, (in the B waveband of the UBV system), and is a mixture of measurements taken at the Steward 80" reflector by Elvius (1963, 1969), and those of Visvanathan and Sandage (1969, 1972) on the 200" Palomar telescope. Both series of measurements were made on much larger aperture telescopes than that of the modest 1 metre telescope of the Wise Observatory, which makes the present determination all the more impressive.

A comparison with the earlier work is made in figures 6.7 and 6.8, where the degree of the polarisation, and the preferred direction of vibration for each of the regions studied photo-electrically, are plotted against the corresponding values from the present work. Each point is weighted with the polarised intensity for that area (∿ uncertainty), and this weight is shown by the symbols (1, 2 ... 9, A, ... Z,+). The apertures used for the earlier work, are 3 to 5 times larger than the present 8 arc second squared determination. In order to make an accurate comparison, our Stokes parameters have been integrated to correspond to the apertures used previously.

The two plots, which both yield straight lines at 45°, with only a relatively small amount of scatter, show that the two series of measurements correlate extremely well. In figure 6.7, the points are uniformly distributed about the theoretical line, which implies that there is no systematic error in the measurement of polarisation angle. The internal uncertainties, which are investigated by examination of the two estimates obtained for each integrated area, are therefore representative of the total uncertainty associated with a particular measurement.

In figure 6.8, however, there is some evidence, that the points form a straight line, which is parallel to, but slightly above the expected straight line through the origin. If the photo-electric measurements are considered to be the accurate values, the present results seem to systematically underestimate the degree of the polarisation by approximately 1.5%. Investigation of this problem, reveals two possible contributing factors

The PDS machine, which was supposed to record a digital value

ANGLE

FIG 6 7 PHOTOELECTRIC POLARISATION DEGREE ESTIMATES v

DURHAM POLARISATION DEGREE ESTIMATES

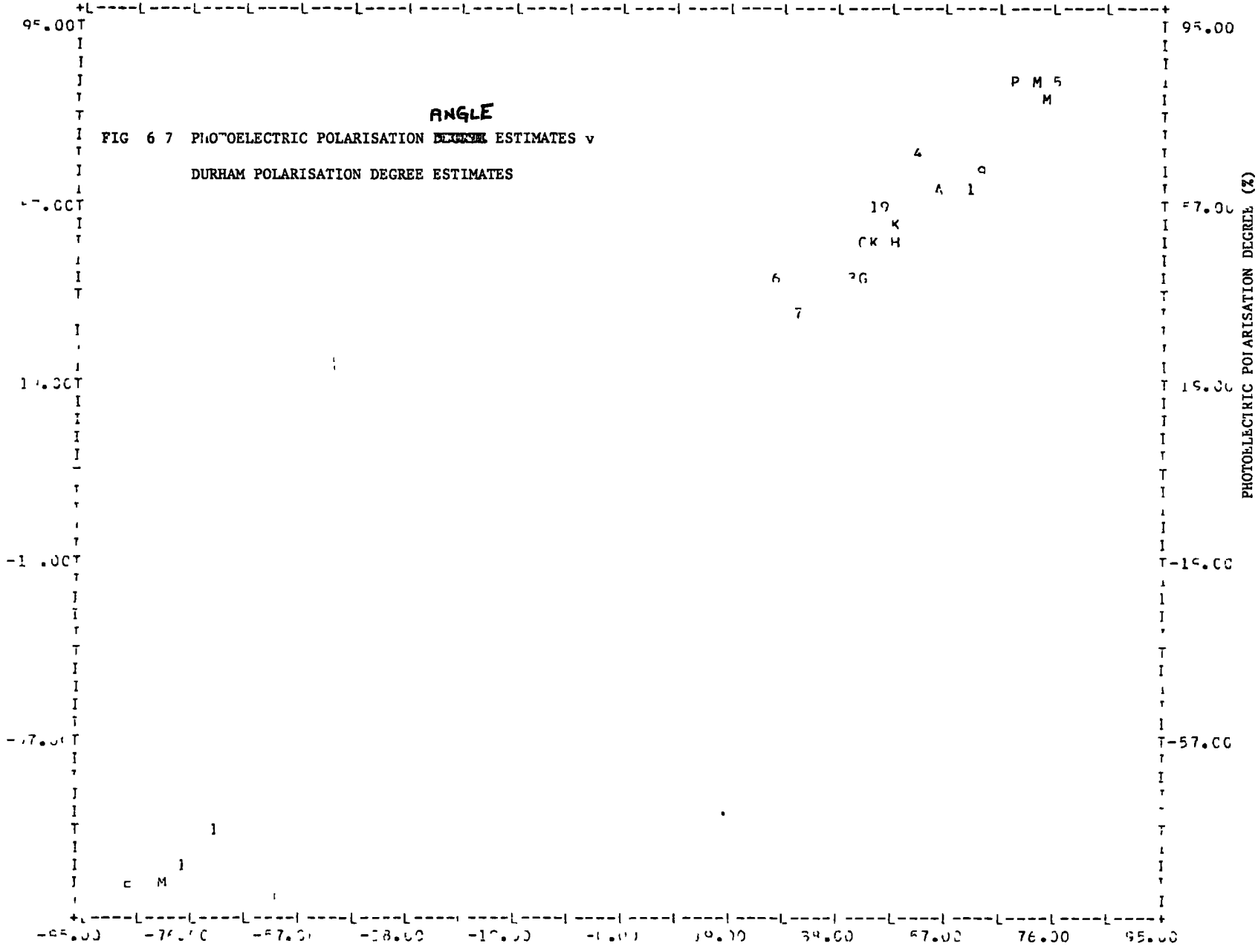

I POL ANGLE(P/C) V POL ANGLE(FIGG-APHIC) I

INSIDE 247 OUT LOW 0 OUT HIGH 0 TOTAL 247

DPLOT NUMBER 1

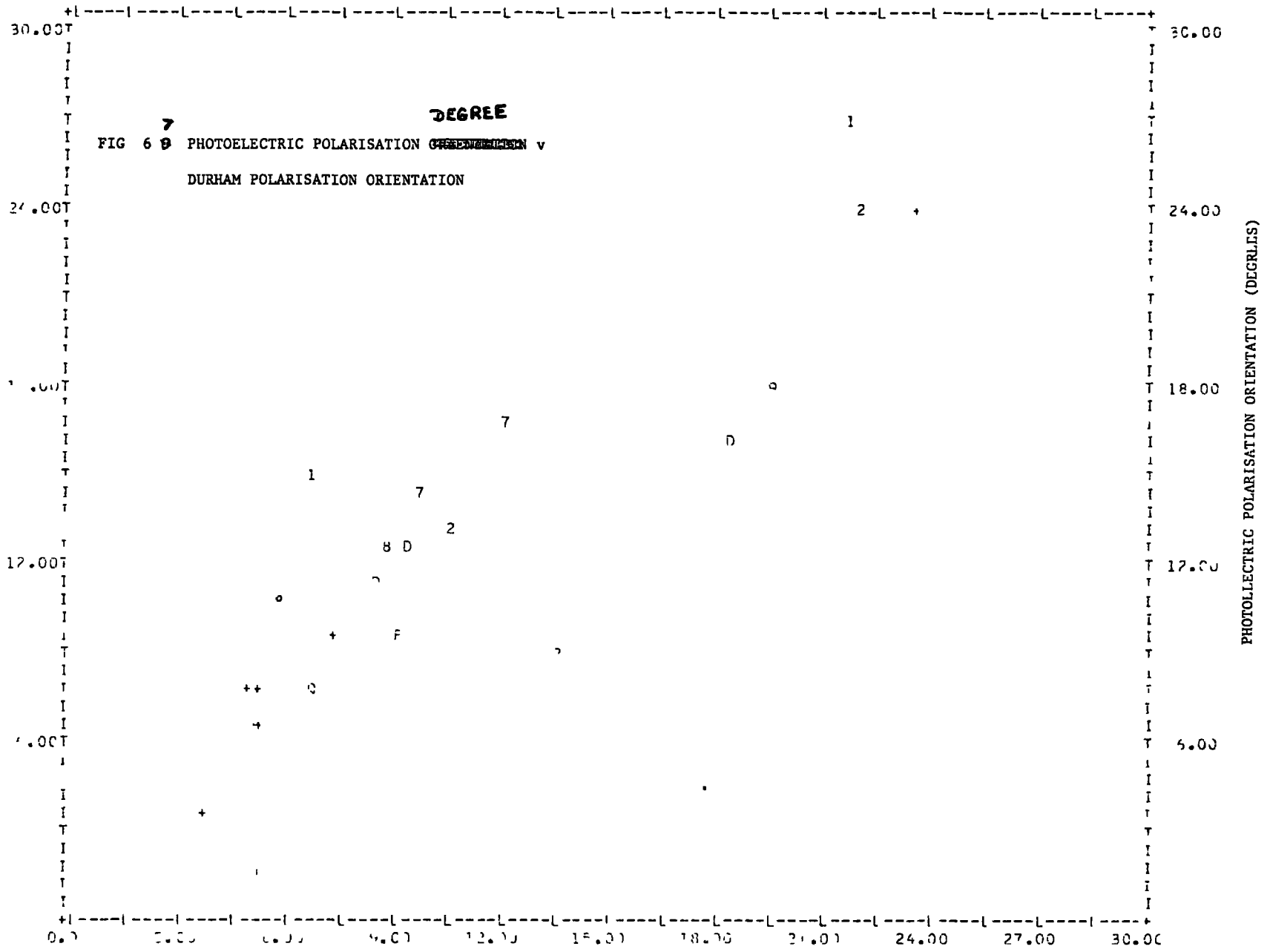
DEGREE
FIG 6 PHOTOELECTRIC POLARISATION
DURHAM POLARISATION ORIENTATION
30.00
24.00
18.00
12.00
6.00
0.0
3.00
6.00
9.00
12.00
15.00
18.00
21.00
24.00
27.00
30.00
PHOTOLLECTRIC POLARISATION ORIENTATION (DEGRLES)
% POL(P/C) V * POLETZ/GRAPHIC)
DURHAM POLARISATION (°)
PLOT NUMBER 2
INSIDE 434
OUT LOW 0
TOTAL 433

proportional to the density on the electronograph, was found to be non-linear, and has subsequently been calibrated for all future digitisations. The machine has undergone modifications since the plates were first digitised however, and the present calibration curve is not necessarily applicable to the M82 plates. The present calibration curve, which is probably of the same form as the one which would have been applicable, has the correct characteristics to explain the discrepancy in the two sets of data. Most of the photo-electric measurements are made in the halo regions of the galaxy, where the density values range between 50 and 150 on the calibration scale On this part of the curve, the line is of steeper gradient than that expected for no calibration, and therefore the difference between two similar values of intensity $(i_1 - i_2)$ is amplified when the calibration is applied. The degree of polarisation, which is given by,

$$p = \frac{I_p}{I} \sim \frac{\sqrt{(i_1 - i_2)^2 + (i_3 - i_4)^2}}{i_1 + i_2} \qquad 6.4$$

is therefore increased upon application of the calibration.

The second possibility, is that the light suffers a small amount of depolarisation, as it traverses the optical components of the polarimeter. The magnitude of this depolarisation is likely to be small, because the most obvious depolarising component, the half wave plate, is achromatic over the waveband used

All the electronegraphs digitised after those of M82 have been calibrated A simple comparison, therefore like the one described here, for the Durham measurements of the Crab Nebula, with those of Woltjer

(1957), will show whether the calibration problem is the main contributing factor to the polarisation magnitude underestimate.

A quantitative study, between the photo-electric and present results, is made in section 6.4, to investigate the statistical errors associated with the Durham polarisation measurements.

6.3.3. Recent Photographic Measurements

A determination of the polarisation of M82 by a photographic technique has recently been published by Schmidt et al. (1976) and the resultant map is shown in figure 6.9.

The four initial plates of the galaxy, through a polarising filter, were taken on the Steward 80" reflector using an image intensifier with fibre-optic coupling to a photographic plate. The intensities on the plate, for each small area of the image, yield a set of values (i_1 - i_4, after calibration), which can be substituted in the equations of Chapter 1 to give a single estimate of the polarisation parameters for each location on the plate. The plates were aligned as accurately as possible, at the time of digitisation, and no further transformation was performed, to ensure an exact one to one correspondence between pixels. The spatial resolution of the map shown is 10 arc seconds squared, which is of the same order as the Durham map.

Although the main features of the two maps compare quite well, there are certain differences which are difficult to understand, when the respective techniques are compared. The photographic map, which has not been subjected to any form of smoothing, or quality control, seems to have a complete absence of erroneous vectors interspaced among the smooth

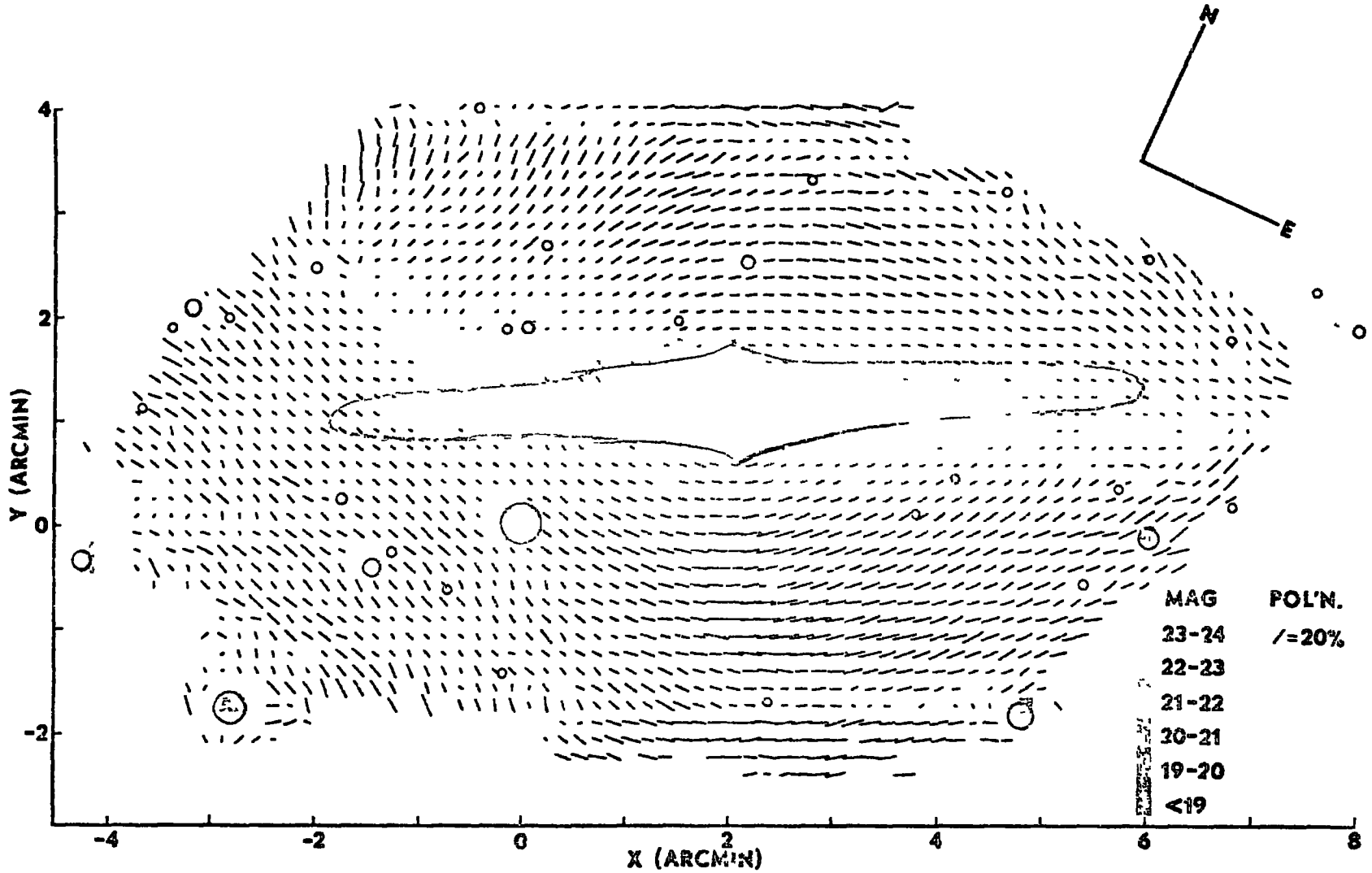

FIG. 6.9 THE PHOTOGRAPHIC POLARISATION MAP OF M82

pattern. This implies that there were no scratches, specks of dust, or cathode defects on any of the four plates used. The impeccable quality of the map, is doubly hard to believe, when it is recalled, that from a series of measurements (i_1 - i_4), it is not possible to make a determination of the exposure factors between the plates from the actual density of the images, or obtain two estimates of the polarisation parameters which can be compared to give a measure of accuracy of the mean value.

The photographic exposures were taken, so that the density in the halo regions of the galaxy, were on the linear part of the calibration curve This means that the measurements in the regions of high density, are near the saturation value for the emulsion, and are not to be trusted (Schmidt et al. 1976). It is in these regions, that the Durham map shows essentially zero polarisation, while that of Schmidt et al. indicates values of approximately 5%.

The measurements of Visvanathan and Sandage were used to calibrate the photographic plates, and the results obtained are not entirely independent of the previous photo-electric determination.

6 4 Analysis of the Errors Associated with the Durham Map

6.4.1. Comparison with Photo-Electric Measurements

The position of the best straight line through the plots shown in figures 6 7 and 6.8 shows any systematic difference between the two sets of data, and this was discussed in section 6 3.2. The scatter of the points about the best straight line, however, is a measure of the internal uncertainties associated with both sets of data. This can be

written in the form,

$$\delta^2 = \delta_E^2 + \delta_{PE}^2 \qquad 6.1$$

where δ is the r.m.s. difference between the photo-electric and electronographic measurements, and δ_E and δ_{PE}, are the intrinsic r.m.s. errors associated with the electronographic and photo-electric measurements respectively

The r.m.s. difference between the electronographic and photo-electric measurements, plotted in figures 6.7 and 6.8 is 2.7% in degree (after the systematic error has been extracted), and 6 8^o in position angle. If the uncertainties on the photo-electric measurements is assumed to be zero, these estimates give an upper limit or the statistical errors associated with the electronographic measurements.

Elvius gives no error estimates with her measurements, but if they are assumed to be of similar values to those obtained by Visvanathan and Sandage, estimates for δ_{PE} of 2% in polarisation degree and 4^o in position angle are reasonable. If these values are inserted into equation 6.1, estimates of the mean errors associated with the electronographic method, of 1.8% in degree, and 5.5 degrees in position angle are obtained.

6 4.2. Estimates of the Intrinsic Errors from the Data

The most obvious way to estimate the polarisation errors, is to start with the errors on the individual intensities (i_1 - i_8), and carry these errors through the set of reduction equations In practice, this is extremely difficult because of several factors.

Firstly, although for a first approximation, the photo-cathode

sensitivity at any point, could be assumed to have random fluctuations of a fixed amount, the instability of the PDS machine represents an additional fluctuation, which changes from electronograph to electronograph, and even with position on a particular electronograph. Secondly, rounding the intensities off to the nearest integer between 1 and 1,000, causes larger percentage errors on the faint areas, to those on the dense regions. Thirdly, the errors attributable to plate alignment, are more serious for a region of steep intensity gradient, than an area of smooth, flat, profile Finally, the errors introduced at the stage of sky subtraction, can only be treated thoroughly, if the photo-cathode sensitivity, and polarimeter vignetting functions, have been accurately determined.

A slightly more empirical approach, is to use the difference between the two independent estimates of the polarisation parameters, for each location on the plates, as a measure of the uncertainty associated with their mean value. These estimates can only be used, before the night sky has been subtracted, because only one set of values for the Stokes parameters (IS, QS, US) is determined from the set of four plates. The subtraction of the same sky parameters, from the two independent values for the total signal, implies that the two estimates of the galactic signal alone are non-independent.

If the two estimates, for the preferred direction, before sky subtraction, are θ_1 and θ_2, then the associated standard deviation of the mean value is given by

$$\alpha_\theta = 1/2 \cdot (\theta_1 - \theta_2) \qquad 6.2$$

The required error after sky subtraction, is then given to first order, by

$$\alpha'_\theta = \alpha_\theta \cdot (1 + I_S/I_G) = {}^1/_2 \cdot (1 + I_S/I_G) \cdot (\theta_1 - \theta_2) \qquad 6.3$$

where I_S and I_G are the respective values for the magnitude of the 'sky', and 'galaxy' signals respectively. Similar equations can be written to describe the uncertainties on the magnitude of the polarisation.

The estimate of α'_θ, for each location on the plates, from two estimates is not very reliable however, as it is not impossible to have values for θ_1 and θ_2, which agree extremely well, although they are both quite different from the true value. A solution to the problem, is to plot a frequency distribution of α'_θ for every location on the plate, and find the typical value for the uncertainty, averaged over all the points on the plate.

Figures 6 10 and 6.11 show frequency distributions of the two variables '$(1 + I_S/I_G) \cdot (\theta_1 - \theta_2)$', and '$(1 + I_S/I_G) \quad (p_1 - p_2)$', and the halfwidths give typical values for the variables of approximately 2% in magnitude and 10^o in position angle. Inserting these values into equation 6.3, results in estimates, for the typical errors associated with any vector on the polarisation map, equal to 1% in magnitude, and 5^o in position angle

Although the errors derived, are an important check, of the overall quality of the data, they do not give a completely full specification of the map produced, because they are a generalisation over the entire area covered by the map In practise, both polarisation degree and orientation for an area is dependent on both the surface brightness of the element concerned, and the degree of polarisation.

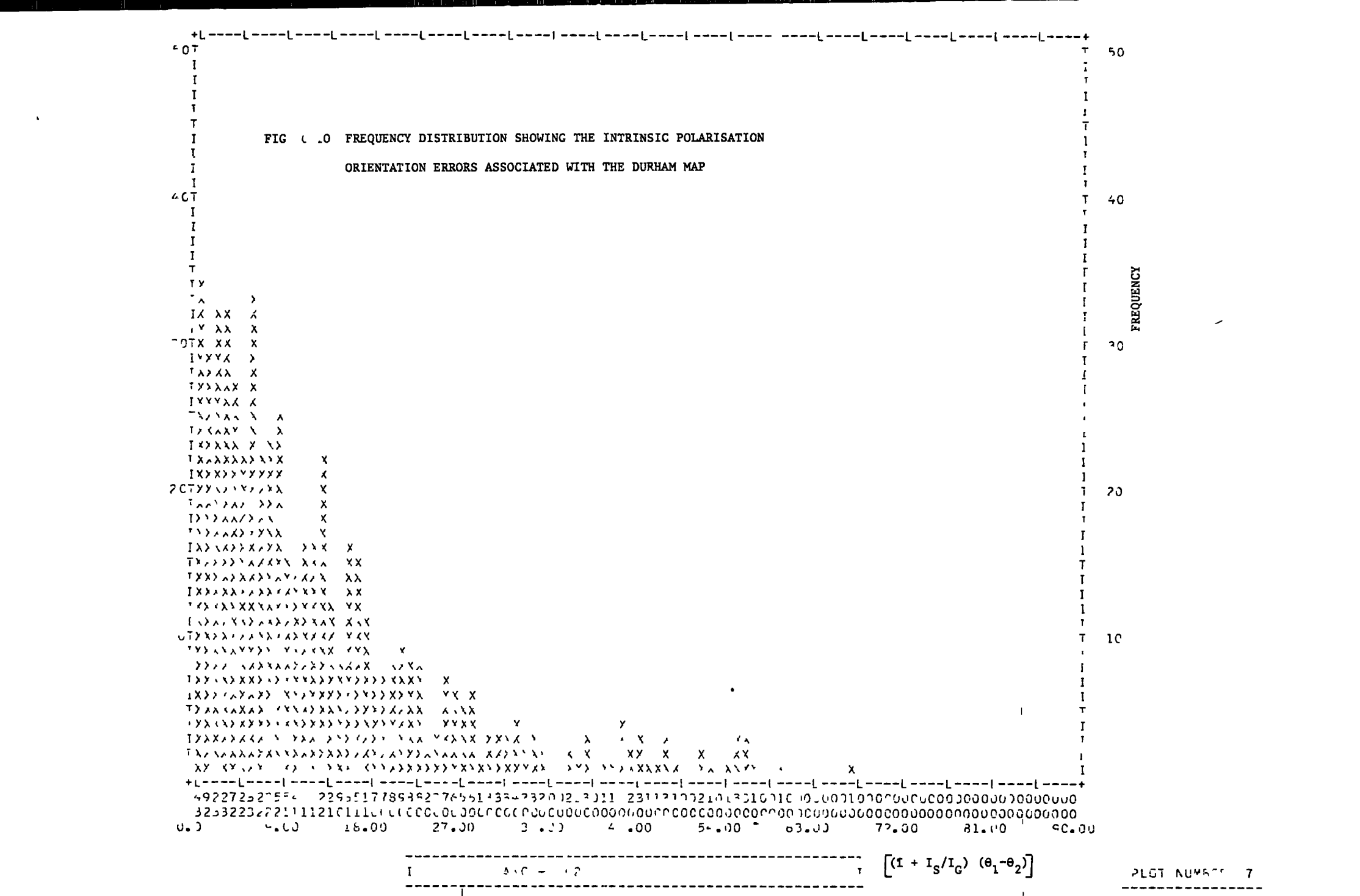

FIG 6.10 FREQUENCY DISTRIBUTION SHOWING THE INTRINSIC POLARISATION ORIENTATION ERRORS ASSOCIATED WITH THE DURHAM MAP

$\left[(1 + I_S/I_G)\ (\theta_1-\theta_2)\right]$

PLOT NUMBER 7

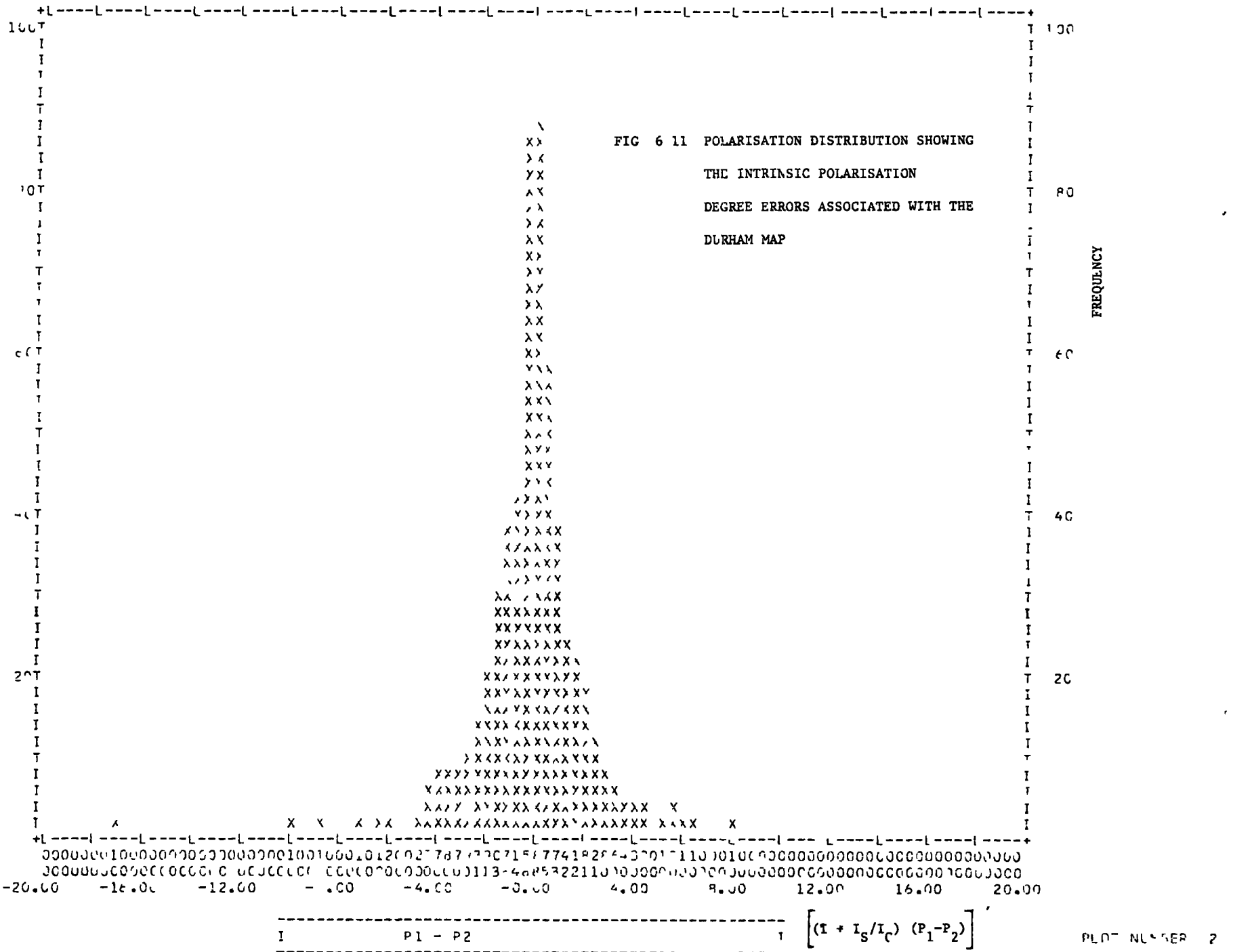

FIG 6 11 POLARISATION DISTRIBUTION SHOWING THE INTRINSIC POLARISATION DEGREE ERRORS ASSOCIATED WITH THE DURHAM MAP

These two relationships were investigated by plotting the quantities "α_p'" and "α_θ'" as a function of 'I_G' for different values of the polarisation degree 'p'. Figure 6.12 shows a particular plot, of the quantity '$(1 + I_S/I_G) \cdot (\theta_1 - \theta_2)$', against the Stokes parameter 'I_G', for all the points on the polarisation map which have polarisations between 8 and 12%. The scatter plot shows that the uncertainty in the measurement of direction, is a well defined function of the surface brightness of the element under consideration.

From a series of plots, similar to figure 6.12, a series of curves which describe the uncertainties associated with the polarisation measurements was built up. The resultant graphs shown in figures 6.13 and 6.14 describe the errors associated with the measurement of polarisation parameters, for any area of the plate, in terms of the particular physical conditions present at that location.

6.4.3. The Measurement of Standard Stars

As a final test, to determine if any systematic error was induced by the equipment itself, plates of several polarised stars were taken in exactly the same manner as the eight plates of the galaxy. The polarisation of the stars had previously been measured by several workers using photo-electric techniques.

For the star plates, the telescope was slightly defocussed, so that the point like objects, formed small circular images contained in one grid bar of the polarimeter image. The stars therefore took on the appearance of small extended objects and had purposefully been chosen so that they were of the same surface brightness as the real extended objects

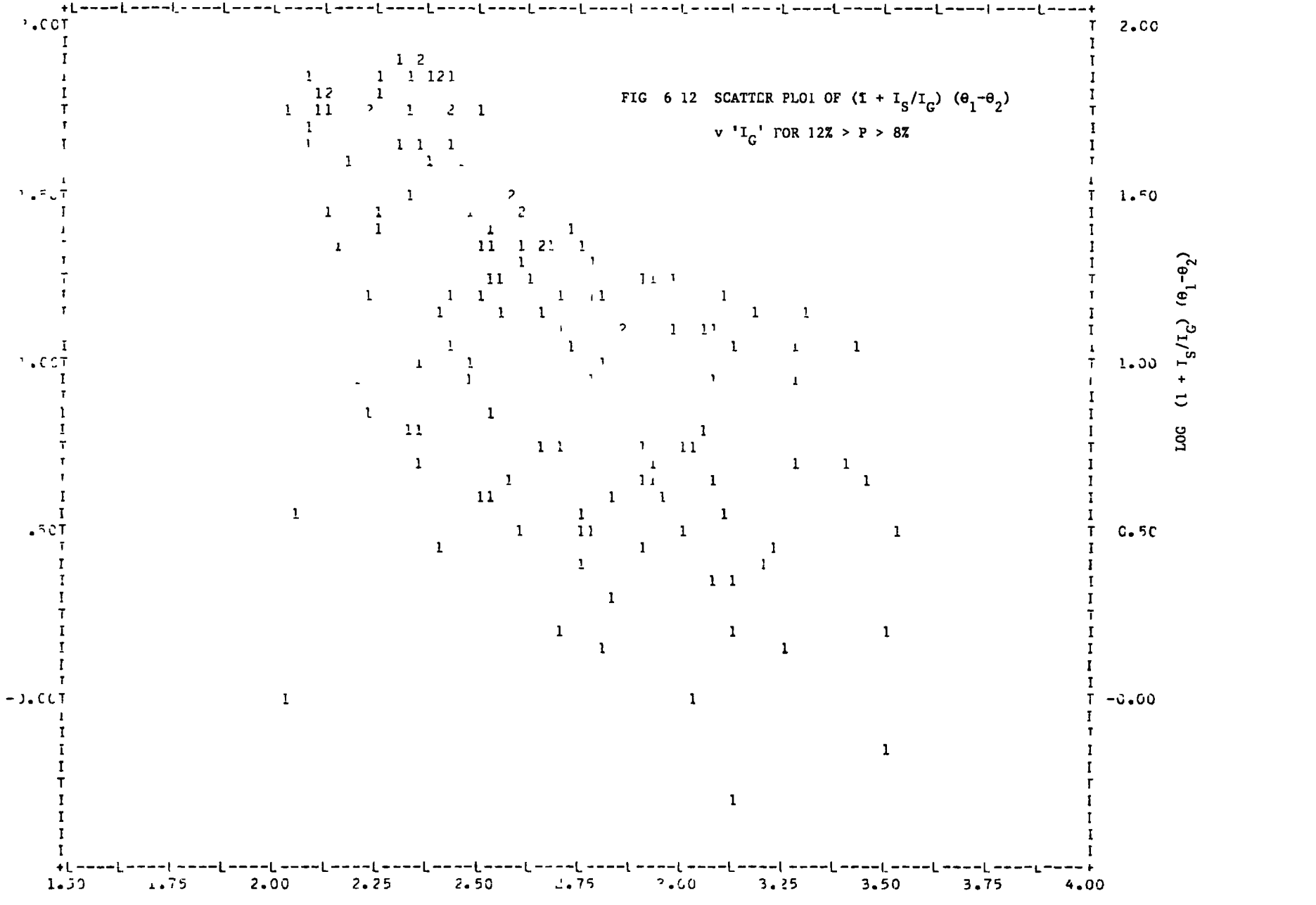

FIG 6 12 SCATTER PLOT OF $(1 + I_S/I_G)\ (\theta_1-\theta_2)$ v 'I_G' FOR 12% > P > 8%

I DISTRIBUTION OF ANG1-ANG2 FOR MB2 I

INSIDE 140 CUT LOW 9 CUT HIGH 5 TOTAL 154

PLOT NUMBER 3

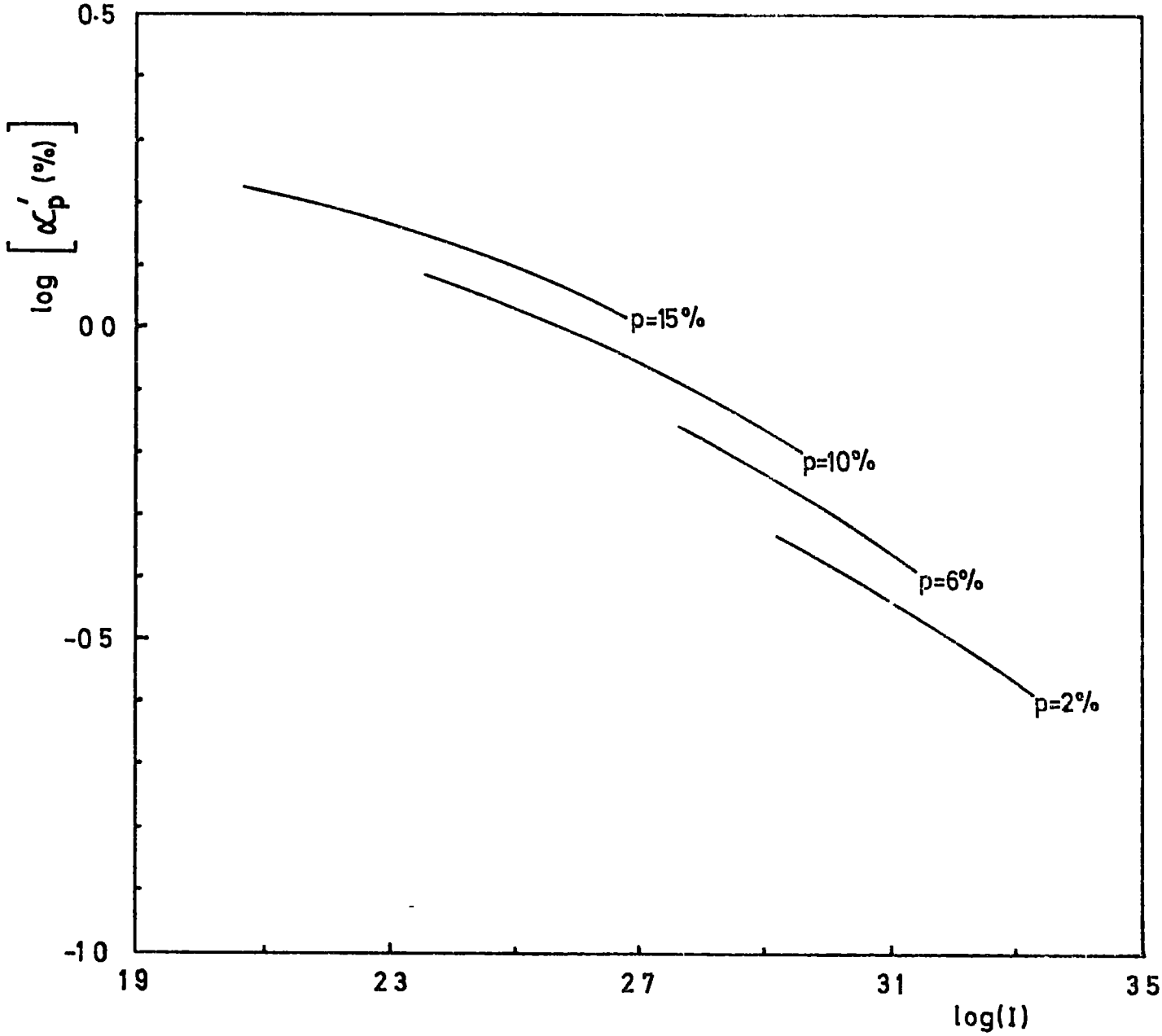

FIG 613 ERRORS IN POLARISATION DEGREE

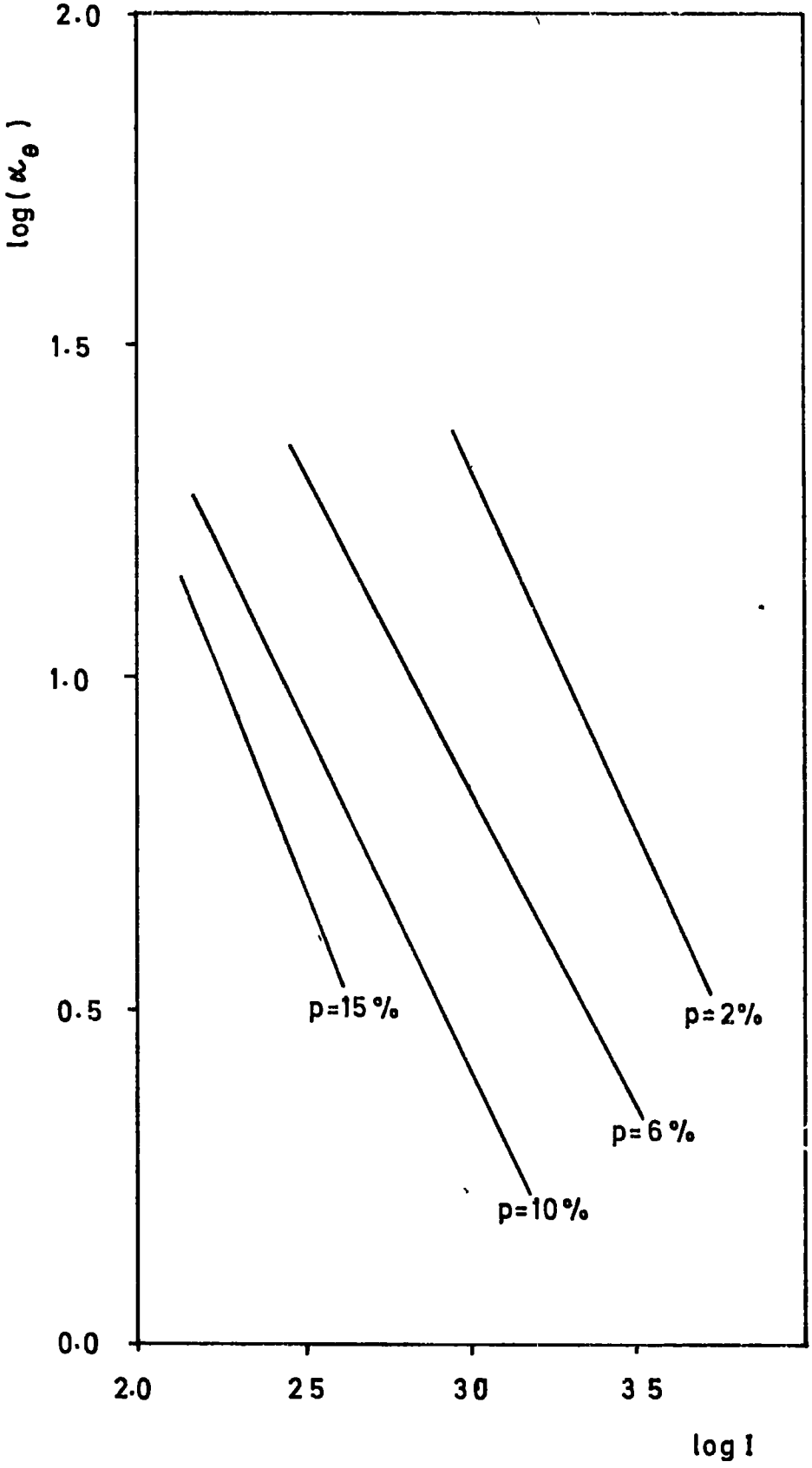

FIG 614 ERRORS IN POLARISATION ORIENTATION

to be observed. The reduction procedure was then carried out in a similar manner to that already described, except that, only one integrated area, centred on the star, and having dimensions slightly larger than the extent of the image, was used to calculate the polarisation parameters. The measurement therefore describes the polarisation of the integrated light from the star.

In some cases, the star was accidentally defocussed too much, and some of the incident light was lost behind a grid bar, in the focal plane of the telescope The results for the stars, are therefore expected to be less accurate than those obtained for a similar region in M82 Inspection of Table 6, which gives the present and previous determinations for the stars, indicates that there is no evidence for any systematic effect being present and confirm the validity of our technique for measuring nebular polarisation.

	Tabulated Value		This Work	
Star	P%	θ(Deg)	P%	θ(Deg)
HD 43384	2.7	170	2.3	172
HD 122945	0.1	56	0.3	69
HD 155528	4.6	93	4.3	90
HD 80083	0.13	140	1.4	128

Table 6. Comparison between our measurements and accepted values for standard polarised stars.

CHAPTER 7

THE GALAXY M82

7.1 Introduction

M82 is the primary member of irregular II galaxies, which are characterised by their lack of symmetry, and inability to be resolved into bright stars or star clusters. The appearance of M82 is that of a flattened irregular system seen nearly edge on, and if a distinct nucleus exists, it is highly obscured at optical wavelengths. The integrated spectral type of A5 (Humason, Mayall and Sandage, 1956), contrasts sharply with the colour index, B-V = +0 91 (de Vaucoulers 1959). This fact, together with the lack of resolution into stars, although the estimated distance, is only 3 Mpc (Tamann and Sandage, 1968), has led to suggestions that M82 is immersed in a dense cloud of dust.

The ratio of the major and minor axes, have been used in an attempt to estimate the angle of tilt of the disk to the line of sight ($\sim 8^{o}$), and, from the asymmetry of the dust lanes overlying the fact of the galaxy, the North-West side of M82 has been assumed to be nearest to the observer. (Lynds and Sandage, 1963). One of the more remarkable features of M82 is a possible system of luminous filaments (forming the halo of the galaxy), which extend several kiloparsecs from the galaxy. The existence of the filaments is now in doubt, and needs to be confirmed or otherwise by further studies.

Although it has been observed optically for a century, it was not

until the discovery that M82 was a powerful radio source (Lynds, 1961), that the stimulus arose for further detailed observations to be made.

7.2 The Synchrotron Hypothesis

Radio observations of Lynds (1961), showed that M82 was a radio source with spectral index of 0 2, very similar to that found for the Crab Nebula.

As a further investigation of the galaxy, several spectra in H_α light were taken with the slit of the spectrograph approximately parallel to the minor axis of the disk, crossing the image in the bright central region (Lynds and Sandage, 1963). The results, illustrated in figure 7.1, showed that the line emission from the halo becomes increasingly redder with increasing distance to the north of the galaxy and progressively bluer to the south. This was interpreted as a radial expansion of the emitting gas, (presumably forming the filaments of the halo), in a direction roughly perpendicular to the plane of the disk. The assumed small tilt of the disk ($\sim 8^{o}$) to the line of sight, meant that the axial outflow of gas along the minor axis, gave rise to the recession velocity component on the north-west side, and the approaching velocity component on the south-east side. The actual expansion velocity was therefore an order of magnitude greater than the measured component velocities. The expansion velocity, which increased linearly with distance along the minor axis, (from figure 7.1) was therefore estimated as 1,500 km/sec, at distances $\sim$ 2 kpc above and below the plane of the galaxy.

By analogy with the Crab, it was therefore suggested that the radio

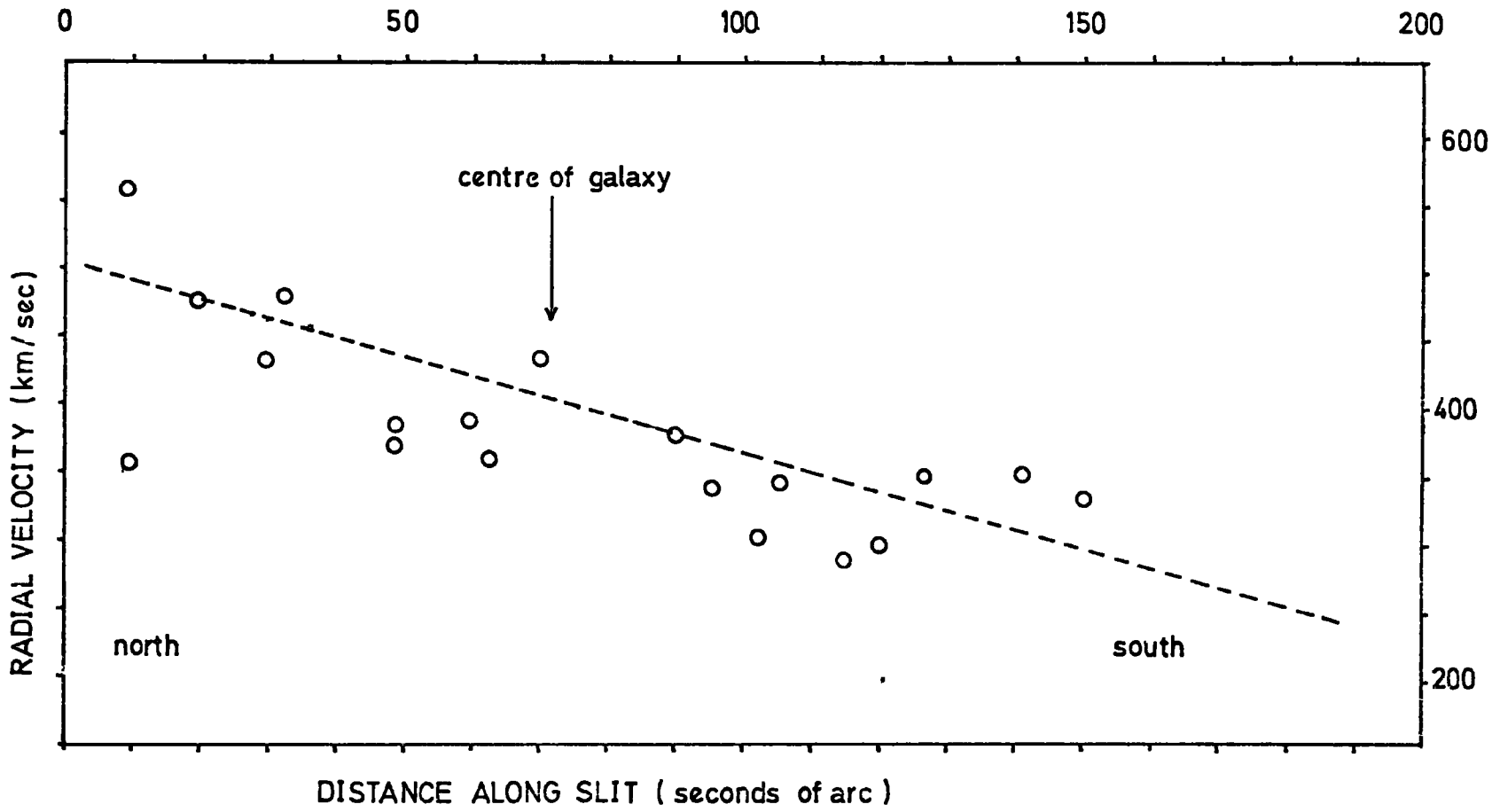

FIG 7 1 H_α RADIAL VELOCITY ALONG THE MINOR AXIS OF M82

emission from M82 was due to the synchrotron mechanism, and that extrapolation of the radio spectrum into the optical region, was responsible for the continuum optical radiation from the filaments. The expanding shell of gas, presumably caused by an explosive event in the nucleus of M82, at an epoch some 1.5×10^6 years ago, and excited by its own radiation field, seemed to form a perfect analogy with the Crab Nebula.

The successful detection of relatively large amounts of polarisation ($\sim$ 15%) in the halo regions of the galaxy (Elvius, 1963), appeared to confirm the synchrotron theory. The areas studied, near the minor axis of the galaxy were polarised, with the electric vector approximately parallel to the major axis of the galaxy, and therefore perpendicular to the radial appearance of the filaments. The vectors therefore, formed the expected pattern for synchrotron radiation, caused by electrons accelerated by a magnetic field in the direction of, and probably containing the filaments.

7.3 The Scattering Theory

The first difficulty with the synchrotron theory arose, when in 1965, Dent and Haddock, measured the radio spectrum of M82 to shorter wavelengths than had previously been investigated. The spectral index was found to decrease rapidly at shorter wavelengths, which meant that extrapolation of the radio spectrum, into the optical region, resulted in an optical synchrotron flux several orders of magnitude less than that measured by Lynds and Sandage (1963).

Further measurements of the optical continuum polarisation, at selected locations in the halo of the galaxy (Sandage and Visvanathan, 1969), showed that the direction of the electric vectors of the linearly

polarised component of the radiation in the halo, adhered much more closely to the normal to the radius vector from the centre of the galaxy, rather than being perpendicular to the filament from which the light was emanating. If a synchrotron model was accepted, this would mean, that the filamentary material, and the magnetic field were not dynamically bound.

The convincing evidence to eliminate the synchrotron hypothesis, came in 1972, when Visvanathan and Sandage found that the line emission from the halo, was also polarised. The H_α radiation measured, had exactly the same degree of polarisation as the continuum flux, and could therefore not be the product of recombination in the filaments.

As evidence against the synchrotron theory mounted, alternative models, in which light from the disk region of M82 was scattered into the line of sight by the halo medium, were proposed to account for the observed form of the polarisation pattern. (The scattering of light by small particles, introduced partial plane polarisation in the scattered ray, at right angles to the plane formed by the directions of the incident and scattered rays). The centro-symmetric polarisation pattern of M82, was therefore consistent with a model in which light from a very small area of the galaxy, near the central region of the disk (or perhaps the obscured nucleus?), was being scattered into the line of sight, by a cloud of scattering centres forming the halo of the galaxy.

The scattering theory, which required the strong, central, localised energy source, received further impetus when measurements in the radio and infra-red bands, revealed highly luminous compact sources,

near the expected position of the hypothesised nucleus. (Kleinmann and Low, 1969, Formalont, 1967). The localised power excesses at infra-red and radio frequencies, evoked comparison between the nucleus of M82 and Seyfert galaxies (Solinger, 1969), and two species of scattering hypothesis were contrived.

Elvius suggested that the polarisation was due to dust scattering in the halo of the galaxy. Solinger (1969), proposed a model for the galaxy, in which a nuclear explosion and accompanying hydrodynamic shock wave heated the expelled halo material, to sufficiently high temperatures to ionise the gas present. The (Seyfert) nuclear light was then Thompson scattered, from the electrons, while recombination radiation gave rise to the H_α emission

7.4 Difficulties with Scattering Models

The measurements of Visvanathan and Sandage (1972), which revealed that the H_α radiation from the halo, was polarised in exactly the same way as the continuum, thereby casting grave doubt on the synchrotron hypothesis, also posed severe problems for any form of scattering model. The polarisation in the line emission required that the H_α was scattered nuclear disk light, and did not originate in the filaments.

The velocity field obtained by Lynds and Sandage (1963), and confirmed by later studies (Burbidge et al., 1963, Heckathorn, 1972), which was initially explained convincingly by supposing that the radiating gas was expanding from the explosion centre required re-interpretation in terms of a scattering model. If the dust, or electrons, were expanding from the disk of M82, then the scattered H_α light would be red shifted

(with respect to the nucleus), to both the north and south of the galaxy. Conversely, an implosion would result in blue shifted light on both sides of the disk, while a static dust cloud would give rise to no Doppler shift whatsoever. None of these obvious possibilities, could give rise to the measured red and blue shifts to the north and south of the galaxy respectively.

Further results, from an important series of observations by Visvanathan and Sandage (1972), concluded that the H_α line in the halo had a width of only 6 Å, and, that the polarisation in the continuum radiation was independent of wavelength over the range 0.36 - 0.8 microns The narrow profile of the emission lines, indicated that Doppler broadening in the halo was small, and restricted the electron temperature to a value less than 10^4 °K. The blast wave origin, due to Solinger, which required temperatures of 10^7 °K was therefore excluded. Also, the lack of recombination radiation, inferred by the polarisation measurements, imposed a severe restraint on the density of low energy electrons in the halo.

The wavelength independence of the polarisation, which is consistent with expectation for Thompson scattering by electrons, is difficult to understand in terms of dust scattering. A size distribution of grains similar to that observed in our own galaxy, would give a marked increase of polarisation at longer wavelengths. However, V.Y. Canis Majoris is a notable exception (Shawl, 1969, Serkowski, 1969). The magnitude of the polarisation would be expected to reach values of $\lesssim$ 100%, if electron scattering was the responsible mechanism, whereas a suitable dust mixture, with a proportion of large particles (radius >

wavelength of radiation), when the scattered light is approximately unpolarised, could account for the observations.

Finally, Visvanathan and Sandage (1972) measured the spectral energy distribution in the halo and compared with that for the nuclear region which had previously been derived (Peimbert and Spinrad, 1970). The comparison tentatively showed that the filaments became increasingly bluer with increasing distance from the galaxy, which is in direct contrast to the reddening effect expected for light transmitted through a dust cloud.

Investigations by Mathis (1973), showed that a suitably chosen size distribution of different refractive index dust particles could reproduce the wavelength independence of the polarisation and the continuum colour gradient in the halo.

Elvius (1971) suggested that M82 was passing through an intergalactic dust cloud, with the south-west side of the disk, having a relative velocity towards the cloud, and the north-west side having a recession velocity of the same magnitude. The blue and red shifts of the line emission from the nucleus, to the south and north of the disk, was thereby partially explained, with the exception that the change of H_α wavelength would almost be a step function situated at the nucleus. The smooth gradient of the Doppler shift, with increasing distance along the minor axis of the galaxy (Lynds and Sandage, 1963) could only be reproduced if the dust cloud had a differential velocity with distance along the minor axis.

Although comparison of observation with expectation was not entirely satisfactory, the dust scattering model alone seemed the only

viable proposal that could at least partially meet the stringent restrictions imposed by the observations.

7.5 High Resolution Measurements at Radio and Infra-Red Wavelengths

Recent measurements in both of these spectral regions, have shown that no single, extra-luminous, compact source is present in the central region of the galaxy. The radio measurements, richly resolved over a wide range of frequencies, (Hargrave, 1974, Kronberg and Wilkinson, 1975), show that the nuclear region is complex in both spectra and geometry. The moderately resolved results of Kleinmann and Low (1970), show that the deep infra-red is also an extended source, while photographic results in the near infra-red (Raff, 1969), display many small localised intensity maxima. These have been identified by Van de Bergh (1971) as unusually luminous associations of early type stars. The ultra-violet spectral peaks, are obscured by the dust, but the clusters radiate sufficient power in the infra-red, where attenuation is much lower, to be resolvable on the infra-red plates The fact that the contrast between the emitting and surrounding regions increases with wavelength, implies that the intensity maxima are not simply holes in the obscuring dust. The analysis of line spectra from the emitting region, seem to confirm the presence of early type stars

These results have led to the conclusion that M82 is thermally powered, by an over luminous nuclear region, where copious quantities of dust have led to multiple star formation. The non-thermal radio sources resolved by recent radio measurements are not much more powerful than might be expected for multiple supernovae events, and the lack of any strong X-ray emission from the central region, has been taken as

further evidence, that no single explosive event of galactic magnitude has ever occurred in the nucleus if M82 (Solinger, 1976).

7.6 Inferences from the Polarisation Data

A novel approach was taken by Solinger and Markert (1975) to determine some of the physical parameters of the disk and obscured nucleus of M82, by investigating the shape of the polarisation pattern formed from the composite measurements of Elvius and Visvanathan and Sandage. The salient features of the method, were that the centre of symmetry of the pattern revealed the position of the hidden nucleus, while any deviation from the circular pattern to one having an elliptical form (elongated in the direction of the major axis of the disk) was a measure of the ratio of the nuclear and disk luminosities.

The model assumed a point source nucleus and a circularly symmetric disk of radially decreasing surface brightness, the latter given by,

$$I(r) = I_o \cdot e^{-kr} \qquad 7.1$$

where I_o is the surface brightness at the centre of the disk, I(r) the corresponding value at a distance 'r' from the centre, and k is a scale factor which can be altered to fit the data. It was further assumed that the nucleus and disk were situated in a cloud of Rayleigh scattering centres, forming the halo of the galaxy. The expected polarisation pattern could then be determined for a given position and orientation of the nucleus and disk, and for a given ratio of nuclear to disk luminosities. The parameters of the model could be varied until agreement between the model predictions and the experimental polarisation pattern was achieved.

The calculations concluded that the nucleus was situated near, but not coincident with the positions of the infra-red or radio intensity maxima, and, secondly, that the nuclear luminosity was probably only 5% of the total disk luminosity. The disk luminosity function was found to have a value for $^{1}/_{k}$, (the scale factor describing the intensity profile of the disk), of 1 kpc.

7.7 Present Interpretations of the Data for M82

7.7.1. Introduction

Adopting the evidence for the non-explosive evolution of M82, Solinger et al. (1976), have attempted to explain all the observational properties of the galaxy with a simple model, in which M82 was a normal spiral galaxy which drifted into the M81 group of galaxies, less than 10^{9} years ago. The interaction between M82, and an extensive, tenuous, cloud of dust and gas surrounding the M81 region, (inferred from the already radio detected H.I. cloud surrounding the M81 group), accounts for the evolution and observed properties of the galaxy.

7.7.2 The Interactive Process

The slow accretion of the dilute dust and gas in the central dense regions of the spiral galaxy (M82), led to the rapid formation of massive stars, which may be continuing to the present day. The super giants, which are responsible for the over luminous nucleus, soon complete their evolutions, by going through the supernova stage, and in doing so, they expel the copious quantities of dust observed in the disk, and near halo regions of the galaxy A simple model of the thermally powered drifting galaxy, which can satisfactorily explain the optical appearance of M82, has also been shown by Solinger

to account for many of the observed characteristics.

7.7.3. The Velocity Field

The Doppler line shifts to the north and south of the galaxy, are explained in a similar way to that proposed by Elvius (1972), for the point source nucleus The main difference, is that the unlikely velocity gradient of the dust (described in section 7.4) is not necessary, because the smooth gradient of theDoppler shift is a natural consequence of the light source being an extended region, and not a point source of radiation. The complex velocity field near the plane of the disk, is due to the interaction of the dynamically bound intrinsic dust, with the large scale dust field of the intergalactic region.

7.7.4. Polarisation and Isophotal Measurements in the Halo

The new interpretation of the origin and motion of the dust cloud surrounding the galaxy, does not significantly affect the conclusions previously formed from the polarisation pattern, which assumed that the dust was a result of a nuclear explosion, and therefore originated in the centre of M82. It does however, impose more stringent requirements on the change in intensity of the scattered light, as a function of radial distance from the source of illumination. Earlier comparison of the expected intensity gradient, for a spherical dust cloud bound to M82, and the observed intensity profile, had shown that the dust density decreased as the square of the distance from the source, and was therefore bound to the galaxy. If however, the galaxy is drifting in an external intergalactic dust cloud, the density should be uniform, and the intensity gradient of the scattered light with distance from

the source, should be concordant with this view point.

Solinger (1976), has calculated the expected profile, using the disk and nuclear parameters, obtained from the earlier polarisation studies (Solinger, 1975), and obtained good agreement with the observations, except for small distances away from the galactic plane. The results of the calculations are illustrated in figure 7.2 (taken from Solinger, 1976), where the expected intensity profile for a disk source, and nucleus with 5% of the total galactic luminosity, is compared with the observations. The results show that for distances 100 arc seconds (ν 2 kpc) from the source, it is necessary to have a decreasing dust density to describe the rapid fall in intensity profile. The solid line, showing the difference between the theory and observations is approximately straight, which implies that the necessary steepening of the intensity gradient is exponential, and therefore requires a similar form of decreasing dust density to explain it.

Solinger therefore argues, that the fit is consistent with required constant dust density at large distances from the galaxy, and the exponential increase as the disk is approached is caused by the expelled dust intrinsic to M82.

7.7.5. The Colour Gradient

The slight blueing of the scattered continuum, with increasing distance into the halo, is explained as a natural consequence of the source distribution of light in the disk of the galaxy. The dominant source contribution to the scattered light at distances close to the central region of M82 comes from the non-nuclear areas, while at large

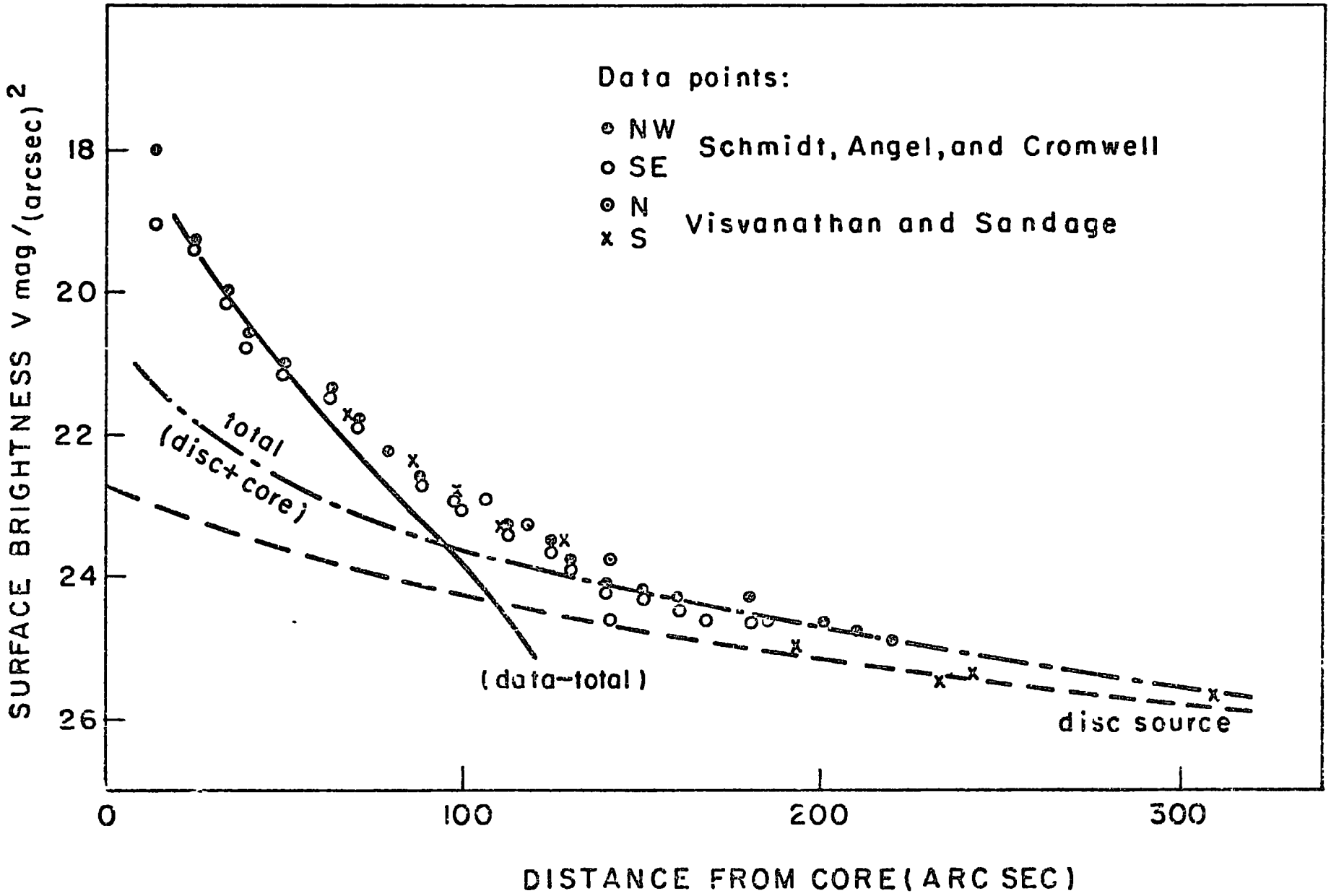

FIG. 7.2 THE SURFACE BRIGHTNESS ALONG THE MINOR AXIS OF M82.

distances from the plane of the galaxy, the quality of the incident light on the scatterer, is described by the spectrum of the integrated disk light. A gradual blueing of the disk radiation, with increasing distance from the nuclear region, is all that is required to account for the observed colour gradient in the halo.

7.7.6. The 'Filaments'

The filamentary appearance of the halo has been synthesised (Solinger, 1976), by allowing the large scale constant dust density, to exhibit clumping, with a scale size of approximately 10 arc seconds. The results were consistent with the appearance of the M82 halo, where the filaments are not long winding wisps as in the Crab Nebula, but are a more randomly composed series of bright 'knots' and dark 'spiders'.

7.8 Analysis of the Durham Map for M82

7.8.1. Introduction

The map obtained, contains information about the state of polarisation of the light at each point in M82. The Stokes vector 'I', describes the total amount of light coming from each of the integration areas, and is therefore a measure of the photometric brightness in the B waveband.

The primary reason for observing M82, was to test the reliability of the electronographic camera, and subsequent computer reduction programs, as a new technique for the production of high resolution polarimetric maps. Although the halo polarisation has been previously studied however, the present map, with several hundred points in the galaxy analysed simultaneously, represents a much more complete

determination of the polarisation pattern. The techniques employed by Solinger (1975, 1976), to investigate the obscured central regions of the galaxy, (using the small number of photo-electric polarisation points), can therefore be applied to the present data, to determine the validity of the conclusions arrived at from this earlier work.

7.8.2. Preliminary Analysis of the Durham Data

As a preliminary step, the centre of symmetry of the pattern has been found in order to try and locate the position of the hidden nucleus.

In order to locate the position of the centre, an initial estimate was made of its position, and, from this position a radius vector was drawn out to each of the points at which the polarisation had been measured. The projection of each of the polarisation vectors along the radius vector was then taken, and the individual projections summed. Each projection was weighted with the polarised intensity ($\sqrt{Q^2 + U^2}$), observed at that point. The centre of symmetry of the pattern, is the point at which the sum of the projections is a minimum, and this was found by slowly varying the position of the centre until the minimum was found.

The program was run on the two independent halves of the map obtained from electronographs 1 - 4 and 5 - 8 respectively, which gives a good check of the consistancy of the results. The mean position of the hidden nucleus from this determination is compared with that obtained by Solinger and Markert (1975) in figure 7.3. The centre of symmetry found by the above method can be compared with that of

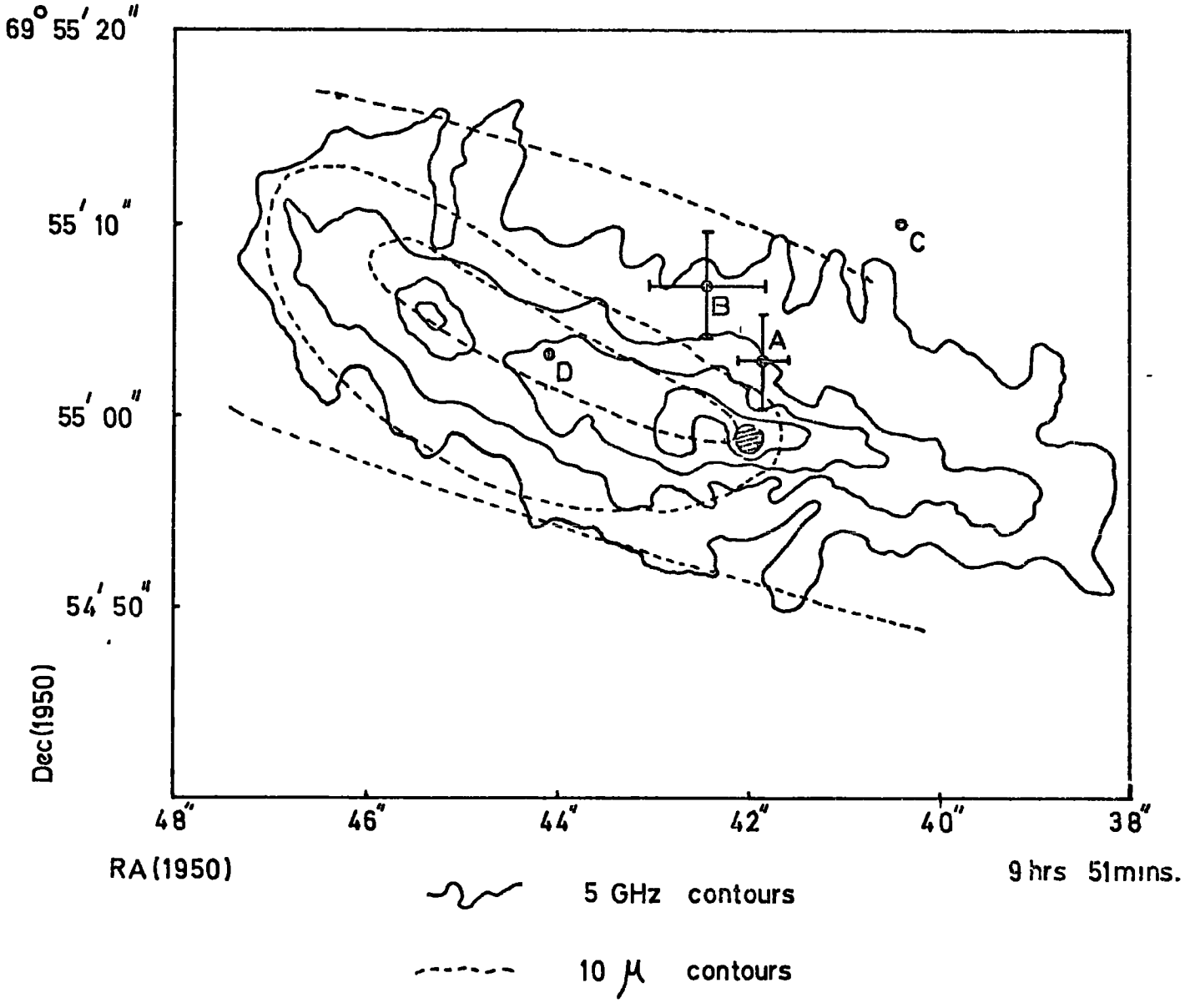

5 GHz contours

10 μ contours

CENTRAL LOCATIONS

A	centre from polarisation pattern	(present work)
B	—————//—————	(Sollinger 1975)
C	radiant of the filamentary structure	(Heckathorn 1972)
D	the optical bright spot	

FIG 73 CENTRAL LOCATIONS IN M82

Solinger and Markert even though the latter used both a disk and nucleus as a source of luminosity, because the disk is symmetric about the nucleus. The error bars are derived from the dispersion of the two estimates about the mean. Other interesting physical features of the central region of M82 are also included in figure 7.3 for comparison.

7.8.3. The Solinger and Markert Model

Very recently the program of Solinger and Markert (private communication) has been made available to us at Durham. The features of the program are described in section 7.6. The program has been run on the Durham data using only the most reliable measurements (~ 400 c.f. the 50 used by Solinger and Markert). Table 7 shows a comparison of the best fit parameters of Solinger and Markert and the ones describing our present data. It is comforting to note that the program gives very similar fits to both sets of data, and also that our naive attempt to locate the centre of symmetry is also in total agreement.

It is obviously possible using our data to extend the Solinger and Markert model to include non-symmetrical disk luminosity functions, finite disk thickness, and geometric details of the scattering medium, to yield further details of the unseen regions of M82

7.9 M82 Conclusions

Many previous considerations of M82 have emphasised that various central features in M82 were almost coincident, but it is not obvious that there is a detailed correspondence between them, as would be

Model Parameter		Photo-Electric Measurements	Durham Measurements
Position of Nucleus	R A.	9^{hrs} 51' 42.3"	9^{hrs} 51' 41.9"
	Dec.	69^{o} 55' 6"	69^{o} 55' 3"
Position Angle of Disk		70^{o}	73^{o}
Ratio of Nuclear to Disk Luminosity		0.05	0.06
Disk Luminance Scale Factor (k)		1 kpc	0.5 kpc

TABLE 7. Physical Parameters of M82 using the Modelling Program of Solinger et al. on the Photo-electric and present observations.

expected if a true compact nucleus were present. The most intense radio component (cross hatched in figure 7.3), has no special position in the infra-red source, which itself is only near to the centre of symmetry. Other centres (shown for completeness in figure 7.3), for example the optical bright spot are rather meaningless because of the large amount of obscuration at optical wavelengths. The position of the 'radiant of the filaments' is also in some doubt if the most recent interpretation is accepted. The absence of a compact nucleus is also emphasised by the recent high resolution measurements at infra-red and radio frequencies. The available data at different wavelengths seems to indicate that there is a central, extended active core in M82 of $\sim$ 300 pc in diameter.

The lack of an identified singular nucleus does not however preclude the possibility that M82 has some resemblance to the nuclear regions of Seyfert galaxies, the over-luminance of which has been attributed to supernovae events at a rate of perhaps 1 every 10 years in a limited volume (McCrea, 1975). In the case of M82, the active region of the galaxy may be $\sim$ 300 pc in diameter, about ten times the size of a Seyfert nucleus, and the process would therefore be modified. For a galaxy such as M82, with large amounts of dust in the central region, this process does seem particularly appropriate. A galaxy of this type, if we had a face on view, could represent the connecting link between Seyferts and normal galaxies.

GENERAL CONCLUSIONS

The work in this thesis describes one of the first attempts to accurately map the linear polarisation of nebulous objects. Using the improvements in recording technique offered by the advances in electronography, and with automated reduction techniques, it is now possible to rapidly produce accurate polarisation measurements at a few thousand points simultaneously in a faint nebulous object.

The results obtained with our technique for M82 are a considerable improvement both in quality and quantity on those previously available. With these results, not only has it been possible to confirm the previous conclusions made by Solinger, but it is feasible to extend our knowledge on the luminosity distributions and conditions within M82

Already the technique has been applied to the Orion Nebula (Pallister et al., 1976), and the Sombrero galaxy (Scarrott et al., 1976), and very exciting results are emerging.

REFERENCES

Axon, D.J., Ph.D. thesis, University of Durham, 1976.

Dent, W.A. and Haddock, F.T., Quasi-Stellar Sources and Gravitational Collapse, (Univ. of Chicago Press), p. 381, (1965).

de Vaucouleurs, G., Lowell Obs. Bull., 4, p. 105, (1959).

Elvius, A., Lowell Obs. Bull., 5, p. 281, (1963).

Elvius, A., Lowell Obs. Bull., 7, p. 117, (1969).

Elvius, A., Astron. and Ap., 19, p. 193, (1972).

Formalont, E B., Observations of the Owens Valley Radio Observatory, Vol 7, (1967)

Hargrave, P J., M.N.R.A.S., 168, p. 491, (1974).

Heckathorn, H M., Ap. J., 173, p. 501, (1972)

Humason, M.L., Mayall, N.U. and Sandage, A.R., Ap. J., 61, p. 97, (1956).

Jenkins, A F. and White, E.H., Fundamentals of Optics, (1957).

Kleinmann, D.E. and Low, F., Ap. J. (Letters), 159, p. L165, (1970).

Kronbergh, P and Wilkinson, M., preprint, (1975).

Lynds, C.R. and Sandage, A., Ap. J., 137, p. 1005, (1963).

Lynds, C.R , Ap. J., 134, p. 659, (1961).

Mathis, J.S., Ap. J., 183, p. 39, (1973).

McCrea, W H , Tercentary Symposium of the Royal Greenwich Observatory, (1975), in the press

McMullan, D., Powell, J.R. and Curtis, N.A., Adv. Elec. Phys., 33A, p. 37, (1972)

Öhman, Y., M N R.A S., 99, p. 624, (1939).

Peimbert, M. and Spinrad, H., Ap J , 160, p. 429, (1970).

Rafi, M., Ap. J. (Letters), 157, p L29, (1969).

Sandage, A and Visvanathan, N., Ap. J., 157, p. 1065, (1969).

Schmidt, G.D , Angel, J.R.P. and Cromwell, R.H., 1976 (in the press).

Shawl, S.J., Ap. J., 157, p. L57-L58, (1969).

Serkowski, K., Gehrels, T. and Wisniewski, W., Astron. J., 75, p. 85, (1969).

Shurcliff, W.A and Ballard, S S , Polarised Light, (Van Nostrand Co.), (1964).

Solinger, A.B., Ap. J., 72, p. 830, (1967).

Solinger, A.B., Ap. J., 155, p. 403, (1969).

Solinger, A.B., Ap. J. (Letters), 158, p. L21, (1969).

Solinger, A.B. and Markert, T., Ap. J., 197, p. 309, (1975).

Solinger, A.B , Morrison, P. and Markert, T., Ap. J. (preprint), (1976).

Tammann, A and Sandage, A.R., Ap. J., 151, p. 825, (1968).

Van de Bergh, S., Astron. and Ap., 12, p. 474, (1971).

Visvanathan, N and Sandage, A , Ap. J., 76, p. 57, (1972).

Woltjer, L., Bull. Astron. Inst. Neth., 13, p. 301, (1957).

ACKNOWLEDGEMENTS

The author wishes to thank Dr. S.M. Scarrott for his guidance, assistance, and helpful suggestions given at all stages of this work. It is a pleasure to thank the other members of the research group for help in taking the data. The facilities and expertise at the Royal Greenwich Observatory provided by Dr. R.G. Bingham, Dr. D. McMullan and Dr. J. Pilkington are also gratefully acknowledged, along with the staff of the Wise Observatory, Israel.

Professor A.W. Wolfendale is thanked for making the facilities of the Department readily available, and the author is also grateful to the Science Research Council for the studentship and funding his expeditions to Israel. Mrs. V A. Gold is also thanked for the expeditious typing of this thesis.

Finally, the author wishes to thank his parents for their encouragement, and his wife for her kind understanding of his nocturnal absences.